UNIVERSITY OF BIRMINGHAM

Temperature dependent plastic deformation of magnesium using micro-pillar compression

by

Ubaid-ur-Rehman Ghori

A thesis submitted to University of Birmingham for the degree of

DOCTOR OF PHILOSOPHY

School of Metallurgy and Materials
College of Engineering and Physical Sciences
University of Birmingham
May 2020

UNIVERSITY OF BIRMINGHAM

Note: Please sign this form and present it to the Bindery with your thesis, so that it can be bound at the front of the Library deposit copy

RESEARCH THESIS

Author's Declaration

Full name (block capitals, surname first): GHORI, UBAID-UR-REHMAN

Full title of thesis/dissertation (block capitals): TEMPERATURE DEPENDENT PLASTIC DEFORMATION OF MAGNESIUM USING MICRO-PILLAR COMPRESSION

College/School/Department (block capitals): SCHOOL OF METALLURGY AND MATERIALS

Date of award of degree (leave blank):

1. I understand that one printed and one electronic copy of my thesis/dissertation (the Work) will be deposited in the University Library (the Library) and in a suitable electronic repository, for permanent retention.
2. Without changing the content, the Library or any third party with whom it has an agreement to do so, may convert either copy into a format or medium for the purpose of long-term retention, accessibility and preservation.
3. The Library will publish, and/or arrange with appropriate third parties for the non-exclusive publication of, a bibliographic description of the thesis/dissertation, and the author's abstract.
4. Unless arrangements are made to the contrary, (see paragraph 6. below), the Library is authorised to make the Work available for consultation in the Library, and via a recognised inter library loans system. The Library is authorised to make the electronic copy of the Work freely accessible to individuals and institutions - including automated agents - via the Internet.
5. Rights granted to the University of Birmingham through this agreement are entirely non-exclusive. I retain all my rights in the Work in its present version or future derivative works.
6. I understand that I may apply to the University to retain the right to withhold access to the content of my thesis/dissertation. Access to the paper version may be withheld for a period which shall not normally exceed four calendar years from the congregation at which the degree is conferred. The actual length of the period will be specified in the application, together with the precise reasons for making that application. The electronic copy may be withheld from dissemination via the web or other networks for any period.
7. I have obtained permission for any use made of substantial amounts of published or unpublished copyright material (text, illustrations, etc) where the rights are owned by a third party, other than as permitted under either The Copyright Designs and Patents Act 1988 (as modified by any related or successor legislation) or the Terms and Conditions of any Licence governing its use.
8. The content of the copies I shall deposit with the Library will be the final version of my thesis, as approved by the Examiners.
9. I understand that the Library and administrators of any electronic theses repository do not hold any obligation to take legal action on behalf of myself, or other rights holders, in the event of a breach of intellectual property rights, or any other right, in the material deposited.
10. I understand that, in the event of my thesis/dissertation being not approved by the Examiners, this declaration will become null and void.

Signature: *(Ubaid-ur-Rehman Ghori)* **Date: 05.05.2020**

For Library use (please leave blank):

Classmark: **Accession number:** **Control number:**

eTheses Repository url:

Preface

The research work described in this thesis was carried out by the author in School of Metallurgy and Materials, University of Birmingham (from July 2015 to May 2020) under the supervision of Dr. Yu-Lung Chiu and Prof. Ian P. Jones.

The presented work is original, and no part of the work has been submitted for a degree at this or any other university/institute. Wherever the work of others has been drawn upon, it is acknowledged and cited in the text.

Dedicated to my parents specially my father, who is not in this world, but his loving memories always remain a part of me,

and

my family, specially my wife,

and

my sisters

Acknowledgement

I would like to express my deepest gratitude to my PhD supervisors Dr. Yu-Lung Chiu and Prof. Ian P. Jones for their kind support and valuable guidance during my PhD study. I appreciate their sincere help and emotional support for me and my family.

I appreciate the contribution and efforts of Dr. Chris Cooper and Mr. Jag Sangha in manufacturing and installation of a novel cryo-stage set-up on the Tescan SEM.

Many thanks to my existing and old EM group fellows specially Dr Bo Pang for his valuable time and kind support in my crystallography and TEM learning.

I would also like to pay thanks to Dr Hammad, Dr Yasir, Dr Zafar, Mr. Awais and Dr Zeeshan for their encouragement and giving me the confidence to finish my PhD.

At the end, I gratefully acknowledge the funding received from University of Engineering & Technology Lahore, Pakistan, for the completion of my PhD.

Abstract

This study investigates the temperature dependence of the deformation processes of basal <a> slip, pyramidal <c+a> slip and $\{10\bar{1}2\}$ tension twinning in magnesium single crystals. In situ SEM compression between 23°C and -94°C was performed on FIB-milled square shaped micro-pillars taken from selected grains of a polycrystalline sample of pure magnesium. For low temperature micro-pillar compression testing, a novel cryo-stage was designed and employed in combination with the existing pico-indentation system. Post-mortem SEM and TEM were then used to analyse the microstructures of the deformed micro-pillars.

$[11\bar{2}1]$ oriented micro-pillars were compressed at 23°C, -28°C and -94°C to activate basal <a> slip. These pillars deformed by a similar deformation mechanism, irrespective of the test temperature. The Critical Resolved Shear Stress (CRSS) for basal <a> slip increased with decreasing test temperature, which is the CRSS increased by approximately 9 MPa on reducing the temperature from 23°C to -94°C. This trend is explained by the increase in Peierls lattice friction for the glide of <a> dislocations on the basal plane accompanied by a rise in activation free energy for the nucleation of <a> dislocations on the basal plane.

For the activation of tension twinning, micro-pillars with a $[1\bar{3}20]$ loading direction were compressed over a similar temperature range. The micro-pillars deformed mainly by the activation of $\{10\bar{1}2\}$ tension twins followed by basal <a> slip within the twinned region. The CRSSs for the twin activation / nucleation and for the twin growth showed no change with temperature. The temperature insensitivity of the twin activation / nucleation is explained by the dominant role of stress-concentrators in twin nucleation during micro-pillars compression

whereas temperature insensitivity of the twin growth is explained by the availability of the dislocation sources and mobile dislocation segments required for twin growth.

For the activation of pyramidal <c+a> slip, [0001] oriented micro-pillars were compressed over the same temperature range. The activation of pyramidal <c+a> slip was confirmed at all the test temperatures. The CRSS for pyramidal <c+a> slip decreased with a reduction in temperature i.e. a drop in testing temperature from room temperature to -90°C resulted in an approximately 39 MPa lower CRSS for pyramidal <c+a> slip. This anomalous temperature dependence of pyramidal <c+a> slip is explained by the balance between the thermally activated processes of dissociation of <c+a> dislocations and cross-slip of <c+a> dislocations between different pyramidal planes.

Overall, the findings of this study provide a useful dataset for understanding the orientation dependent temperature sensitivity of the dominant deformation modes in magnesium at micron length scale under uniaxial compression at room temperature and to a range of cryogenic temperatures.

Table of Contents

1 Introduction

Lightweight structural materials remain an important area for scientists and engineers due to ever-increasing demand from the modern automobile and aircraft industries [1], [2]. Due to their high specific strength, magnesium and magnesium alloys have gained much attention amongst commercially available structural materials. They are considered to be a potential replacement of many aluminium and steel based commercial alloys for the transport industry. However, the application of magnesium and its alloys to a wider range of such applications is limited by their less developed state in comparison with many FCC and BCC commercial alloy systems like aluminium and steels alloys. Not much is known about the fundamental deformation mechanisms of these alloys under different service conditions. Thus, there needs to be a more in-depth understanding of the mechanical behaviour of magnesium metal at first and then magnesium-based alloys under different service conditions of temperatures and loading modes, to find the best working conditions for this metal to offer the optimum mechanical and structural properties.

The crystal structure of magnesium is hexagonal closed packed (HCP) with an axial ratio of 1.624 [3]. High specific strength, excellent damping capacity and biocompatibility make it a preferred choice over steel, aluminium, and titanium for many structural applications. However, the application of magnesium to industrial and commercial applications is not straightforward because of its intrinsic plastic anisotropy and the lack of simultaneous activation of multiple slip and twinning modes which otherwise is essential for homogenous shear during any forming

process. The reason is a very big difference in critical resolved shear stress (CRSS) values of the different slip and twinning systems of magnesium.

Recent developments in the field of small scale (micro and nano) in-situ mechanical testing have enabled researchers to relate the measured mechanical response of a material to the underlying deformation mechanisms remarkably as the entire deformation volume can be analysed which is not possible in any traditional mechanical testing [4], [5]. In-situ micro-compression, micro-tension, micro-bending, nano-indentation, and advanced characterization techniques, like dual-beam focused ion beam and high-resolution transmission electron microscopy allow researchers to better understand the underlying plastic deformation behaviour of many materials of scientific and commercial importance under various testing conditions [6].

Loading direction with respect to crystal orientation and CRSS value are the key factors that determine the activation of a particular slip or twinning mode during the plastic deformation of any material. Various factors can affect the CRSS value of a deformation mode. In the past, there have been many studies to help understand the effect of loading direction on the activation of different slip and twinning modes in single crystal magnesium. However, a thorough investigation is the need of the hour, as limited literature is available on the effect of temperature on the activation of slip and twinning. Micro-pillar compression testing is a very convenient way to do this.

The present work is related to the orientation-dependent mechanical behaviour of magnesium single crystals at room temperature and below. This thesis consists of seven chapters, including this chapter. Chapter 2 contains a literature review relevant to the current research work. Chapter 3 describes the experimental procedures used during this research work including designing and installation of a novel cryogenic stage (for low-temperature testing).

Subsequently, Chapters 4, 5 and 6 contain all the results obtained with a discussion section at the end of each of these chapters. Lastly, the conclusions based on the most important findings of this research are presented in Chapter 7.

2 Literature Review

2.1 Crystallography of Magnesium

Magnesium has an HCP (closed packed hexagonal Structure) crystal structure. In 1967, Partridge [3] described the crystallography of the HCP unit cell in detail. The axial lengths of a primitive hexagonal unit cell are $a_1 = a_2 \neq c$ and the crystallographic axial angles are $\alpha = \beta = 90^{\circ}$ and $\gamma = 120^{\circ}$ as shown in Figure 2.1 (a). The three primitive hexagonal unit cells are combined to form a hexagonal lattice in the way shown in Figure 2.1 (b). The atoms in this hexagonal lattice are stacked in three layers following a sequence of ABABA (Figure 2.1(c)). A perfectly packed HCP unit cell has a packing factor of 0.74 and a coordination number of 12. The c/a axial ratio for an ideal hexagonal unit cell is 1.633. In case of magnesium, the c/a ratio is 1.624 with lattice parameters of a = 0.32 nm and c = 0.52 nm.

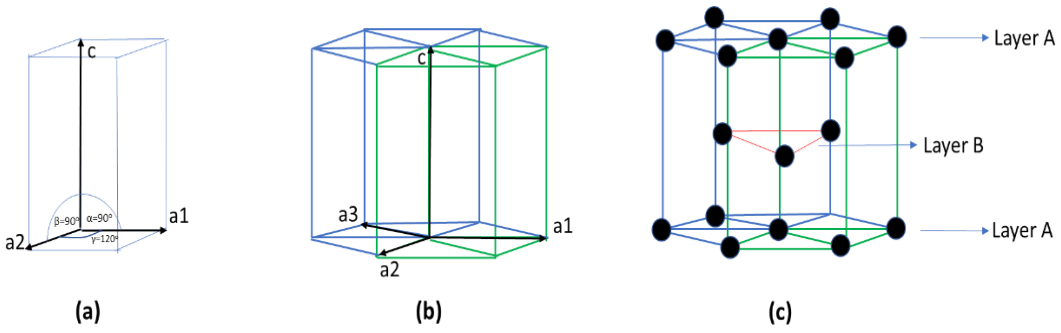

Figure 2.1: (a) Primitive hexagonal unit cell, (b) three primitive unit cells combined to form an HCP lattice, and (c) atomic packing sequence in the HCP lattice

The HCP crystal structure is usually indexed by using four-axis Miller-Bravais indices based on four vectors, namely $\mathbf{a_1}$, $\mathbf{a_2}$, $\mathbf{a_3}$ and **c** where $\mathbf{a_3 = -(a_1 + a_2)}$. Any direction in this four-indexing system is described as $\mathbf{d = u\,a_1 + v\,a_2 + t\,a_3 + w\,c}$ where $\mathbf{u + v = -t}$. The close packed directions in the HCP unit cell lie in the basal plane and have indices of $< 2\bar{1}\bar{1}0 >$ [7]. Important planes and directions of the HCP unit cell are shown in Figure 2.2.

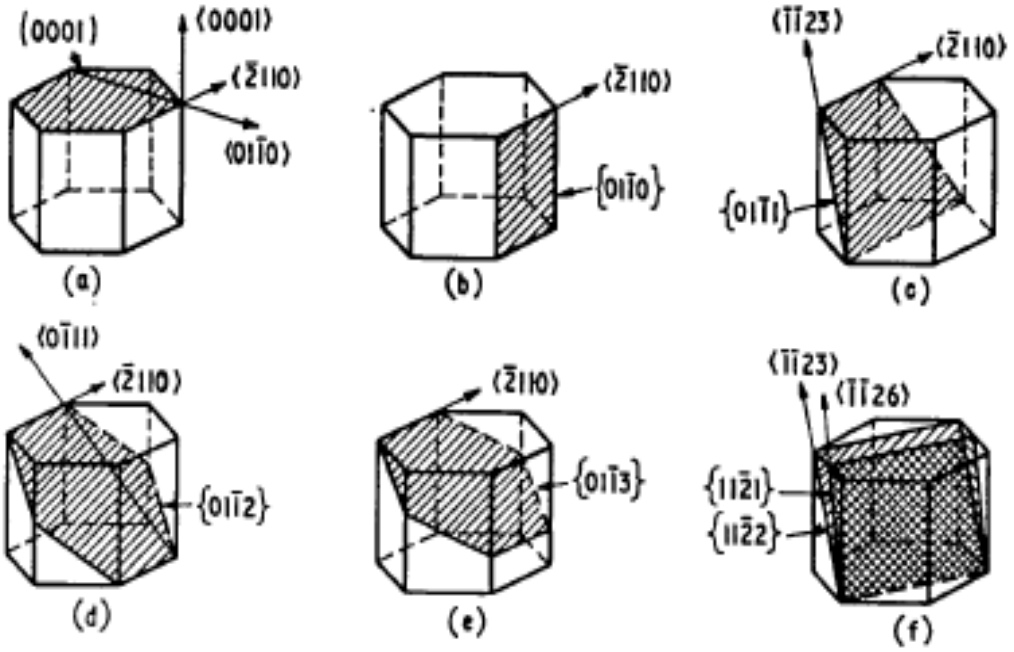

Figure 2.2: Important planes and directions in HCP unit cell [3]

In this crystal system, the planes are directly indexed by taking the reciprocals of their respective axial intercepts. These reciprocal intercepts were then reduced to the smallest integers with the same ratio, to give the indices of a plane. Different from the cubic system, in HCP unit cell a direction parallel to plane (h k i l) normal is determined by using the following relation:

$$[u\ v\ t\ w] = [h\ k\ i\ \frac{3}{2}\left(\frac{c}{a}\right)^2 l\ ] \qquad [7]$$

2.2 Dislocations in HCP Unit Cell

The dislocations in HCP metals have been described by using a bi-pyramidal model (Figure 2.3), with three atoms on the basal plane and two mirror atoms at $\frac{2}{3}, \frac{1}{3}, \frac{1}{2}$ on both sides of the basal plane [3], [8]. This model describes two types of perfect dislocations: one, along the sides of the triangular base (AB, BC and CA) and other, perpendicular to the basal plane (ST or TS). Besides these perfect dislocations, there are also partial dislocations, Aδ, Bδ and Cδ along the basal plane whereas δS, and δT perpendicular to the basal plane. More details about the important dislocations in HCP metals are given in Table 2.1.

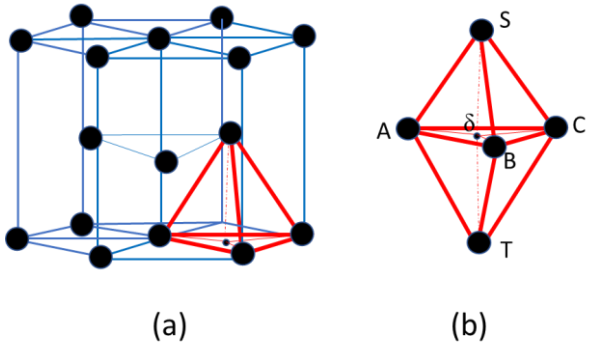

Figure 2.3: (a) HCP structure and (b) a bi-pyramidal model showing Burgers vectors of different dislocations

Table 2.1: Burgers vectors of important dislocations in HCP metals [3]

Type	Miller Bravais Indices	Magnitude in terms of lattice parameters	Total Number of dislocations including negatives
AB (perfect)	$\frac{1}{3}$<11$\bar{2}$0>	a	6
TS (perfect)	[0001]	c	2
ST+AB (perfect)	$\frac{1}{3}$<11$\bar{2}$3>	$\sqrt{c^2 + a^2}$	12
Aδ (partial)	$\frac{1}{3}$<1$\bar{1}$00>	$\frac{a}{\sqrt{3}}$	6
δS (partial)	$\frac{1}{2}$[0001]	$\frac{c}{2}$	4
AS (partial)	$\frac{1}{6}$<2$\bar{2}$03>	$\sqrt{(\frac{a^2}{3} + \frac{c^2}{4})}$	12

2.3 Plastic Deformation in Magnesium

Four possible slip systems and two twinning systems are involved in plastic deformation of magnesium. These include basal <a>, prismatic <a>, pyramidal <a> and pyramidal <c+a> slip systems. The tension twinning and compression twinning are the two twinning modes. A schematic illustration of slip and twinning modes in magnesium is shown in Figure 2.4. Dislocations with <a> type Burgers vectors can produce slip in the basal (0001) plane, the

prismatic $\{10\bar{1}0\}$ plane and the pyramidal $\{10\bar{1}1\}$ plane whereas dislocations with <c+a> Burgers vectors can slip on pyramidal $\{10\bar{1}1\}$ and pyramidal $\{11\bar{2}2\}$ planes [3], [9].

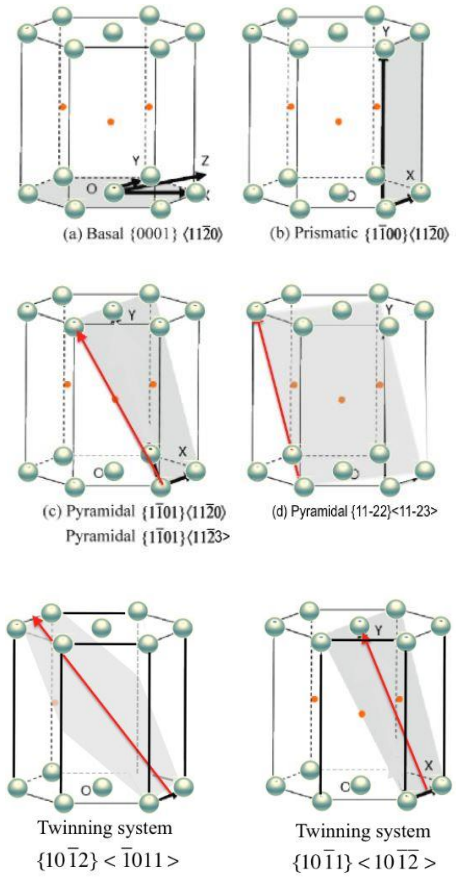

Figure 2.4: Schematic illustration of basal <a>, prismatic <a>, pyramidal <a>, pyramidal <c+a> slip systems, {$10\bar{1}2$} tension twinning and {$10\bar{1}1$} compression twinning [10]

According to Von Mises's criteria, a homogeneous change in the shape of a polycrystalline material requires the activation of five independent slip systems. Interestingly, in the case of magnesium, deformation occurs mainly by basal <a> slip which thereby offers only two independent slip systems [9]. Even adding prismatic <a> or pyramidal <a> slip systems does not satisfy the Von Mises criterion individually as each of them provides only two independent

slip systems [3]. Thus, activation of non-basal slip along the <c+a> direction on pyramidal planes or twinning is essential to fulfil this criterion because it can provide five independent slip systems. Furthermore, basal <a>, prismatic <a>, and pyramidal <a> slip can accommodate plastic strain only along a-axis, so pyramidal <c+a> slip is vital to accommodate strain along c-axis because any arbitrary shape change in an HCP metal requires deformation along both "a" and "c" directions.

2.3.1 Deformation by Slip

Metallic materials undergo plastic deformation either by slip or twinning. The role of slip is more pronounced as compared to twinning when considering plastic deformation. Slip involves sliding of one part of a crystal over another part of the crystal by an integral multiple of its interatomic distance. The process of slip is favoured by the presence of dislocations. In order the slip to occur, a minimum amount of shear force is required acting on a slip plane, the most densely packed crystallographic plane, and in the slip direction, the direction on the slip plane with the highest linear atomic density, to overcome the resistance to dislocations motion which is known as the critical resolved shear stress (CRSS). The resolved shear stress along slip plane and in the slip direction is related to the tensile stress (σ), acting along the loading axis of a single crystal specimen having cross sectional area (A), by a factor known as the Schmid factor (m) as given by the following relation and illustrated in Figure 2.5:

$$\boldsymbol{\tau = m \,.\, \sigma = \frac{F}{A}\,(\cos\lambda\ \cos\varphi)}$$

where A=is the cross-sectional area of the sample, F = applied load, λ= angle between slip direction and loading direction and φ= angle between slip plane normal and slip direction

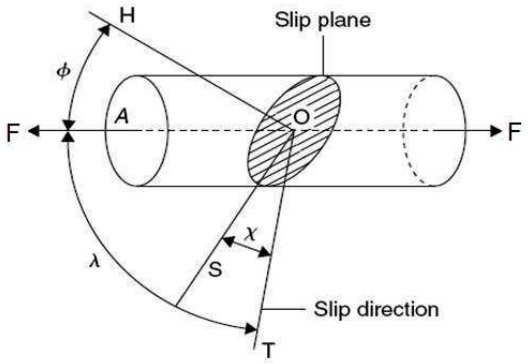

Figure 2.5: Tensile test specimen orientation and resolved shear stress [11]

The Schmid factor (*m*) is an important component of the plastic deformation of metals introduced by Schmid et al. [12]. Schmid's law correlates the applied load to the shear stress acting on a slip plane. During a tensile test of a crystalline material, each slip plane is differently oriented with respect to the loading axis and the shear stress acting on every slip plane is directly dependent on the *m* value, which varies amongst the various slip and twinning systems for a fixed loading direction. As a result, the deformation mode with the highest Schmid factor is activated preferably compared to other counterparts. This condition is generally true but not always, the reason being the difference in CRSS values for different slip and twinning modes i.e., as soon as the effective shear stress exceeds the CRSS value of a slip/twinning mode, that deformation mode becomes active even though the Schmid factor may not be the highest for that deformation mode. That is why measuring the CRSS value for each of the slip systems and twinning variants is very important.

2.3.1.1 Basal <a> slip

Basal <a> slip involves the movement of $\frac{1}{3} < 2\bar{1}\bar{1}0 >$ type dislocations on the (0001) basal plane. This motion of dislocations occurs only when the resolved shear stress along this plane reaches the CRSS value. Basal <a> slip is the most commonly observed slip system during

plastic deformation of magnesium at room temperature and has been studied by several authors [10], [13]–[28]. This dominance of basal<a> slip is attributed to its very low CRSS values [20], [23], [24], [28]. The most favourable orientation for the activation of basal <a> slip is achieved when the loading direction lies at 45 degrees to the c-axis which gives the highest Schmid factor of 0.5 [29]. However, basal <a> slip is always found to be the main deformation mode even when the loading direction is away from 45 degrees [13], [22], [24], [25]. Burke et al. [20] performed uniaxial tension tests on magnesium single crystals by varying the angle between the loading axis and the c-axis from 6 degrees to 72 degrees and reported activity of basal <a> slip always as the main deformation mode.

In the past, basal <a> slip was studied by several authors in magnesium single crystals for different reasons, but mainly to investigate the work hardening behaviour and its relative ease of activation as compared to other deformation modes. Work hardening behaviour during basal slip has been studied by characterizing a change in the slope of stress-strain curves obtained during uniaxial testing and with the help of the underlying dislocation substructure. Whereas its ease of activation has been investigated by measuring its CRSS value and considering the effects of sample size, mode of loading and initial dislocation density on its CRSS value. In this regard, experimental techniques like macro-compression, macro-tension, in-situ SEM pillar compression, in situ TEM pillar compression and in-situ TEM tension tests have been used on magnesium single crystals with a loading direction at 45 degrees to the basal plane normal and a sample size of 100 nm to a few millimetres [13]–[17], [19], [24], [25], [28].

It is generally agreed that the work hardening behaviour of magnesium during tensile deformation of a single crystal for the activation of basal <a> slip can be divided into two stages based on the stress-strain curves: stage A and stage B as shown in Figure 2.6 [13], [20], [24],

[26]. Stage A is an easy glide stage characterized by a low work hardening rate and stage B is characterised by a rapid work hardening rate. On the stress-strain curve, stage A is considered to extend from the start of yielding to a point of rapid change in the slope of the curve whereas stage B is considered to extend from point of termination of stage A up to failure. The mechanism of dislocation interactions is different in both the stages which is explained briefly in the following paragraphs based on the description of Hirsch et al. [13] in the light of their TEM observations.

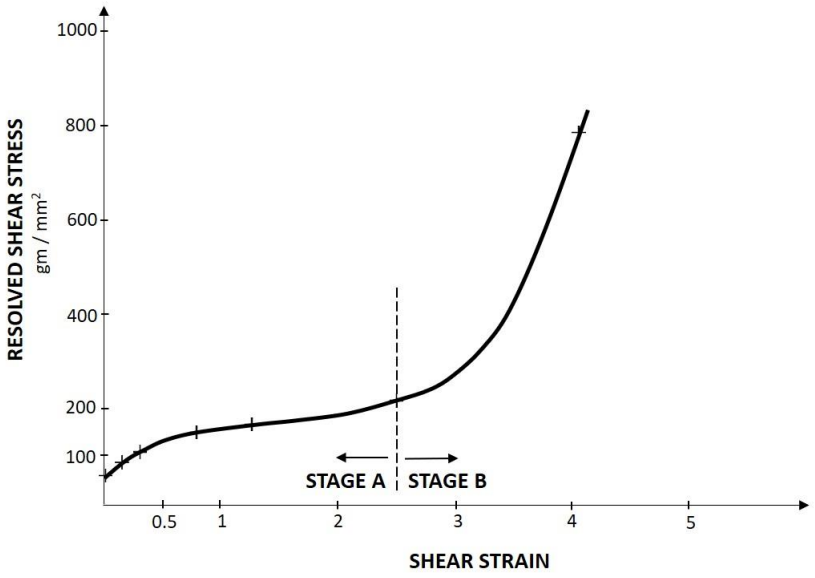

Figure 2.6: Resolved shear stress vs shear strain of magnesium single crystal deforming via basal slip showing two stages of work hardening (stage A and stage B) [13]

In stage A, pre-existing dislocation sources work independently and emit dislocations that entrap one another, resulting in dipole bands comprising of both screw dislocations but of edge dislocations as well [13]. At the same time, screw dislocations annihilate through cross-slip leaving behind the edge dislocations and the excess of the screw dislocations of the same sign. As a result, work hardening rate in stage A remains low as most of the dislocations annihilate

or make dipoles which have relatively smaller interaction radii with the mobile dislocations resulting into their limited contribution towards the work hardening. Thus, the flow stress during this stage is predominantly controlled by the internal stress field from residual screw dislocations, clusters of edge dislocations and dislocations of non-primary slip systems [13], [28].

During stage B, the formation of strong dislocation tangles and dislocation networks contribute towards the rapid rate of work hardening. Two other types of non-primary basal dislocations, which were inactive during stage A of plastic deformation, also became activated alongside the primary basal dislocations and resulted in the formation of hexagonal networks. This kind of hexagonal structure was reported by Hirsch et al. [13] and is shown in Figure 2.7. Additionally, during the last phase of stage-B, the presence of non-basal dislocations and deformation twins have been reported by Bhattacharya [28] and Hirsch et al. [14]. These also contribute towards the rapid increase in the rate of work hardening.

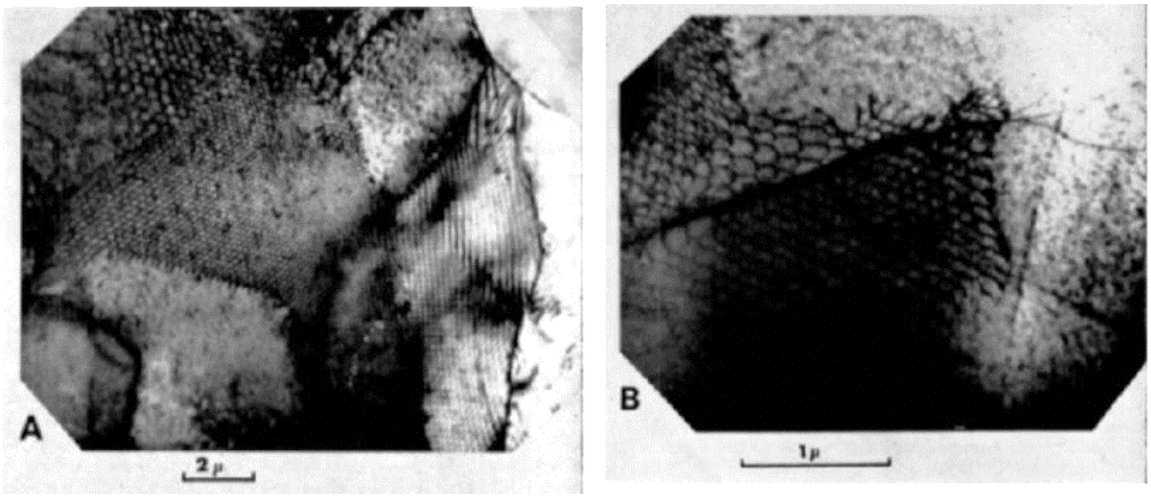

Figure 2.7: TEM image of a section cut along the basal plane from a 45 degree compression specimen of pure magnesium deformed to Stage B of work hardening showing hexagonal networks of dislocations [13]

As mentioned before, an important perspective whereby to study basal <a> slip in magnesium is to investigate the relative ease of its activation by measuring the CRSS values for this most common deformation mode [15]–[20], [23], [24], [26]. In this regard, different techniques have been employed to measure CRSS values for basal <a> slip. However, there exists a wide variation in reported CRSS values for this slip system. At room temperature, Burke et al. [20], Conrad et al. [24], Sharp et al. [24], and Bhattacharya et al. [26] reported CRSS values for basal <a> slip in the range of 0.39 — 1 MPa, whereas most recent studies on basal <a> slip have reported CRSS values for basal <a> slip as high as 268 MPa [18]. These huge variations in CRSS are related to many factors, including sample size, mode of test, testing conditions and the method used to compute CRSS value from raw mechanical test data. Amongst these mentioned factors, the most important is the size of the sample used for the measurement of CRSS. In past literature, a CRSS value of 0.39 — 1.0 MPA is reported for millimetre-sized specimens, 10 — 15 MPa for micrometre-sized specimens and ~268 MPa for submicron-sized specimens. This trend of increase in CRSS value with the decrease in sample size follows the common phenomenon of "smaller the stronger" which is also known as the "size-effect" [30], [31]. However, this size-effect is also related to the initial dislocation density in such a way that a higher initial dislocation density tends to minimize the size-effect or, in other words, no size-effect could be observed in case of a higher initial dislocation density [18].

Another important investigation of the activity of basal <a> slip was carried out by Qian Yu [10]. She carried out in-situ TEM tensile testing with a gauge length (width of the tensile specimen) of 900 nm to 80 nm with emphasis on the size-effect. For her specimens favourably oriented for basal slip, she observed the activation of primary basal <a> slip system for a gauge length of 800nm — 150nm and activation of non-basal slip systems alongside the primary basal slip system in the range of 150nm — 80nm. In her experiments, pre-existing basal dislocations

acted as dislocations sources in all specimen sizes. With a decrease in specimen size, the number of dislocation sources also decreased and transformed the general plastic behaviour from 3d plasticity to 2d plasticity. In specimens from 900 nm — 400 nm, due to a greater number of dislocation sources, dislocations interactions and their multiplication were more significant, which ultimately resulted in more elongation and lower yield stress. In the second regime of sample size from 400 nm to 150 nm, the mean free path of the dislocations was compatible with the specimen dimension. As a result, the deformation took place by the glide of single primary basal dislocations on one set of slip plane. The dislocations then escaped from the free surface resulting in shear failure along that glide plane which was referred to a 2d plasticity. In the third regime of sample size, less than 150 nm, the higher value of yield stress was found to be related to the activation of non-basal dislocations alongside basal dislocations.

2.3.1.2 Prismatic <a> slip

Magnesium deforms by prismatic <a> slip when dislocations of Burger vectors $\frac{1}{3} < 2\bar{1}\bar{1}0 >$ glide on one of the prismatic $\{10\bar{1}0\}$ planes. However, prismatic <a> slip is not often observed during room temperature plastic deformation of magnesium even when the loading direction, with respect to crystal orientation, is favourable for its activation, based on the highest Schmid factor criterion [29]. The reason for the rare activation of prismatic <a> slip is its higher CRSS value as compared to other slip and twinning modes [28], [32], [33].

Reedhill and Robertson [32] reported the activation of prismatic <a> slip at room temperature and below, determined by analysing slip traces on the faces of the deformed specimens during uniaxial tensile testing of magnesium single crystals along the basal plane. However, at a higher temperature, the dominant deformation mode was observed to be pyramidal <a> slip [32]. Contrary to this study, there were several studies of tensile testing along the basal plane of

single crystal magnesium in which the main deformation mode was reported to be pyramidal <c+a> slip instead of prismatic <a> or pyramidal <a> slip [28], [34]–[37]. So, there exists a difference in the past literature concerning the plastic behaviour of magnesium when strained along the basal plane.

The compression behaviour of magnesium single crystals is different from their tensile behaviour when strained along the basal plane [15], [16], [32], [37]. There are several recent reports on room temperature in-situ SEM/TEM compression experiments on <$2\bar{1}\bar{1}0$> oriented magnesium single crystal micro-pillars of varying sizes ranging from 20 μm to 0.5 μm [16], [17], [38]–[40]. For this crystal orientation, based on the maximum Schmid factor criterion, easy glide by basal <a> slip has the minimum chance of activation with zero Schmid factor and prismatic <a> slip has the maximum chance of activation with the highest Schmid factor of 0.433, whereas Schmid factors for pyramidal <a>, pyramidal <c+a> and $\{10\bar{1}2\}$ tensile twinning are 0.41, 0.33 and 0.25 respectively [39]. But in all these experiments performed by compression along the basal plane, $\{10\bar{1}2\}$ tensile twinning and basal <a> slip within the twinned region are reported to be the main deformation modes identified by strain bursts in stress-strain curves and confirmed by post-mortem SEM/TEM microstructures in the deformed micro-pillars [15], [16], [38]–[40]. However, there are two recent in-situ micro-pillar compression studies which identified two key parameters; those can lead to a transition in deformation mode from $\{10\bar{1}2\}$ tensile twinning to prismatic <a> slip during compression along the basal plane [39], [40]. Sim et al. [40] performed in-situ SEM compression on 5 μm micro-pillars at 25°C, 75°C, 100°C, 150°C and 225°C along a <$2\bar{1}\bar{1}0$> loading direction. Their stress-strain curves showed a change in deformation behaviour below and above 150°C, from typical twinning associated strain bursts below 150°C to typical slip associated continuous plastic flow above 150°C as shown in Figure 2.8 [39]. Their post-mortem TEM results

confirmed that prismatic <a> slip was responsible for continuous plastic flow above 150°C whereas $\{10\bar{1}2\}$ tensile twinning and basal slip within the twinned region were responsible below 150°C [39] as illustrated in Figure 2.9 and 2.10. The reason is that the CRSS value for prismatic <a> slip decreases with an increase in temperature whereas CRSS for twinning is not affected by temperature. Hence a temperature is reached where deformation mode changed from twinning dominated plasticity to dislocation dominated plasticity where the activated slip system was confirmed to be prismatic <a> slip (Figure 2.8).

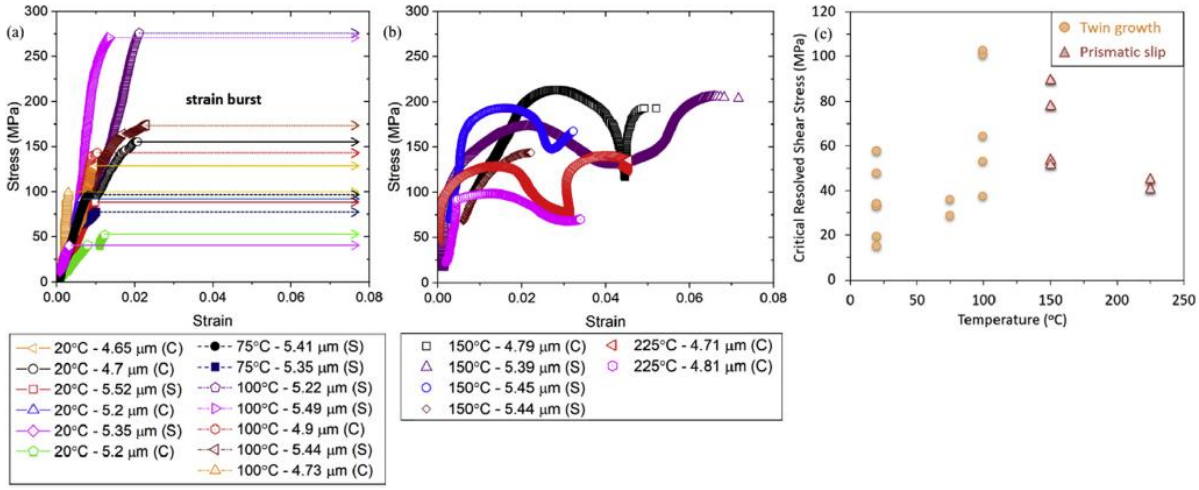

Figure 2.8: Stress-strain compression curves of 5µm microcrystals at different temperatures, (a) 25°C, 75°C,100°C and (b) 150°C and 225°C with circular(C) and square (S) shaped pillars. (c) variation in CRSS with test temperature [39]

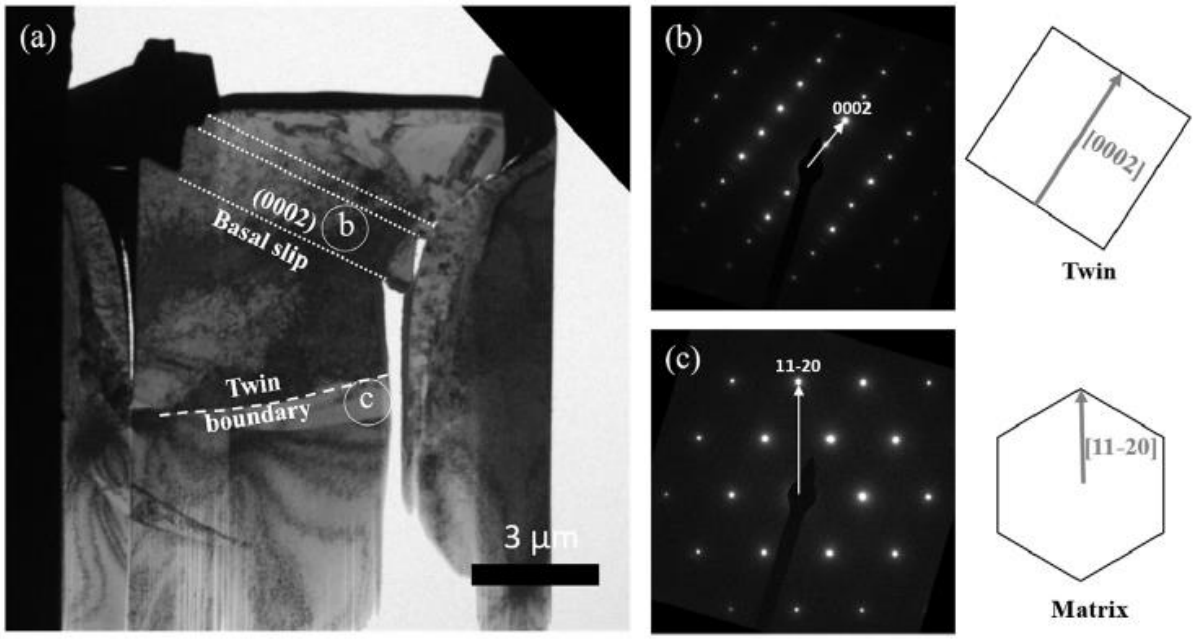

Figure 2.9: Post-mortem images of a deformed microcrystal at 100°C. (a) cross-sectional TEM image, (b) and (c) are SADP's corresponding to ⓑ and ⓒ regions of (b)[40]

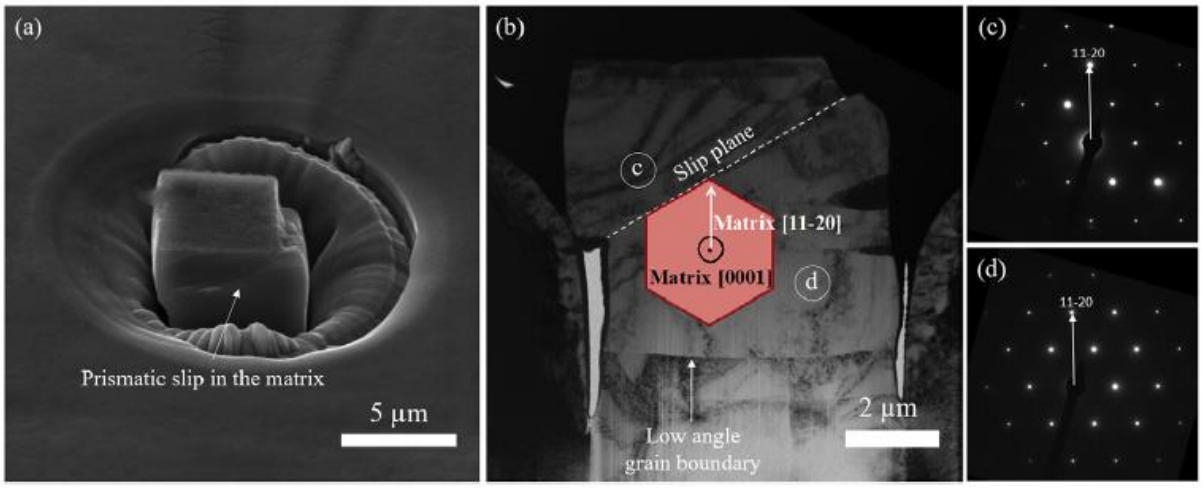

Figure 2.10: Post-mortem images of a deformed microcrystal at 150°C. (a) SEM image, (b) cross-sectional TEM image, (c) and (d) are SADP's corresponding to ⓒ and ⓓ regions of (b)[40]

In the most recent studies of in-situ SEM/TEM micro-pillar compression along <$2\bar{1}\bar{1}0$>, the authors found a relationship between sample size and activation of prismatic <a> slip, and twin nucleation and growth [38], [40]. In both studies $\{10\bar{1}2\}$ tensile twinning was observed to be the dominant deformation mode up to a pillar size of 500 nm. However, Sim et al. [41] performed Molecular Dynamics simulation using LAMMPS [41] employing the EAM potentials of Liu et al. [42] with smaller-sized pillars (>120 nm). Their simulation results predicted the activation of prismatic <a> slip without any hint of twinning [40]. They related this change in deformation mode to the rate at which twin nucleation stress increases with a decrease in crystal/pillar size as compared to the CRSS for prismatic <a> slip; the rate of increase is lower in the latter case. Hence, below a certain crystal/pillar size, a transition in deformation modes takes place and prismatic <a> slip becomes activated in preference to tension twinning for the same loading direction. However, they did not explain the role of strain rate in such a transition as they performed their simulations for a strain rate of $9x10^{9}\ s^{-1}$ which is very large compared to the experimental strain rate of $10^{-3}\ s^{-1}$. So it is not clear whether it was the strain rate or the sample size which played the more critical role in the transition of deformation mode from $\{10\bar{1}2\}$ tensile twinning to prismatic <a> slip [40]. Jeong et al. [39] gave a more logical explanation of this transition in deformation modes based on the change of role of pre-existing prismatic <a> dislocations in subsequent plastic deformation during a-axis compression as a function of sample size. During a-axis compression, the pile-up of pre-existing prismatic <a> dislocations acts as a source of stress concentration that leads to the nucleation of twins. The mobility of the screw and edge parts of a prismatic <a> dislocation loop are different at room temperature as the mobility of the screw part is lower due to the higher Peierls stress [43]. As a result, screw arms of the dislocation loop become immobile, and can annihilate and edge part moves a little ahead, forming a half loop, but being caught up by the incoming

edge part hence created a pile-up. The area in front of these piled-up dislocations is highly stressed and is hence a potential site for twin nucleation and growth. In addition to prismatic <a> dislocation pile-up, the additional factors of cross-slip between prismatic and basal planes, stacking fault generation and dissociation of edge prismatic dislocations into partial dislocations are also affected by the sample size. So, as the sample size decreases, the pre-existing prismatic <a> dislocations will decrease which ultimately reduces the chances of their pile-up and dissociation into partial dislocations hence becoming potential sites for local stress concentration are decreased. As a result, the chances of twin nucleation are decreased. On the other hand, these pre-existing prismatic <a> dislocations become mobile under high local shear stress and act as dislocation sources hence promoting dislocation slip processes [38].

2.3.1.3 Pyramidal <c+a> slip

Pyramidal <c+a> slip is an important deformation mode in magnesium as it facilitates deformation along "**a**" and "**c**" directions simultaneously. Pyramidal <c+a> slip takes place by the activation of <c+a> dislocations either on pyramidal I $\{10\bar{1}1\}$ planes or pyramidal II $\{11\bar{2}2\}$ planes. However, its activation is not very straightforward due to its higher CRSS values as compared to other slip and twinning modes in magnesium. At room temperature, the CRSS value of pyramidal <c+a> slip is about 100 times more than that of basal <a> slip and $\{10\bar{1}2\}$ tension twinning [28], [44]. So, to activate pyramidal <c+a> slip, loading is applied in such a manner that resolved shear stress on other slip and twinning planes must either be zero or very near to zero [29].

In the past, there have been many studies on the activation of <c+a> dislocations in magnesium [15], [18], [34]–[36], [44]–[56], but only a few presented the detailed post-mortem dislocation structure [44], [50]–[52]. In these publications, activation of pyramidal <c+a> slip is achieved

by compression along the c-axis [15], [18], [37], [50], [51], [55]–[58]. However, there are some reports of activation of $\{10\bar{1}1\}$ compression twinning during c-axis compression [59]–[61] and in some other reports simultaneous activation of both deformation modes have been reported [44], [62].

Due to the significance of pyramidal <c+a> slip in the homogeneous shear of magnesium and magnesium alloys, extensive research has been carried out with a focus on the source mechanisms for <c+a> dislocations [63]–[65], dissociation of <c+a> dislocations [50], [51], identification of the preferred glide plane [44], [51]–[53], [66] and the cross-slip mechanism for <c+a> dislocations [50], [67]–[69]. All these factors ultimately influence the strength, ductility and hardening properties of this HCP metal resulting from the activation of <c+a> dislocations.

Two hypotheses exist for the source mechanism of <c+a> dislocations. The first model was presented by Yoo et al. [63], who proposed separating the <c+a> source mechanism into three steps as shown in Figure 2.11.

Step-1, cross-slip of <a> type dislocations from the basal to a prism plane.

Step-2, transformation of this <a> dislocation into a <c+a> dislocation after combining with a pre-existing <c> dislocation in the prism plane. And

Step-3, finally cross-slip of this screw segment of <c+a> dislocation from the prism to pyramidal II plane.

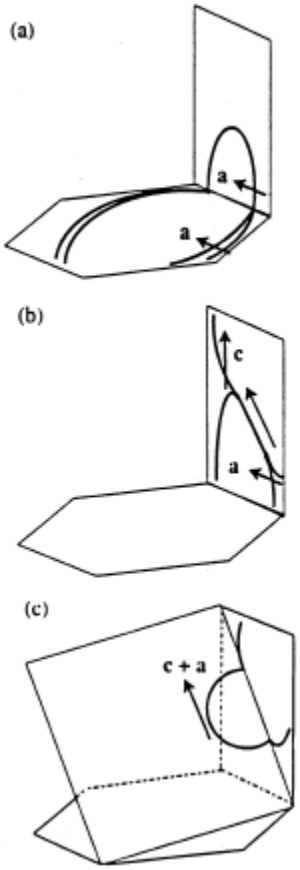

Figure 2.11: Steps involved in the evolution of a <c+a> dislocation (a) Cross-slip of <a> dislocation from the basal plane to the prism plane (b) formation of <c+a> dislocation junction on the prism plane and (c) cross-slip of <c+a> dislocation from prism plane to pyramidal II plane [63]

Later in 2014, Tang et al. [70] proposed another model for the source mechanism of <c+a> dislocations after performing MD simulations of c-axis compression of magnesium single crystals using the LAMMPS code [41] with magnesium interatomic EAM potentials developed by Liu et al. [42] and Sun et al. [71]. Their simulation results indicated that an individual <c+a> dislocation is formed on a pyramidal I $\{10\bar{1}1\}$ plane through the sequential emission of two partial dislocations in the same plane. However, there is no experimental evidence available for this source mechanism, nor for the one proposed by Yoo et al. [63]. Tang et al. [70] also reported

that during c-axis compression, plastic deformation initially takes place by motion of <c+a> dislocations on pyramidal I$\{10\bar{1}1\}$ planes; cross-slip from pyramidal I $\{10\bar{1}1\}$ to pyramidal II $\{11\bar{2}2\}$ plane takes place at the later stage of deformation and finally, subsequent deformation takes place by glide of <c+a> dislocations on a pyramidal II $\{11\bar{2}2\}$ plane [70]. They also reported the formation of <a> dislocations on pyramidal I $\{10\bar{1}1\}$ plane as a result of a reaction between two <c+a> dislocations [70] which was also previously observed by Reedhill and Robertson [32] during a-axis compression at higher temperatures. Their results were in good agreement with experimental observations showing <c+a> slip activity on the pyramidal II $\{11\bar{2}2\}$ plane [44], [47], [52], [55] and also provide an explanation of the prevalence of theoretical predictions of <c+a> slip on pyramidal I $\{10\bar{1}1\}$ planes [53], [70], [72]–[74].

Since <c+a> Burgers vector is large, it undergoes dissociation reaction to transform into a stable configuration. The interaction of gliding <c+a> dislocations with these dissociated products then provides the basis for higher work hardening and limited ductility during c-axis compression of magnesium single crystals at room temperature [44], [50], [53]. There were two possible dissociation reactions reported in the past. One such possibility is reported by Frank and Nicholas [75] based on the hard-sphere model. They suggested that one $\frac{1}{3}$ <$11\bar{2}3$> dislocation undergoes dissociation reaction to transform into two $\frac{1}{6}$<$20\bar{2}3$> partial dislocations on the pyramidal II $\{11\bar{2}2\}$ plane by the following reaction:

$$\frac{1}{3}[11\bar{2}3] \rightarrow \frac{1}{6}[20\bar{2}3] + \boldsymbol{SF}(11\bar{2}2) + \frac{1}{6}[02\bar{2}3]$$

But their explanation was contradicted by Stohr et al. [52] who reported dissociation of edge type $\frac{1}{3}$ <$11\bar{2}3$> dislocation into two $\frac{1}{6}$ <$20\bar{2}3$> partial dislocations on the basal plane rather than the pyramidal II plane as proposed by Frank and Nicolas [75].

The other possible dissociation reaction was proposed by Agnew et al. [51] based on their TEM observations which was later confirmed by Geng et al. [50] through their TEM results. Agnew et al. [51] suggested that the <c+a> dislocation dissociates into <c> and <a> dislocations as shown in Figure 2.12. The TEM observations of Geng et al. [50] were a little different from the observation of Agnew et al. [51] in the sense that they did not observe a junction of <c+a>, <c> and <a> dislocations, instead they observed <c+a> and <c> dislocations, as shown in Figure 2.13, possibly due to further glide of the <a> dislocation on the basal plane or further decomposition of this <a> dislocation into two partials on the basal plane with a stacking fault enclosed, as shown in Figure 2.14. So, the overall reaction would be:

$$\frac{\mathbf{1}}{\mathbf{3}}\mathbf{<11\bar{2}3>} \rightarrow [\mathbf{0001}] + \frac{\mathbf{1}}{\mathbf{3}}\mathbf{<11\bar{2}0>} \rightarrow [\mathbf{0001}] + \frac{\mathbf{1}}{\mathbf{3}}\mathbf{<10\bar{1}0>} + \boldsymbol{SF}(\mathbf{0001}) + \frac{\mathbf{1}}{\mathbf{3}}\mathbf{<01\bar{1}0>}$$

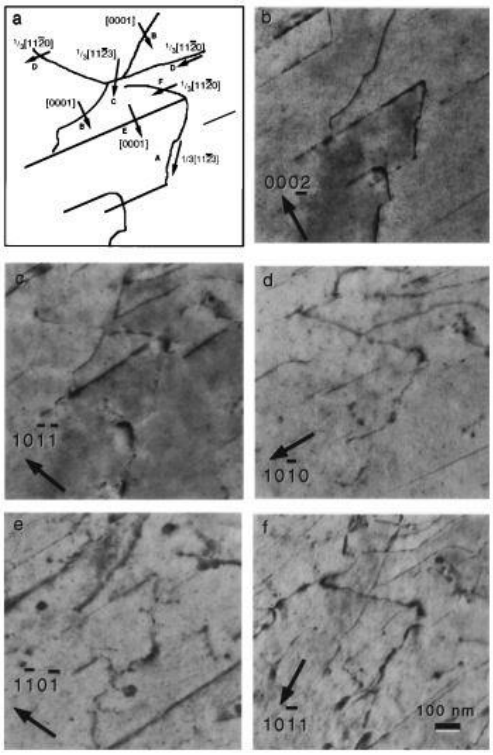

Figure 2.12: TEM images using different g vectors to show the presence of <c+a>, <c> and <a> dislocations as a result of c-axis compression of an α-solid solution Mg-Li single crystal [51]

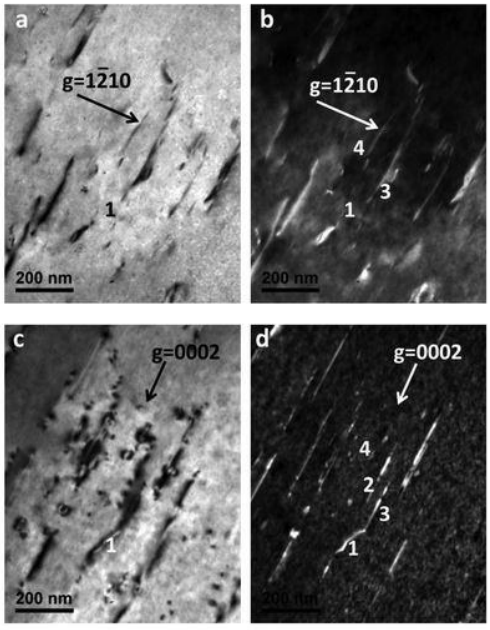

Figure 2.13: TEM images using different g vectors to show the presence of <c+a> and <c> dislocations as a result of c-axis compression of a magnesium single crystal [50]

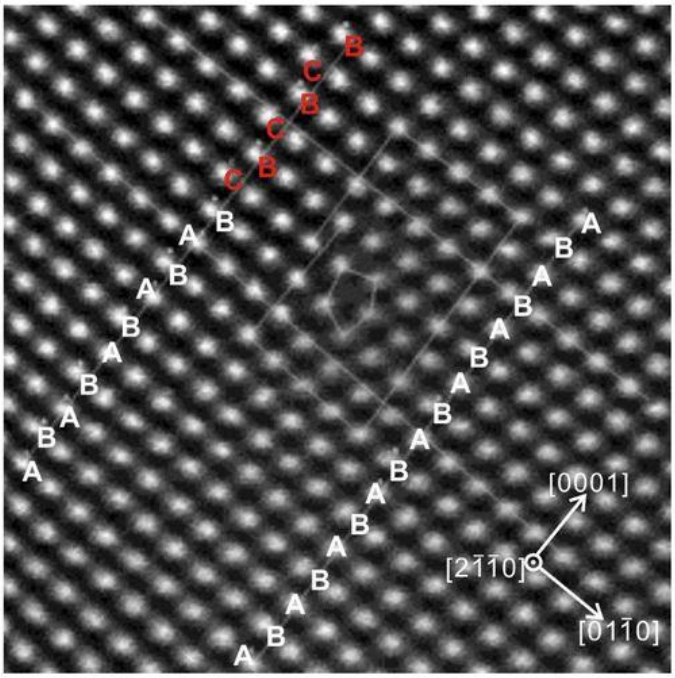

Figure 2.14: TEM-HAADF image showing a 1/3[0$\bar{1}$10] partial dislocation with stacking fault ABABCBCB from a magnesium single crystal compressed along the c-axis [50]

Another important feature of the activation of pyramidal <c+a> slip is the presence of straight <c+a> dislocation segments aligned along the basal plane trace as shown in Figure 2.12 and Figure 2.13 [50], [51]. These straight <c+a>dislocations are reported to be the edge segments which are left behind as debris due to their relatively slower mobility than that of their screw counterparts [50]. These straight edge segments were believed to be immobile in nature. However, a recent in-situ TEM indentation study of Zhang et al. [48] reported some unpinning of these basal dissociated edge segments of <c+a> dislocations that makes them glide further. They also reported limited bowing out of non-basal portions of <c+a> dislocations [48].

Since <c+a> dislocations can glide on both pyramidal I{10$\bar{1}$1} and pyramidal II {11$\bar{2}$2} planes and each pyramidal II plane share a common crystallographic direction of <11$\bar{2}$3> with two of pyramidal I planes, this facilitates double cross-slip of screw <c+a> dislocations from a

pyramidal II plane to a pyramidal I plane and back. Geng et al. [50] observed the frequent presence of edge stepped <c+a> dislocations which are left behind as debris by the double cross-slip of mobile screw dislocations as shown in Figure 2.15. Similar stepped configuration of <c+a> dislocations have been reported by Jain et al. [49] during TEM study of dislocation bands in pure magnesium.

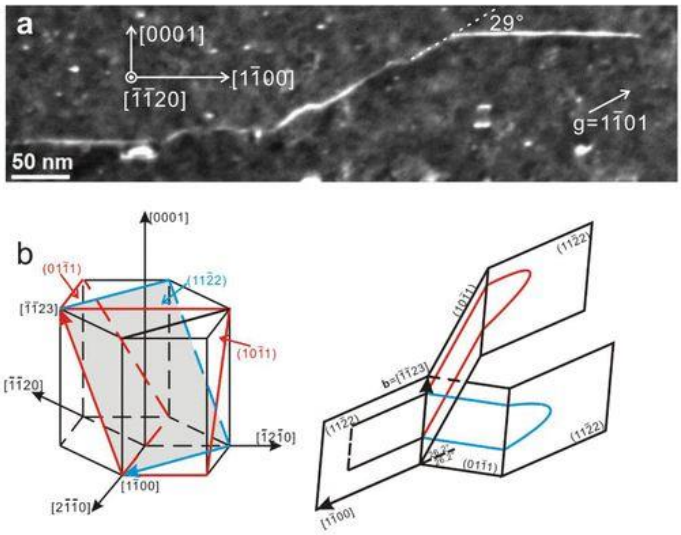

Figure 2.15: (a) DF-TEM image of magnesium single crystal showing double-cross slip and (b) schematic illustration of double cross-slip in magnesium HCP [51]

2.3.2 Deformation by Twinning

A deformation twin is a part of a parent crystal that has been subjected to a displacive transformation to attain a new orientation that has mirror symmetry with respect to the parent crystal [76], [77]. The mirror plane between the twinned region and the matrix is called the twinning plane and the direction of movement of atomic rows to attain a twin orientation is called the twinning direction.

In classical theory, deformation twinning can be described by defining four key twinning parameters K_1, K_2, η_1, and η_2, also known as the twinning elements. Figure 2.16 shows a sphere of bulk material whose top half is transformed into an ellipsoid as a result of homogenous shear due to deformation twinning. K_1 is the first undistorted plane, known as the twinning plane, having the twinning direction η_1. K_2 is the other undistorted plane, having the other crystallographic direction η_2, which is rotated to an angle of 180-4Φ to acquire the final position of K_2 (from A to A_1 in Figure 2.16) and 2Φ is the angle between K_1 and final position of K_2. The plane of shear is the one containing both crystallographic directions η_1 and η_2 and also the normals to the planes K_1 and K_2 [77]. The magnitude of the twinning shear can be calculated as:

$$\mathbf{S = 2\cot(2\Phi)}$$

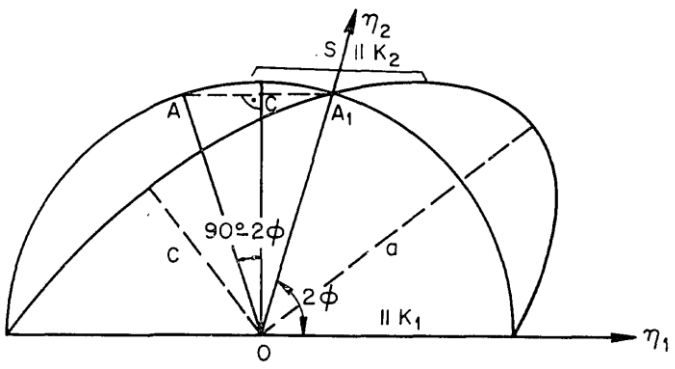

Figure 2.16: Schematic illustration of a twinning event to transform a sphere into an ellipsoid illustrating different twinning elements [77]

Although slip and twinning both involve atomic displacements causing homogeneous shear, there are some key differences between the two modes [78]:

1. During slip, shear displacement always takes place with a magnitude that is an integral multiple of the inter-atomic distance. Whereas, in the case of twinning, the magnitude of shear displacement is not only a fraction of inter-atomic distance, but every plane undergoes shear relative to its neighbouring plane.

2. The shear caused by twinning is always directional or can be termed as irreversible because, for a particular twinning system, the shear taking place along one crystallographic direction is not the same as produced in the opposite crystallographic direction (polar in nature). However, in the case of slip, this is always the case. For example, for an FCC lattice, twinning on (111) can cause shear along $[\bar{2}11]$ but not along $[2\bar{1}\bar{1}]$ whereas slip on (111) can occur equivalently either along [110] or $[\bar{1}\bar{1}0]$ planes.

3. Twinning causes an abrupt reorientation in the crystal lattice whereas deformation by slip takes place gradually.

Twinning plays an important role during plastic deformation in magnesium as it is the second deformation mode after pyramidal <c+a> slip that is capable of accommodating strain along the c-axis and hence makes an important contribution towards mechanical properties such as ductility and hardening.

In magnesium, twinning is the second most common deformation mode after basal <a> slip. Although the contribution of twinning as an independent deformation mode towards the homogeneous shear deformation of magnesium is very limited as it only provides 0.5 independent slip system [15], but it plays a more pronounced role because it reorients the twinned region with respect to the parent crystal in such a manner that it becomes favourable for slip activity which otherwise would not be possible in the parent orientation. Twin boundaries also act as obstacles to gliding dislocations, thus promoting hardening.

Generally, twinning in HCP metals can be divided into two classes: if deformation twinning produces an extension along the c-axis then it is termed tension twinning and if it produces contraction along the c-axis then it is termed compression twinning. So, tension along the c-axis or compression along the a-axis would be the ideal loading conditions to activate extension twinning and vice versa. Experimentally, in the case of magnesium, $\{10\bar{1}2\}<\bar{1}011>$ and $\{10\bar{1}1\}<10\bar{1}\bar{2}>$ are the most common twinning modes observed, although compression twinning along $\{30\bar{3}4\}$, $\{11\bar{2}4\}$ and $\{10\bar{1}3\}$ twinning planes has also been reported at different temperatures [37], [62], [79]–[81]. Ando et al. [82] reported another twinning phenomenon known as a $\{10\bar{1}1\}$ - $\{10\bar{1}2\}$ double twin that leads to fracture at a later stage of deformation above 200°C during c-axis compression of magnesium single crystals. $\{10\bar{1}2\}<\bar{1}011>$ tension twinning is the most common twinning mode irrespective of the orientation of the loading axis with respect to the c-axis and its activity has been reported by several authors [59], [83]–[85]. The reason for its frequent activation is its lower CRSS value (2 - 3 MPa) [79], the second lowest after the CRSS of basal <a> slip in magnesium. The experimentally determined CRSS value for compression twinning is 76 - 153 MPa and 114 MPa [59], [61].

Yoo et al. [9] explained the activation of a particular type (contraction or extension) of twin system (characterised by twinning plane K_1 and twinning direction η_1) in HCP metals with respect to their c/a ratio as shown in Figure 2.17. In Figure 2.17, each solid line is characteristic of a unique twin family, where a positive slope represents contraction twinning and a negative slope represents extension twinning and the filled symbols show the active twinning mode for specific HCP metals. For example, in the case of magnesium with a c/a ratio of 1.624, there is the possibility of activation of $\{10\bar{1}2\}<\bar{1}011>$ tension twins and $\{10\bar{1}1\}<10\bar{1}\bar{2}>$ compression twins which are schematically represented in Figure 2.18 within an HCP unit cell. Both

twinning modes produce nearly the same amount of shear strains, 0.1289 and 0.1377 for tension twin and compression twin respectively. However, these modes cause different crystal reorientations with respect to the same rotation direction. For example, a tension twin cause 86.3 degrees reorientation about <11$\bar{2}$0> direction but a compression twin cause 56.2 degrees reorientation about <11$\bar{2}$0> direction [78].

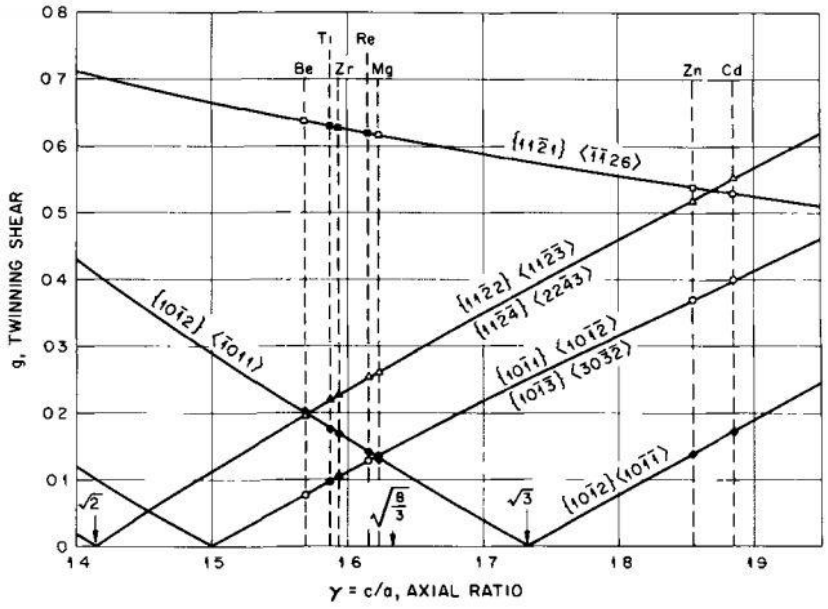

Figure 2.17: Variation of twinning shear with axial ratio (c/a) with various HCP metals indicated [9]

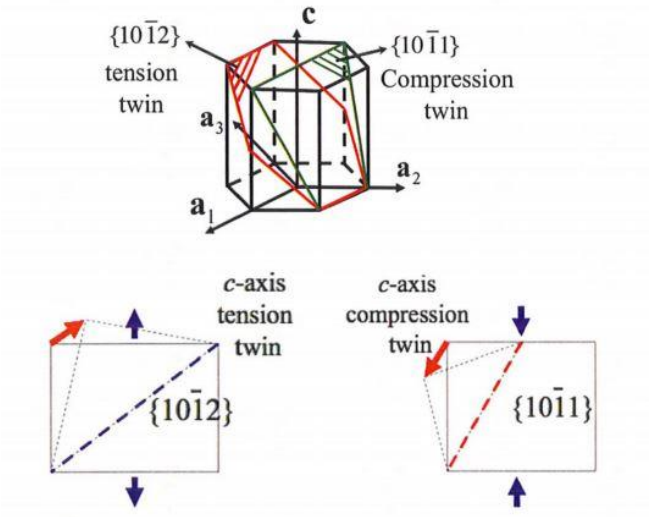

Figure 2.18: Schematic presentation of {10$\bar{1}$2} tension twin and {10$\bar{1}$1} compression twin [86]

There are three stages for a complete twinning event: twin nucleation, twin propagation and thickening of the twin. Twin nucleation is the first stage that occurs when the resolved shear stress along the twinning direction on a twinning plane reaches a critical value due to a highly localised stress concentration [87]. In the next stage, rapid twin propagation takes place by the gliding of twinning dislocations on the twin plane along the twinning direction resulting in the motion of twin boundaries. The stress required for twin propagation is less than for the twin nucleation stress. In the last stage, twin thickening takes place, achieved through long-range stress states by the motion of twin boundaries across the grains in the direction normal to the twinning plane through nucleation and gliding of twinning dislocations [88].

With the introduction of small scale in-situ mechanical testing in the years 2004-2005 by Uchic et al. [5], [30], interest once again shifted to understanding better the different aspects of deformation twinning like the critical stresses associated with the different twinning events and the mechanism for twin nucleation and growth, using real time direct observations of the

microstructural changes as a result of different test conditions [15]–[17], [19], [38]–[40], [89]–[91]. Most of these studies were performed by compression along the basal plane to activate tension twinning whereas there is only one study using tension along the c-axis to activate tension twins [90]. In terms of the experimentally determined twin nucleation stress, Prasad et al. [25] reported a twin nucleation stress of 116 MPa for a 10 μm pillar, Liu et al. [28] reported 50-200 MPa for a 3 μm pillar and Yu et al. [95] reported 800 MPa for a 0.1 μm pillar which follows the general trend of size-effect i.e. the smaller samples exhibit higher CRSS values. In the study of Yu et al. [95], they reported a similar twin nucleation stress for both compression and tension twins which is contrary to previous understanding where a huge difference exists between the nucleation stresses of tension and compression twins. Another interesting observation of a transition from twinning dominated plasticity to slip dominated plasticity during compression along the basal plane has been reported in the literature [39], [40] for small sample (< 200 nm) at room temperature or for temperature greater than 100°C with a sample size of 5 μm.

2.4 Effect of temperature on plastic deformation modes in magnesium

Service temperature plays an important role in defining the mechanical behaviour of any material. During plastic deformation of magnesium, each slip and twinning system is activated along a certain loading direction as predicted by maximum Schmid factor, when the resolved shear stress on a preferred slip or twinning plane surpasses its CRSS value. These CRSS values of the various deformation modes depend upon certain factors like strain rate to some extent and temperature to a great extent. So, a thorough understanding of the effect of temperature on the CRSS values of different deformation modes in magnesium is important not only in describing the overall mechanical behaviour of this HCP metal, and its alloys, but also helpful

in the development of an improved design strategy by predicting a forming temperature (other than room temperature) where the optimum balance between ductility and strength could be achieved. In this regard, there have been few studies of the temperature dependence of individual deformation modes in magnesium which are summarised below.

The effect of temperature on the CRSSs of different deformation modes in magnesium single crystals has been studied using different experimental techniques like uniaxial tension, uniaxial compression, shear testing and plane-strain compression [23], [24], [26], [28], [32], [36], [37], [39], [44], [45], [47], [61], [62], [92]–[95]. In this regard, there exists controversy about the different CRSS values reported for the same deformation mode at the same temperature. At room temperature, the CRSSs for basal <a> slip and pyramidal II<c+a> slip were found to vary between 0.5 MPa to 40 MPa and 40 MPa to 110 MPa respectively [16], [26], [44], [94], [96]. The different sample sizes used in these investigations led to this discrepancy in CRSS values.

The temperature dependence of individual deformation modes in magnesium has been studied in the temperature range -270°C to 500°C [23], [24], [26], [28], [32], [36], [37], [39], [44], [45], [47], [57], [61], [62], [92]–[95]. The CRSSs of prismatic <a> slip, pyramidal II <c+a> slip and compression $\{10\bar{1}1\}$ twinning are reported to be more temperature dependent than those of basal slip and $\{10\bar{1}2\}$ tension twinning (Figure 2.19 and 2.20). It is clear from Figure 2.19, that the CRSSs of prismatic <a> slip, pyramidal II<c+a> slip and $\{10\bar{1}1\}$ compression twinning decrease with increase in temperature from room temperature to 450°C whereas no significant change in the CRSS of basal <a> slip and $\{10\bar{1}2\}$ tension twinning is obvious in this range of temperatures. Further, the trends of variation in CRSS values for different slip and twinning systems within the same temperature range are reported to be different [37], [44], [57]. Observations of Stohr et al. [57] differed in the case of pyramidal II <c+a> slip system, where

they reported an increase in CRSS values from room temperature to 100°C and no change in CRSS value from room temperature to -73°C whereas Obara et al. [44] and Ando et al. [37] reported a decreasing trend in CRSS value from room temperature to 100°C and from room temperature to -70°C as well (Figure 2.20). The reason behind this opposite trend in CRSS values for pyramidal II <c+a> slip is unclear.

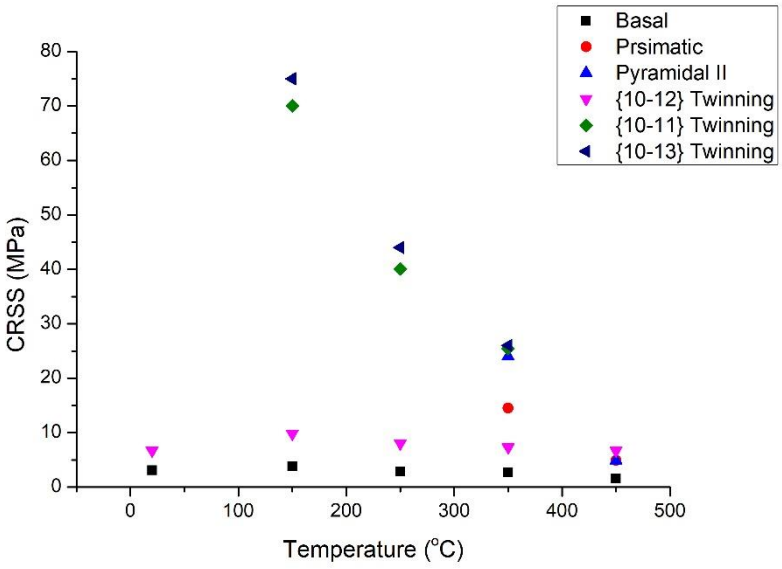

Figure 2.19: Variations in CRSS values of different slip systems with temperature under plane strain compression [94]

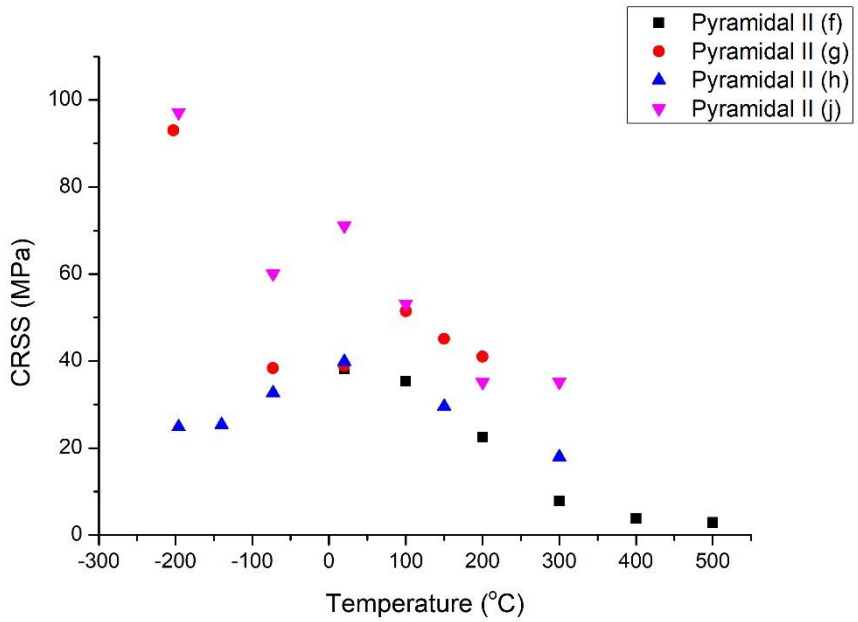

Figure 2.20: Variations in CRSS values of pyramidal II <c+a> slip system with temperatures as reported by (f) Obara et al. [44], (g) Stohr et al. [57], (h) Ando et al. [45], and (j) Ando et al. [37]

The discrepancies mentioned above are mainly attributed to the different testing conditions like strain path and specimen size. In the past, multiple studies were made on the temperature dependence of different slip systems in magnesium, but the testing conditions were quite different from one to another. Moreover, each study was limited to the temperature dependence of one type of slip or twinning system whereas other types of slip and twinning systems were not studied under the same testing conditions. So, to establish the role of temperature in the overall deformation process of magnesium, the activation of all possible slip systems should be tested individually under similar testing conditions over the same temperature range. Previously, Chapuis and Driver [94] conducted a systematic study in which they analysed basal <a>, prismatic <a>, pyramidal II <c+a> slip, $\{10\bar{1}2\}$ tension twinning, and $\{10\bar{1}1\}$ compression twinning individually at same size scale, strain rate and strain path in the

temperature range from 0°C to 450°C. But that study was under plane strain compression which imposes additional friction to the activation of individual deformation modes, hence resulting in higher observed CRSS values. Similarly, Bhattacharya [28] performed uniaxial tension testing on magnesium single crystals for the activation of basal <a>, pyramidal II<c+a> slip and $\{10\bar{1}2\}$ tension twinning from room temperature to -260°C. But there is no systematic study of the temperature effect on individual slip or twinning systems under uniaxial compression either above room temperature or for cryogenic temperatures.

Another aspect of the deformation behaviour of magnesium is work hardening which is also dependent upon working temperature [26]. Typically, deformation by basal <a> slip exhibited very little change in work hardening as the deformation proceeds. But the presence of inherent defects like dislocations, impurity atoms and interactions between pre-existing dislocations would lead towards a typical increasing trend in work hardening. As a result, interaction, pinning, and entanglement among dislocations increase before they annihilate. Thus, higher stress is required to propagate and activate new and harder slip systems, resulting in more work hardening. A comprehensive TEM analysis of deformed specimens can reveal the dislocation structure developed during different stages of work hardening to explain the sources of work hardening in different crystal orientations at different test temperatures.

Considering the above discussion, there is a need for a systematic experimental investigation of the effect of different working temperatures on the activation of individual deformation mode in magnesium single crystals under the same testing conditions to develop a clear understanding of this phenomenon. To study the effect of temperature on the activation of different slip and twinning systems, the test conditions of sample size and strain path must be identical for different crystal orientations favouring for the individual slip or twinning mode. In this regard,

in-situ micro-compression testing is a very useful technique to get very precise data for stress and strain at a very high resolution of applied force and the resultant displacement. This type of experimentation can provide an accurate set of CRSS values at different temperatures for different slip and twinning modes which then could be utilized to model the deformation behaviour of polycrystalline magnesium and alloys at different temperatures.

2.5 Micro-pillar compression

Micro-pillar compression is an effective way to study the property structure relationship within small confined volumes of a wide range of materials. In this technique, FIB-made pillars of micro-metre to nano-metre size ranges are compressed inside an SEM and/or TEM by using a flat punch nanoindentation system, generating uniaxial compressive stress inside the pillars to cause plastic deformation of the pillars. As a result, physical changes in the dimensions of the pillars are recorded as a function of applied load/stress to correlate the underlying plastic deformation and failure mechanisms to corresponding stress and strain levels. Quantitatively, stress vs strain curves are obtained from these experiments. The stress values are obtained by dividing the load by the cross-sectional area of the pillar; the strain values are calculated by dividing the measured change in height of the pillar by the initial height of the pillar.

This technique was first introduced by Uchic et al. [30] to study the sample size effect in single crystal Ni and Ni_3Al-Ta superalloys, leading to the well-known phenomenon of ‘smaller is stronger’ in the field of micromechanical testing. They found that the strength of single crystal Ni was increased three times when the sample size was decreased to 5 μm as compared to the bulk sample whereas the strength of single crystal Ni_3Al-Ta was found to increase 15 times when the sample size was decreased to 0.5 μm as compared to a bulk sample. Since then, this

technique has been utilised widely to investigate the sample size effect and mechanical properties of a wide range of crystalline materials [15], [17], [31], [38], [56], [58], [97]–[117].

In the published literature, most of the size dependent plasticity work is focussed on FCC, BCC and HCP metals. The most recent review on the size effect in micro-pillar compression by Shahbeyk et al. [118] presented a comparison between the size effects observed in these three classes of materials and reported the size exponent for various FCC metals as a global size exponent of ~ 0.6 based on all the previous experimental data. However, for BCC and HCP metals, no such global size exponent was reported because of the large scatter in the size exponents for these two classes of metals; their size exponents seem to be affected significantly by crystal orientation, strain rate and test temperature, which is not the case for FCC metals.

There are two generally accepted explanations of the size effects in crystalline materials during micro-pillar compression. The *source truncation* model, which was proposed by Parthasarathy et al. [119]: according to this model, with a decrease in pillar size the free surface to volume ratio increases, resulting in the formation of single arm dislocation sources from double ended Frank-Read dislocation sources due to the dislocations' interaction with the pillar surfaces. Consequently, with a decrease in pillar size, the length of these new dislocation sources also decreases, resulting in higher strength in a smaller sample.

The second model is known as *dislocation starvation* or *source exhaustion* as proposed by Greer et al. [101], [114]. This model is based on the view-point that the dislocation sources become scarce inside a confined volume due to the escape of mobile dislocations from the pillar free surfaces under the influence of applied stress. Consequently, the pillar becomes dislocation starved. To sustain further plastic deformation, the activation of harder dislocation sources or

the generation of new dislocations is required, thus leading to higher applied stresses and strength.

Micro-pillar compression, however, is not limited to studying the size effect in crystalline materials. Many researchers have employed this technique to investigate other aspects of plastic deformation, including the impact of alloying elements, heat treatments, interfaces, temperature and strain rate on mechanical performance, not only in metallic materials but also in other classes of materials of commercial and scientific importance.

In HCP metals, micro-pillar compression work has mainly been limited to Ti [112], [113], [120]–[127] and Mg [16]–[18], [38]–[40], [56], [58], [128] because of their industrial significance as compared to other HCP metals. In the case of Ti, the focus of initial micro-pillar compression research was to better understand the orientation dependent size effect in single crystal Ti and titanium alloys [112], [122], [129]. More recently this has been extended to the role of microstructural constituents on mechanical performance, for example the effect of the morphology/distribution and relative proportions of beta laths on the critical strengths associated with different slip and twinning modes in different titanium alloys [123], [124], [126], [127], [130]–[134].

The literature available on the micro-pillar compression of magnesium single crystals is mainly aimed at the effect of sample size, alloying elements and microconstituents on the critical stresses associated with basal <a> slip, pyramidal <c+a> slip and tension twinning [15], [16], [18], [19], [39], [40], [48], [55], [56], [58], [89], [135], [136]. Kim [15], Ye et al. [17], Byer et al. [18], Prasad et al. [16] and Liu et al. [19] reported an increase in CRSS with a decrease in sample size for basal <a> slip with a size exponent around 0.6. The size effect exponent, however, is reported to decrease with an increase in dislocation density [18], solute content in

the case of solid solution strengthening [136] and test temperature [136]. Kim [15], Kim et al, [89], Ye et al. [17], Prasad et al. [16], Liu et al. [19], Jeong et al. [38], Sim et al. [40] and Sim et al. [39] performed micro-pillar compression on magnesium single crystals along $[11\bar{2}0]$ and reported tension twinning as the main deformation mode, although Sim et al. [39] and Sim et al. [40] reported a transition in deformation mode from tension twinning to prismatic <a> slip with an increase in temperature to above 150°C [39] or a decrease in sample size to below a few hundred nanometres [40]. The size exponent for tension twinning is reported to be ~ 0.9 [15]. Byer et al.[56], Lilleodden et al. [58], Kim [15] and Byer et al. [18] performed compression of magnesium micro-pillars along [0001] to study pyramidal <c+a> slip. The size exponent for pyramidal <c+a> slip is reported to be 0.2 [15].

2.5.1 Variable test temperature micro-pillar compression

Engineering materials are often exposed to temperatures above or below room temperature. Micro-pillar compression has been utilised to evaluate the mechanical performance and failure mechanisms at non-ambient temperatures for a range of materials including metallic materials like Ni [137], Cu [138], W [139]–[141], Ta [140], Fe [142]–[144], Nb [141], [142], V [142], and Sn [145], [146], ceramic materials like YSZ [147] and $MgAl_2O_4$ spinel [148] and laminar-structured materials like Cu-W [149], Al-SiC [150] and Nb-Mg [151] multilayers over a temperature range from -142°C to 600°C. The application of micro-pillar compression under variable temperatures is not, however, straightforward because it requires modifications in the ambient temperature testing equipment such as installing miniaturized heating/cooling systems and temperature measuring components connected to the sample/stage and the indenter tip. There is also the challenge of maintaining the thermal stability of the different components of the indentation system, particularly at the tip/sample contact. Not only is there the management of the thermal drift of the tip materials during micro-pillar compression at non-ambient test

temperature, there is also the question of their chemical and physical stability. The heating systems employed are mainly based upon resistive heating [152] whereas the cooling systems employed are based upon liquid nitrogen [144], [146] or Peltier cooling [153].

Any thermal gradient present between different parts of the nanoindentation system results in some sort of thermal drift, which could lead to misleading test data. So, an effective strategy to address the issue of thermal gradient is key here. To minimise the temperature gradient in different parts of the indentation system, different researchers have employed various methods to keep the thermal gradient as small as possible, particularly at the sample/tip contact [149], [154]. In recent reviews of non-ambient micromechanical testing, authors have discussed at length the possible sources of thermal drift during non-ambient micromechanical testing and listed different ways to achieve a minimal thermal drift rate [6], [152], [155], [156]. Though these review articles are mainly focussed on nanoindentation, where the thermal drift at the sample/tip contact is a bit more serious due to variable contact area during nanoindentation, the overall strategies to tackle the thermal drift presented there are equally applicable to micro-pillar compression as well. The most critical aspect of non-ambient micromechanical testing is to effectively heat/cool both the sample and the tip to minimise the temperature gradient at the sample/tip contact. There are two ways to achieve this: 1. The heater/cooler is attached to the sample or stage only and heating/cooling of the tip is achieved by keeping the tip very close to the hot/cold sample surface for a sufficient period of time prior to the start of the actual test, 2. The heater/cooler is attached to both the sample and the tip independently [152], [156]. In the former case, the contact thermal drift is reported to be as low as 0.1 nm/s to 0.2 nm/s for test temperatures up to 300°C [148], [150] whereas in the latter case, thermal drift rates smaller than 0.1 nm/s are reported for test temperatures up to 950°C in recently developed elevated temperature nanoindentation equipment [157].

2.6 Summary and Objectives of present work

Despite magnesium being a very attractive choice for light weight transport applications, its usability in such applications requires an in-depth knowledge of its mechanical performance under prevailing service conditions like temperature and strain path. The mechanical performance of magnesium is principally related to the underlying plastic deformation processes based on the simultaneous activation of the three most dominant deformation modes of basal <a> slip, pyramidal <c+a> slip and tension twinning to satisfy the von Mises criterion. However, the activation of these individual deformation modes in magnesium is orientation dependent and is affected by the temperature. In the past literature, there are quite a few studies exploring the effect of temperature on these individual deformation modes in magnesium single crystals using different experimental techniques. Most of these studies are for temperatures above the room temperature whereas only a few are reported for sub ambient temperature. These sub-ambient studies were carried out on millimetre sized specimens and in a range well below the practical range of service temperatures. Even in these studies, there still exists controversy over the variation of critical strengths with temperature. The past literature is therefore lacking in a systematic comparative study of these commonly observed individual deformation modes under similar test conditions of testing method, loading rate and sample size within the practical range of sub-ambient service temperature.

In the recent past, various authors have used micromechanical testing to clarify the role of sample size, solid solution strengthening and precipitate strengthening on the activation of different slip and twinning modes in magnesium single crystals. In this regard, the field of temperature dependent micron-scale plastic deformation in magnesium is not very well studied due to challenges associated with non-ambient test temperatures. The studies available are for

above room temperature and only related to basal <a> slip and tension twinning; no work is reported for these two deformation modes at the micron scale sample regime in the sub-zero temperature range. Interestingly, there is no small length scale work reported for temperature dependency of pyramidal <c+a> slip, either above room temperature or in the sub-zero temperature range.

Keeping in view the above mentioned research gaps, the present research was designed to carry out a systematic study on the effect of temperature on commonly observed deformation modes in magnesium single crystals at the micron length scale in the practical range of cryogenic test temperatures. This study aimed at the precise measurement of CRSS values as a function of test temperature for the activation of different slip and twinning modes at room temperature and below. The micro-pillar compression technique was used here to activate basal <a> slip, pyramidal <c+a> slip and tension twinning in the temperature range between 23°C and -95°C. For low-temperature testing, a novel cryogenic stage was designed to be used in conjunction with an already available SEM-based indentation system. Finally, post-mortem SEM/TEM microstructure analysis was performed to relate the underlying deformation mechanism with the test temperature. The data thus obtained is the first to include the CRSS values for different slip and twinning modes in magnesium at a micron length scale in sub-ambient test temperature range and consequently the variation in their CRSS values with temperature.

3 Experimental Procedures

This chapter covers the experimental procedures and techniques used during this research work with an emphasis on the development of a cryo-stage for low-temperature in-situ SEM mechanical testing. In addition to this design part, details concerning the fabrication of micro-pillars from selected grains of polycrystalline magnesium specimens, in-situ micro-pillar compression at different temperatures and post deformation microstructural analysis are explained.

3.1 Sample preparation

Three specimens of ~ 6mm × 6mm × 5mm were cut from vacuum cast commercially pure magnesium (> 99.9% Mg) block using a slow speed diamond cutter to minimise the depth of the deformation layer caused by the cutting process. The overall impurities were less than 0.1 %, which include O, C, Si, and Fe, as determined by SEM EDS (Energy Dispersive X-rays Spectroscopy) by using an Oxford Instrument SDD EDS detector on a Tescan MIRA3 SEM. The specimens were then annealed at 250°C for two hours. These specimens were very carefully mechanically ground and polished using 400, 800, 1200, 2500 grit SiC papers and 1 μm diamond solution. Mechanical polishing was followed by electrolytic polishing using an electrolyte consisting of phosphoric acid and ethanol (3:5 by volume) at 3 volts for 8-10 minutes at room temperature. A freshly prepared electrolyte is essential to avoid any unwanted residual layer on the polished surface. After electropolishing, the specimens were thoroughly rinsed with ethanol followed by ultrasonic cleaning for a few minutes. These were then dried in a jet of air to give a mirror-like surface for the best EBSD signal.

3.2 Grains orientation and Schmid factor

Grain orientations of these electrolytically polished specimens were determined by Electron Back-Scattered Diffraction (EBSD). The data obtained through EBSD was interpreted by HKL Channel-5 Tango software as four-index grain orientations. For this purpose, the Tescan MIRA3 SEM was used which is equipped with an integrated Oxford Instruments EBSD detector and Aztec software for acquisition of the EBSD data. Figure 3.1 shows the positions of the specimen, SEM pole piece and EBSD detector inside the SEM chamber. In this work, a 70-degree pre-tilted specimen holder was used for all the EBSD experiments (Figure 3.2).

EBSD is a very useful technique not only in the context of this research work but also for many other crystal orientations based experimental investigations as it provides very accurate grain orientation data with high spatial resolution. The EBSD experimental set-up is generally installed inside an SEM. During an EBSD experiment, an incident beam of electrons interacts with a metallic specimen and is backscattered out of the specimen due to their elastic interactions with the atoms in the specimen without significant change in their kinetic energy. On their way back out of the specimen, these backscattered electrons are diffracted at different angles corresponding to the atomic arrangements in that specimen. These backscattered diffracted electrons are then collected by the EBSD detector. A set of diffracted electrons striking the detector at angles satisfying the Bragg's condition for diffraction makes a definite pattern of bands like Kikuchi lines as shown in Figure 3.3. Each band in a Kikuchi pattern is representative of a specific crystallographic plane. Based on these Kikuchi patterns, a grain orientation map may be constructed. To obtain the maximum signals from the back-scattered diffracted electrons, the specimen is generally placed at 70 degrees to the axis of the EBSD detector (horizontal axis). This 70-degree specimen position can either be attained by tilting the SEM stage to 70 degrees or by using a 70 degrees pre-tilt specimen holder.

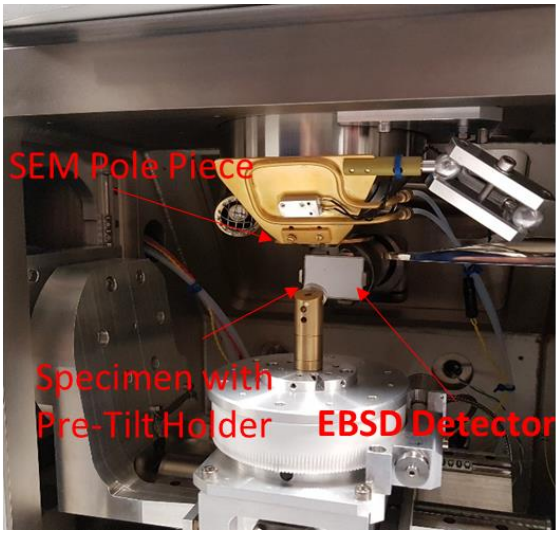

Figure 3.1: EBSD set-up inside Tescan MIRA3 SEM

Figure 3.2: 70 degrees pre-tilt EBSD holder

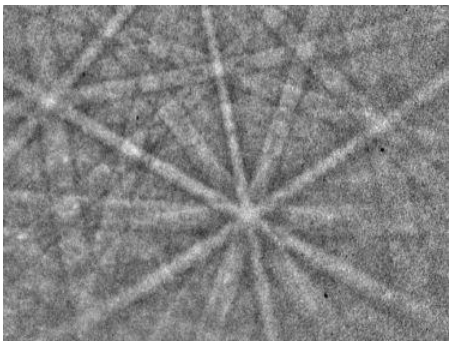

Figure 3.3: EBSD pattern

Based on the acquired EBSD data, one grain on each specimen was found to have a favourable orientation to activate basal <a> slip, pyramidal <c+a> slip or tension twinning. In this regard, a grain with plane normal at 40 degrees to the c-axis of the HCP unit cell was selected to activate basal <a> slip, another grain with plane normal parallel to the c-axis of the HCP unit cell was selected to activate pyramidal <c+a> slip and the third grain with plane normal parallel to the basal plane of the HCP unit cell was selected for the activation of $\{10\bar{1}2\}$tension twinning. The four-index crystal orientations for these three grains were $[11\bar{2}1]$, [0001] and $[1\bar{3}20]$ for basal <a> slip, pyramidal <c+a> slip and $\{10\bar{1}2\}$tension twinning respectively. The selection of the grains was made based on the values of the Schmid factor. The values of the Schmid factor of all possible slip/twinning systems for the selected grains are given in Table 3.1. The relationship used to calculate the Schmid factor is:

$$m = \cos\emptyset \cos\lambda$$

Further,

$$\cos\emptyset = \frac{\left[u_1u_2 + v_1v_2 - \frac{1}{2}(u_1v_2 + u_2v_1) + \left(\frac{c}{a}\right)^2 w_1w_2\right]}{\left[\left({u_1}^2 + {v_1}^2 - u_1v_1 + \left(\frac{c}{a}\right)^2 {w_1}^2\right)\left({u_2}^2 + {v_2}^2 - u_2v_2 + \left(\frac{c}{a}\right)^2 {w_2}^2\right)\right]^{\frac{1}{2}}}$$

$$\cos\lambda = \frac{\left[h_1u_2 + k_1v_2 - \frac{1}{2}(h_1v_2 + u_2k_1) + \left(\frac{c}{a}\right)^2 l_1w_2\right]}{\left[\left({h_1}^2 + {k_1}^2 - h_1k_1 + \left(\frac{c}{a}\right)^2 {l_1}^2\right)\left({u_2}^2 + {v_2}^2 - u_2v_2 + \left(\frac{c}{a}\right)^2 {w_2}^2\right)\right]^{\frac{1}{2}}}$$

where $\emptyset$ is the angle between slip plane normal $[u_1\ v_1\ w_1]$ and loading direction $[u_2\ v_2\ w_2]$, and λ is the angle between slip direction $[h_1\ k_1\ l_1]$ and loading direction $[u_2\ v_2\ w_2]$ [29]*; the c/a ratio for magnesium is 1.624*

Table 3.1: Schmid factor values of the selected grains for different slip and twinning systems

	Slip Plane	Slip Direction	Schmid Factor (m)		
			LD ~ [11$\bar{2}$1]	**LD ~ [0001]**	**LD ~ [1$\bar{3}$20]**
Basal <a>	(0001)	[2$\bar{1}\bar{1}$0]	0.21	0.00	0.00
	(0001)	[$\bar{1}$2$\bar{1}$0]	0.21	0.00	0.00
	(0001)	[$\bar{1}\bar{1}$20]	0.42	0.00	0.00
Prismatic <a>	(10$\bar{1}$0)	[$\bar{1}$2$\bar{1}$0]	0.33	0.00	0.18
	(0$\bar{1}$10)	[2$\bar{1}\bar{1}$ 0]	0.33	0.00	0.31
	($\bar{1}$100)	[$\bar{1}\bar{1}$20]	0.00	0.00	0.49
Pyramidal <a>	(1$\bar{1}$01)	[11$\bar{2}$0]	0.20	0.00	0.44
	(10$\bar{1}$1)	[$\bar{1}$2$\bar{1}$0]	0.39	0.00	0.16
	(01$\bar{1}$1)	[$\bar{2}$110]	0.39	0.00	0.27
	($\bar{1}$101)	[$\bar{1}\bar{1}$20]	0.20	0.00	0.44
	($\bar{1}$011)	[1$\bar{2}$10]	0.20	0.00	0.16
	(0$\bar{1}$11)	[2$\bar{1}\bar{1}$0]	0.20	0.00	0.27
Pyramidal <c+a>	(11$\bar{2}$2)	[$\bar{1}\bar{1}$23]	0.06	0.45	0.19
	(1$\bar{2}$12)	[$\bar{1}$2$\bar{1}$3]	0.08	0.45	0.43
	($\bar{1}$2$\bar{1}$2)	[1$\bar{2}$13]	0.11	0.45	0.43
	(2$\bar{1}\bar{1}$2)	[$\bar{2}$113]	0.11	0.45	0.05
	($\bar{2}$112)	[2$\bar{1}\bar{1}$3]	0.08	0.45	0.05
	($\bar{1}\bar{1}$22)	[11$\bar{2}$3]	0.43	0.45	0.19
	(10$\bar{1}$2)	[$\bar{1}$011]	0.20	0.50	0.02

Tension Twinning	$(01\bar{1}2)$	$[0\bar{1}11]$	0.20	0.50	0.43
	$(\bar{1}102)$	$[1\bar{1}01]$	0.12	0.50	0.28
	$(\bar{1}012)$	$[10\bar{1}1]$	0.14	0.50	0.02
	$(0\bar{1}12)$	$[01\bar{1}1]$	0.14	0.50	0.43
	$(1\bar{1}02)$	$[\bar{1}101]$	0.12	0.50	0.28

3.3 Fabrication of micro-pillar

Square-shaped micro-pillars were fabricated on each of these three grains using Focused Ion Beam milling on a dual-beam FEI Quanta 3D FIB-SEM. This piece of equipment uses Gallium (Ga^+) ions for milling. The micro-pillars were made in steps between which milling current and milling strategy were changed. All the milling process was completed using a 30 kV accelerating voltage with a milling current of 15nA - 0.3nA. Initially, a circular x-section milling pattern was used to excavate a coarse circular-shaped pillar with subsequently decreasing milling currents. Finally, a rectangular x-section milling pattern was employed on all four sides of the pillar achieved by 90 degrees specimen rotation after milling one side. The stage tilt was kept at 52 degrees during the initial coarse milling and 53.5 degrees during final rectangular x-section milling steps. An additional tilt of 1.5 degrees allowed to minimise the micro-pillar taper angle. The final nominal size of the pillar was ~ 5μm x 5μm in x-section with height to width aspect ratio of 2-3. Figure 3.4 shows one of the square-shaped micro-pillar made by the procedure outlined above. A schematic illustration of the dual-beam FIB-SEM is presented in Figure 3.5, which shows the positions of the Electron and Ion sources which are 52 degrees apart and explains the necessity of the stage tilt of 52 degrees during the general FIB milling procedures.

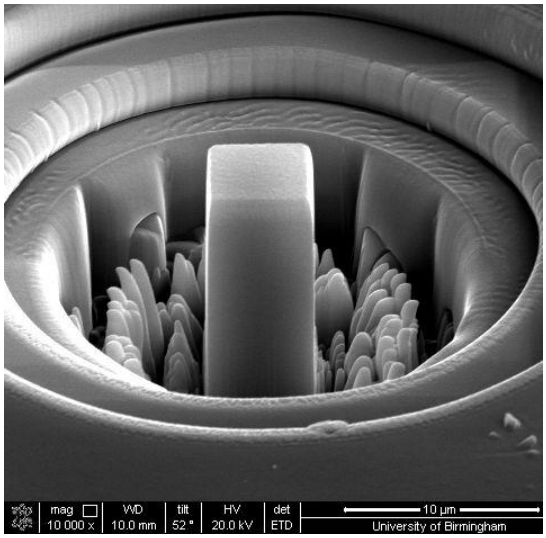

Figure 3.4: SEM images of a square-shaped micro-pillar

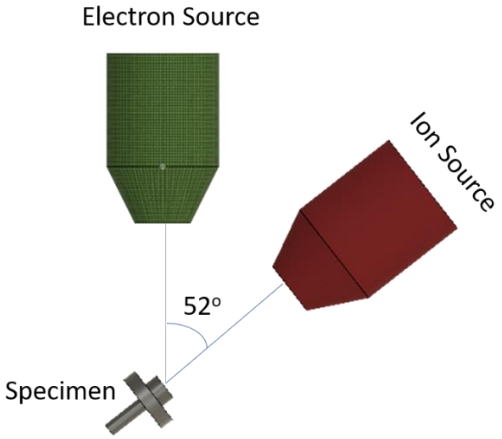

Figure 3.5: Schematic diagram of positions of the specimen with respect to ion and electron sources

3.4 Micro-mechanical testing

After the fabrication of the micro-pillars, the next stage was to perform in-situ SEM compression at room temperature and below. For this purpose, a PI85 Hysitron indentation system was used inside the Tescan MIRA3 SEM. Since the main idea of this research work was

to compare the cryogenic mechanical behaviour of magnesium with room temperature, and the PI85 system is designed for room temperature mechanical testing, so, there was a need to extend the capability of PI85 below the room temperature.

3.4.1 Low-temperature micro-compression set-up

For this purpose, a three-step design strategy was employed to develop a novel cryo-stage for in-situ mechanical testing at cryogenic temperatures and room temperature. The key idea of the design process was to cool down the specimen to the desired cryogenic temperature without cooling the PI85 components especially the piezo-stage motors. Secondly, an accurate temperature measurement directly from the specimen top surface was required.

3.4.2 Step-1: Designing of cryo-stage

In first step, the cryo-stage was designed to be used as specimen holder for the PI85 compression system. It was designed in two parts: the top part was made of highly conductive material to be connected to the cold-finger for specimen cooling and the bottom part was made of highly insulative material to avoid cooling of the PI85 stage piezo-motors. In this regard, pure copper (Cu) was used for the top part and polytetrafluoroethylene (PTFE) was used for the bottom part. Both parts were then screwed together, with a brass screw, through the central holes. All the design work was performed in Autodesk Fusion 360 design software and fabricated in the mechanical workshop of the School of Metallurgy and Materials, University of Birmingham. The initial simplified design of the cryo-stage is shown in Figure 3.6 as version-1 and after fabrication is shown in Figure 3.7. This version of cryo-stage had a brass screw on top of the copper plate for connection to the cold-finger for cooling down the sample. Though this design satisfied the main requirements of the conduction and insulation, it posed a difficulty of specimen attachment to the cryo-stage at the same time. Generally, for room temperature testing, silver paint is used to attach the sample to the stub. But silver paint is not

suitable for the cryogenic conditions as it loses its strength under such conditions. As a result, the initial design was modified in such a way that two side-walls were introduced along the specimen area on the top copper part of the cryo-stage, firstly, to hold the specimen tightly with the help of screws through the holes on the side-walls and secondly, as points of attachment to the cold-finger for cooling down the specimen. The design of the modified version is shown in Figure 3.8 as version-2 and after fabrication in Figure 3.9.

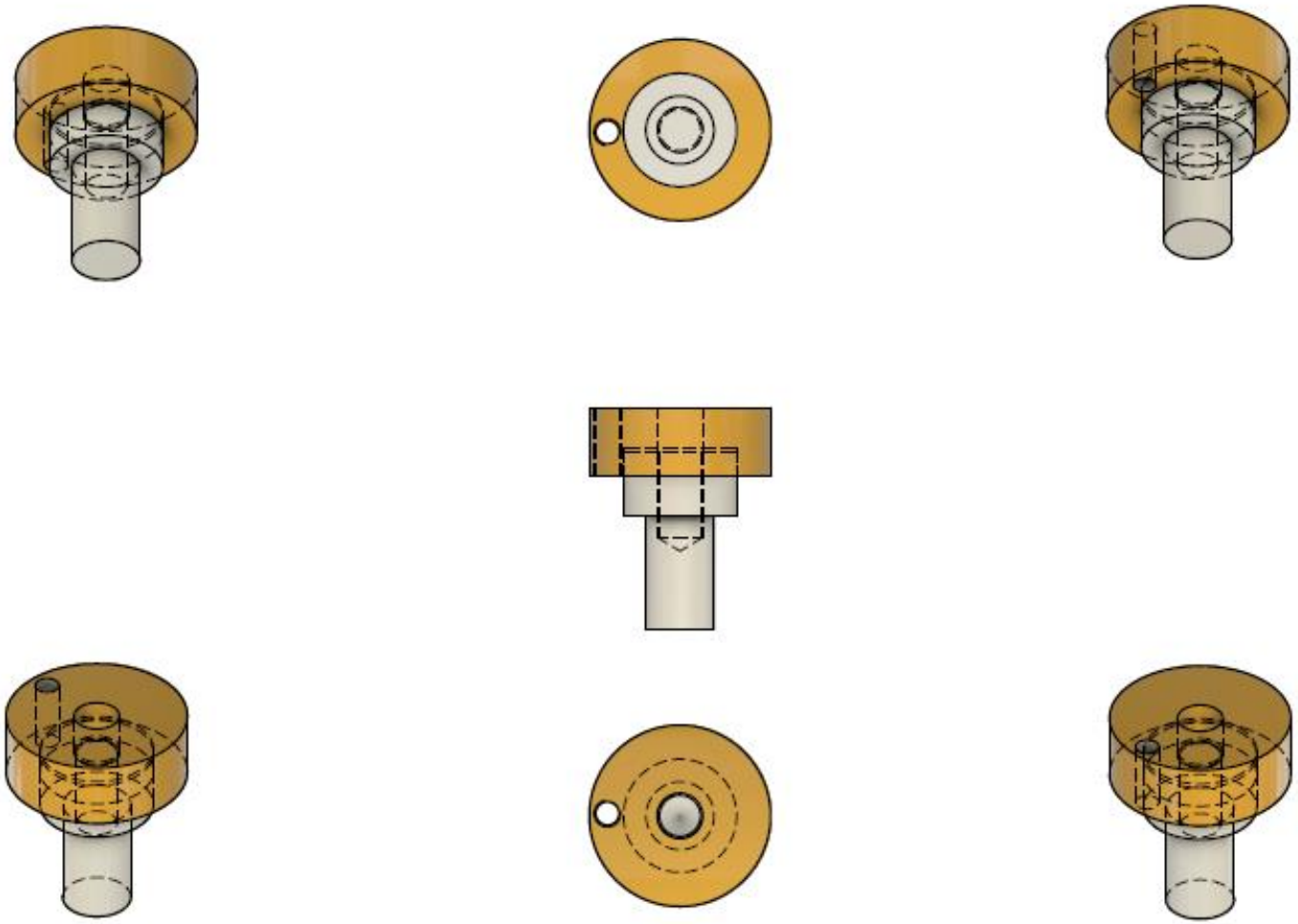

Figure 3.6: Different views of version-1 of the cryo-stage. The cryo-stage was designed using Autodesk Fusion 360 software

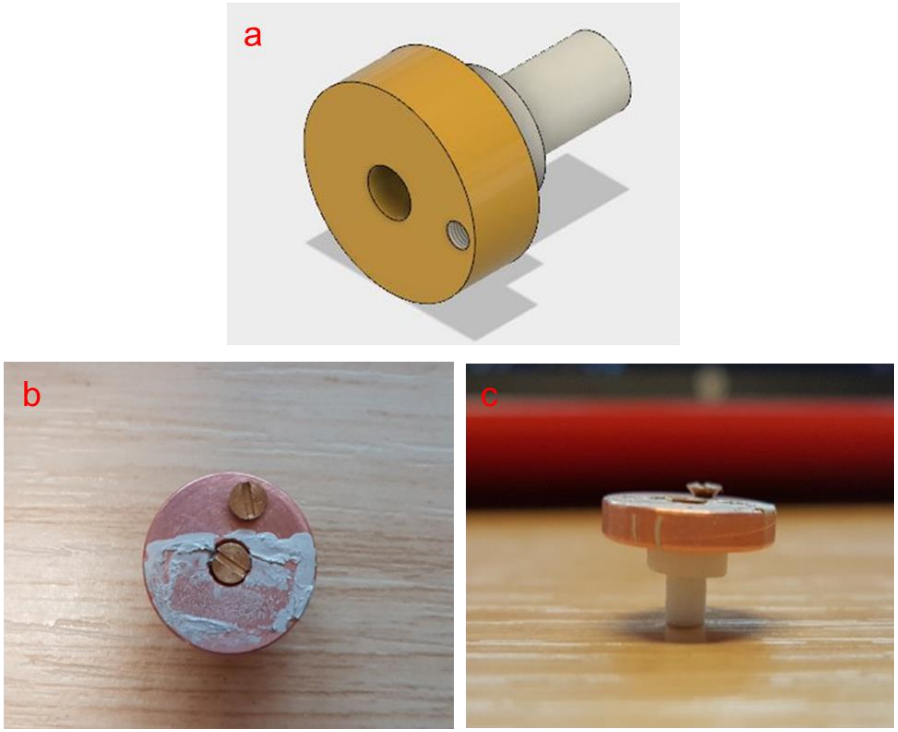

Figure 3.7: (a) 3d view of version-1 of the cryo-stage, (b) and (c) top and side view of the version-1 after fabrication

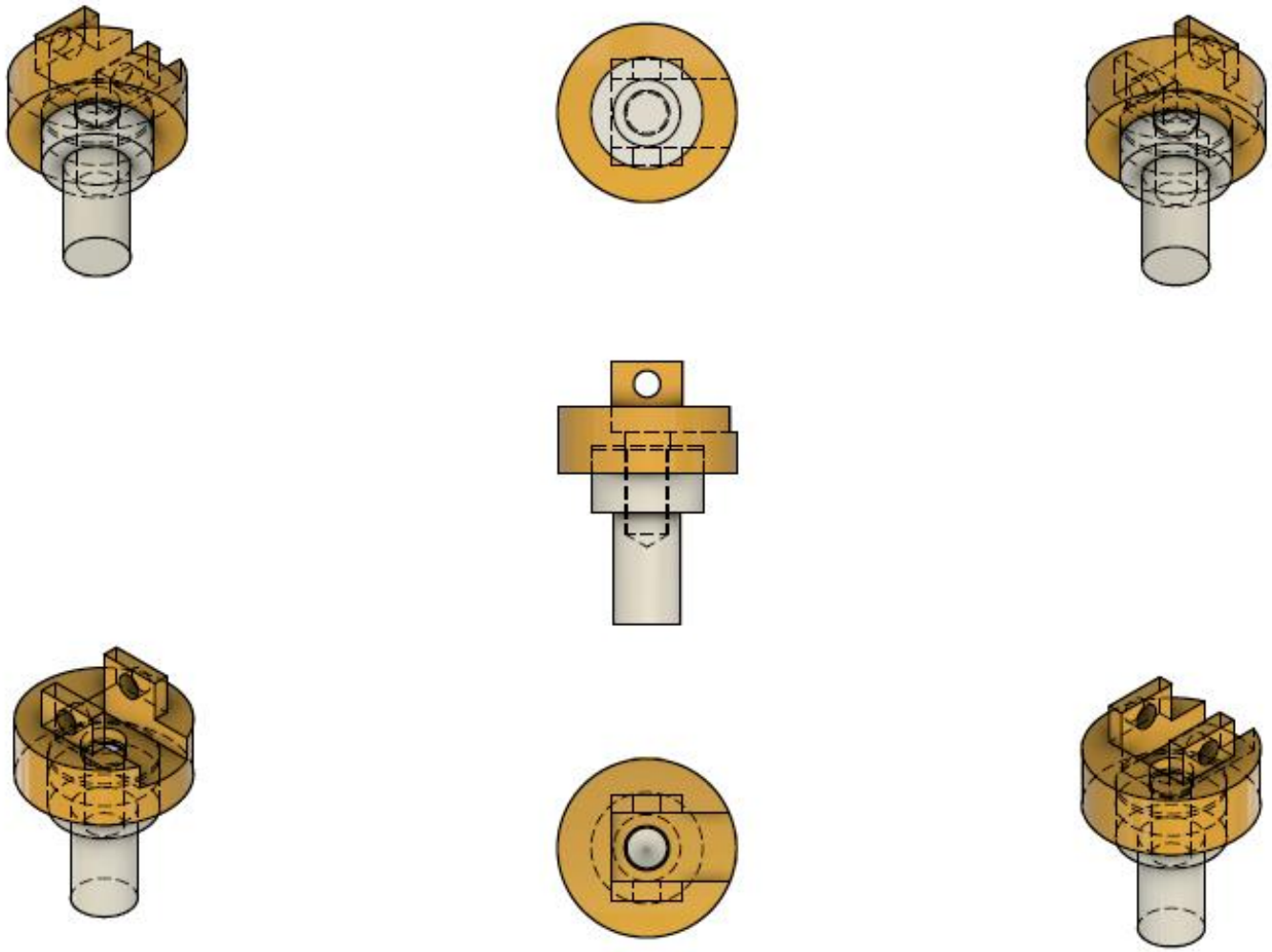

Figure 3.8: Different views of version-2 of the cryo-stage (Autodesk Fusion 360 design software)

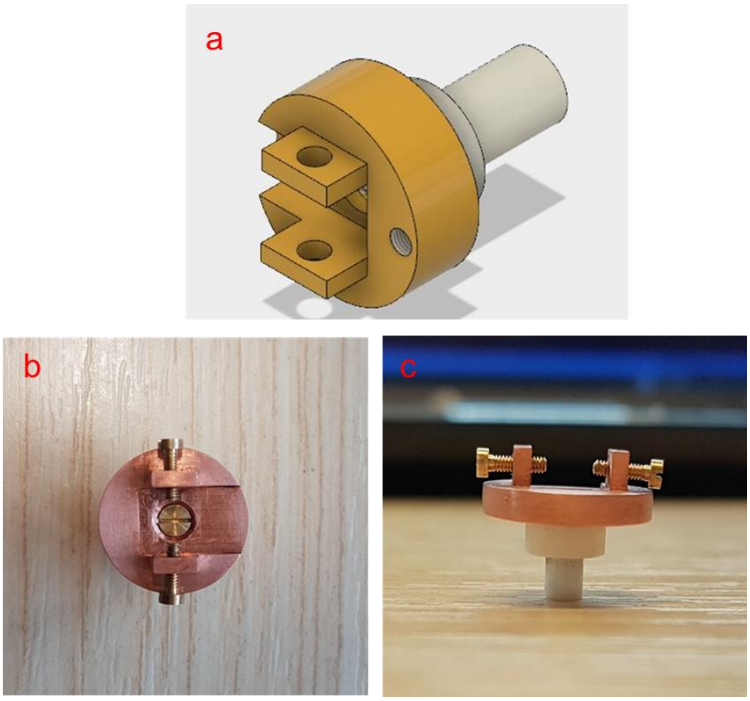

Figure 3.9: (a) 3d design view of the version-2 of the cryo-stage, (b) and (c) top and side views of the version-2 after fabrication

3.4.3 Step-2: Cooling system

The cooling system used was supplied and installed by the Quorum Technologies on the Tescan SEM. This system is based on pressurized liquid nitrogen gas. There are three main parts of it, a dewar for storage of pressurized liquified nitrogen gas, a flow controller for the gas and a cold finger installed near the SEM pole piece as shown in Figure 3.10. The flow controller regulates the flow of pressurized cold gas to the cold-finger, which in turn controls the temperature of the cold-finger. For this work, the cold-finger is attached to the custom built cryo-stage through copper wires to cool down the specimen to a testing temperature.

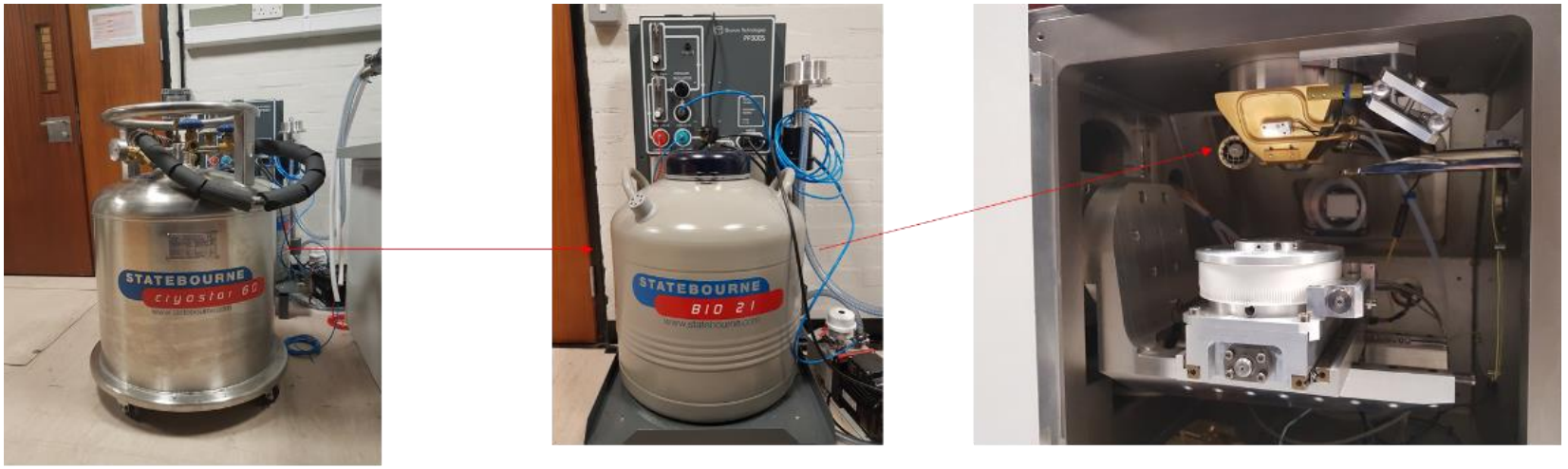

Figure 3.10: Cooling set-up used during the research work to cool down the cold-finger

3.4.4 Step-3: Specimen-temperature measurement

The third step during this overall design process was to install a k-type thermocouple for specimen temperature measurement. This thermocouple needs to be connected to the specimen on one side (inside the SEM chamber) and to a temperature measuring instrument on the other side (outside the SEM chamber). For this purpose, K-type thermocouple feedthrough was installed on one of the SEM ports using a T-shaped extension. This feedthrough was then connected to the thermocouple and temperature measuring instrument by using compensating cables and miniaturised switches. The schematic illustration of the whole fixture is shown in Figure 3.11 and 3d design views of the individual components are shown in Figure 3.12. The SEM port from the outside of the SEM is shown in Figure 3.13 (a-c), initially with a vacuum gauge on it, then without any attachment on it and finally after the attachment of the thermocouple feedthrough and vacuum gauge both together. After the installation of the feedthrough, the SEM chamber was vented and pumped down several times to ensure no vacuum leakage took place. Another important consideration in this experimental set-up was the attachment of the thermocouple to the specimen. For this purpose, a 0.6 mm diameter hole was drilled to 3 mm depth on one side of each specimen and a 0.5 mm thermocouple was then placed in that hole. This sort of thermocouple-specimen attachment also ensured precise specimen temperature measurement.

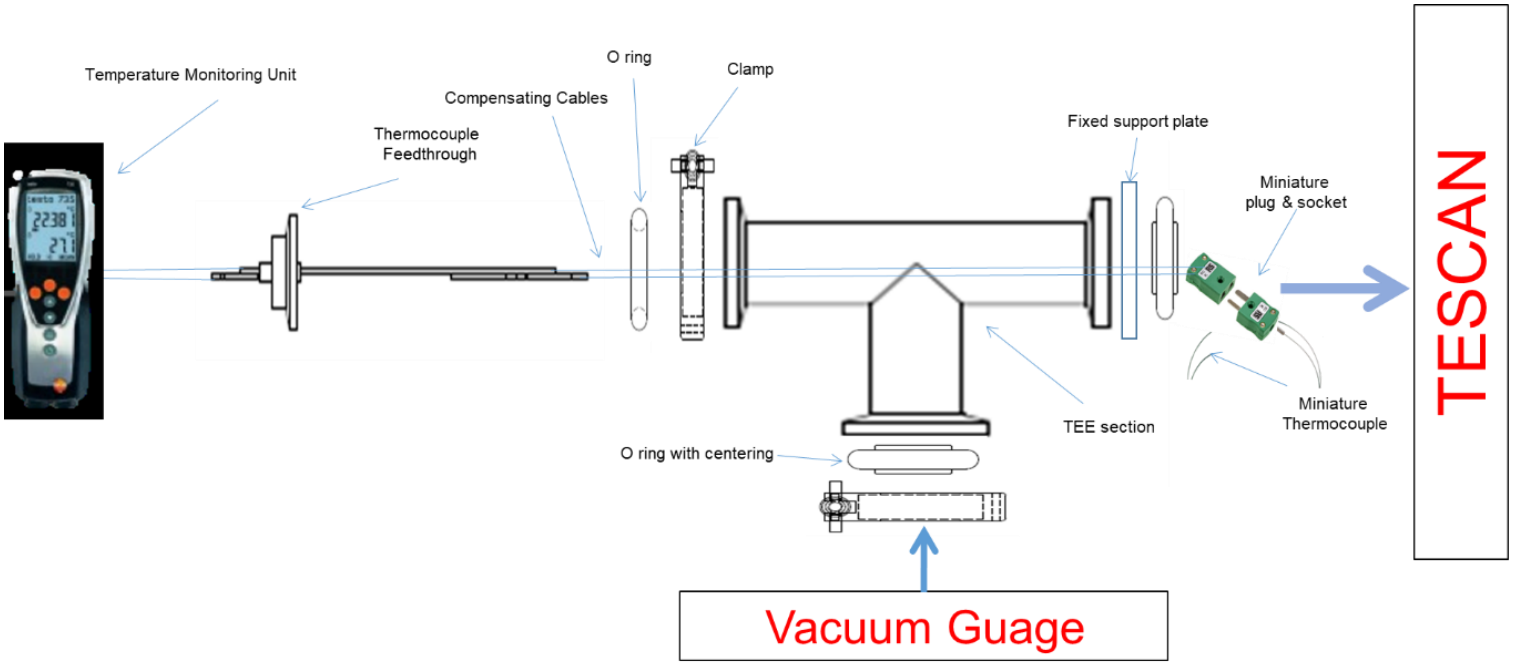

Figure 3.11: Schematic representation of the k-type thermocouple feedthrough on the Tescan-SEM

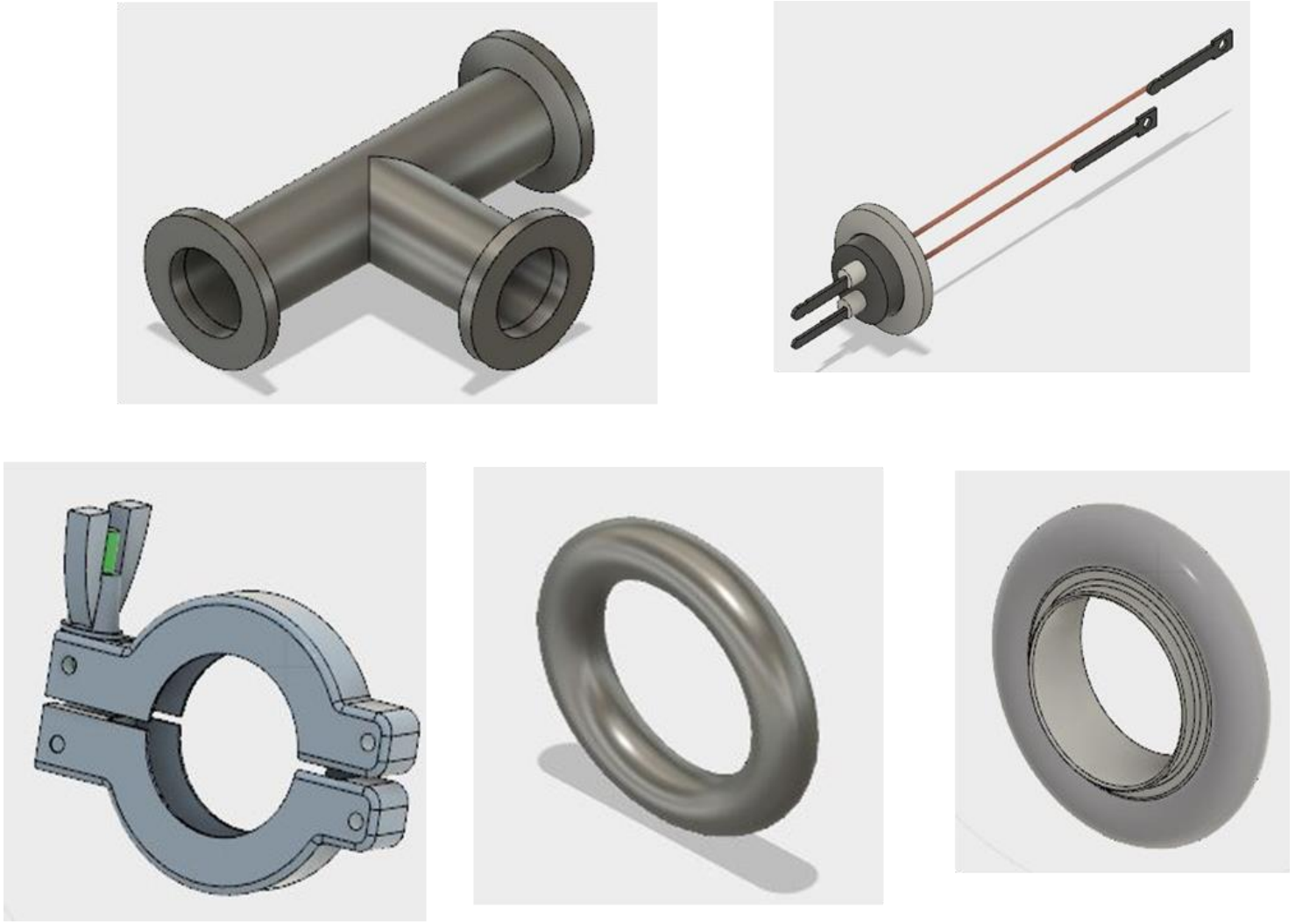

Figure 3.12: 3d models of the different parts used during the installation of k-type thermocouple feedthrough on Tescan-SEM

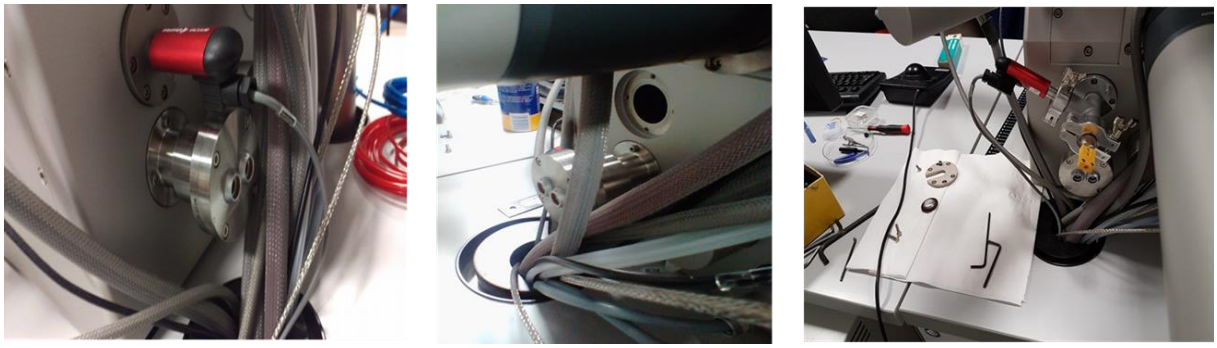

Figure 3.13: Images of the Tescan MIRA3 SEM port (a) with vacuum gauge originally installed on it, (b) without any component on it and (c) after the installation of the thermocouple feedthrough and vacuum gauge

3.4.5 Management of thermal drift

A key challenge during low temperature testing was to minimise the thermal drift that can affect the measured test values of force vs displacement as a result of a temperature gradient between different parts of the indentation system. The PI85 system is ideally designed for room temperature testing and has an in-built automatic drift correction mechanism that monitors variation in displacement for a few seconds at a fixed minor load before to an actual indentation/compression test. The recorded variation in displacement over time is then incorporated into the force vs displacement data recorded during the actual indentation/compression test. In the case of low temperature testing, there exists a considerable big temperature difference between the sample surface and the flat indentation tip that resulted in a very fast-changing drift rate which the PI85 system is not capable of recording accurately and which gave misleading values of drift rate and, hence, an uncertainty in actual test data. To overcome this problem, three approaches were used:

1. During the cooling down of the specimen, the indenter tip was kept very close to the specimen surface to cool the indenter tip as well in a passive manner to reduce the temperature difference between the indenter tip and the specimen surface.

2. The drift rate was manually measured by recording the variation in displacement over time by holding the load at 10% of the peak load for 60 seconds during the unloading stage of the compression test. The drift rate thus calculated was incorporated into the test data. In addition to this 60 seconds holding period for drift correction, a 20 seconds initial hold period was applied during the loading segment of the actual test at 1-2 % of the peak load to further reduce the temperature gradient between the sample surface and the indenter tip. The loading cycle used for all the compression experiments is shown in Figure 3.14.

3. Thirdly and most importantly, to minimise the effect of thermal drift, the duration of the loading segment for individual pillar compression test was kept as small as possible, between 6 – 14 seconds for different maximum peak loads at the same loading rate for the same loading direction during one set of micro-pillar orientation.

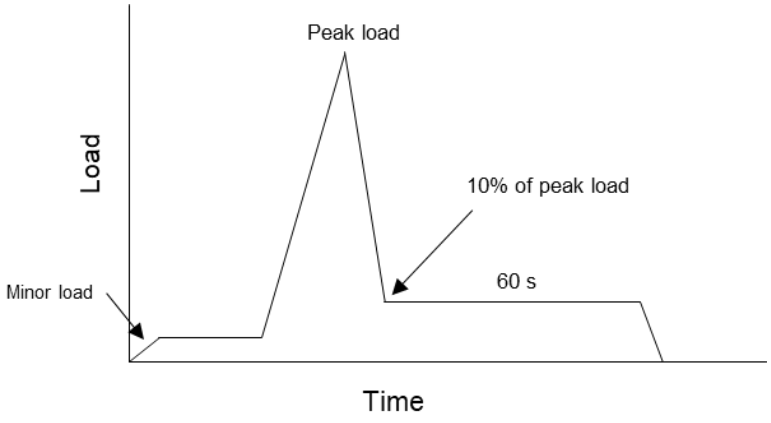

Figure 3.14: Loading cycle used for the micro-compression experiments

3.4.6 Micro-compression testing parameters

The compression of the FIB made micro-pillars was then performed at room temperature, ~ -25°C and ~ -94°C for $[11\bar{2}1]$, [0001] and $[1\bar{3}20]$ oriented pillars using the PI85 indentation system in conjunction with the specially designed cryo-stage inside the Tescan SEM. The complete setup of the PI85 system inside the SEM is shown in Figure 3.15 and the individual components of the PI85 system are highlighted in Figures 3.16 and 3.17, with and without the cryo-stage respectively. The indenter used for the compression was made of diamond and had a conical shape with a flat punching surface. The diameter of the flat punch surface was 20 μm. The positions of the indenter-tip and the micro-pillar just before the micro-pillar compression is shown in Figure 3.18. All the micro-pillar compression tests were performed under load-controlled mode without automatic drift correction and a manual drift correction method was used. Each compression test was performed by following a specific loading cycle as shown in Figure 3.14 and all the experimental parameters are given in Table 3.2. To achieve similar strain rate (of the order of $10^{-3}s^{-1}$) for all the three loading directions, different loading rates were selected accordingly for each loading direction due to the orientation dependent anisotropic plastic behaviour of magnesium single crystals. In the loading cycle, there were two hold periods; the first 10-20 seconds were to reduce the temperature difference between the indenter and the specimen whereas the second hold period was for the measurement of thermal drift as explained in the last section. A typical load vs displacement curve with and without drift correction is shown in Figure 3.19. Finally, true stress vs true strain curves were drawn for each set of experiments. For this purpose, load and displacement data, obtained from the PI85 system, were converted into engineering stress and engineering strain values by dividing with initial cross-sectional area and initial height of uncompressed micro-pillar respectively. These

engineering stress and strain values were then converted into true stress and true strain values using following empirical relationships to draw true stress vs true strain curves.

$$\textbf{\textit{True strain}} = \boldsymbol{ln}\ (\mathbf{1} + \boldsymbol{engineering\ strain}) \quad \textit{and}$$

$$\textbf{\textit{True stress = (engineering stress) x (1 + engineering strain)}}$$

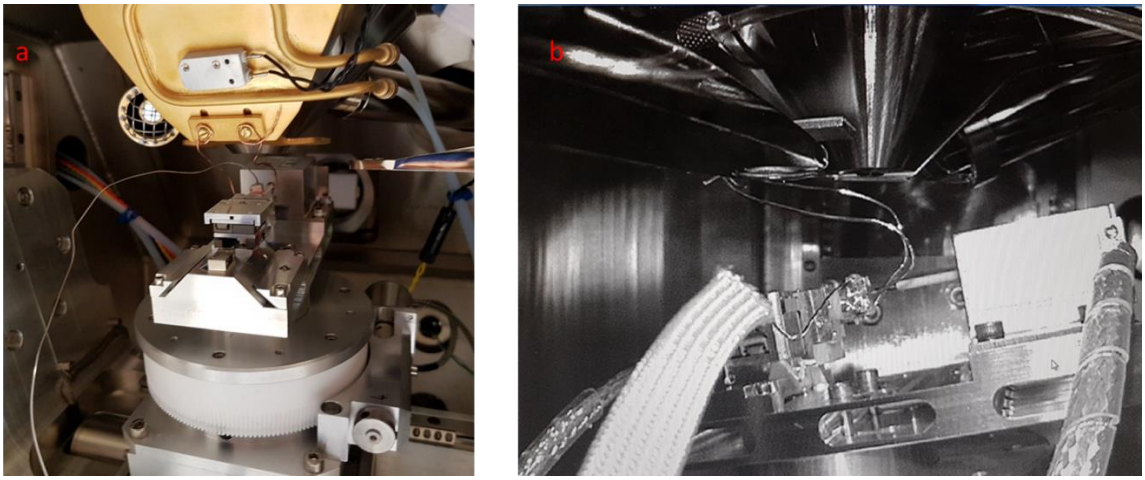

Figure 3.15: (a) and (b) Images of the PI85 set up inside the Tescan-SEM with the cryo-stage

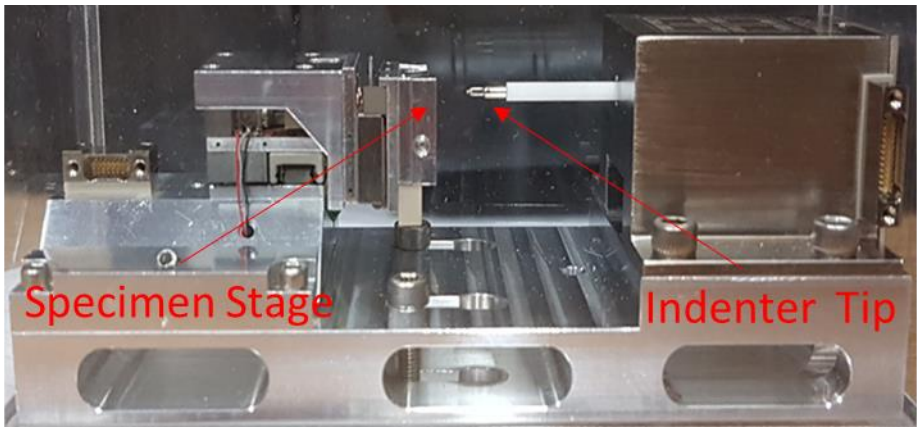

Figure 3.16: Hysitron PI85 indentation system without the cryo-stage

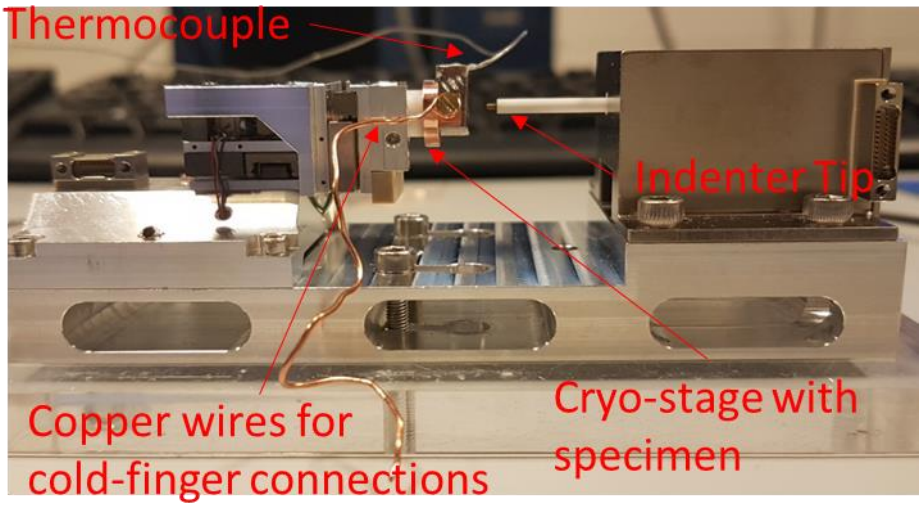

Figure 3.17: Hysitron PI85 indentation system with the cryo-stage

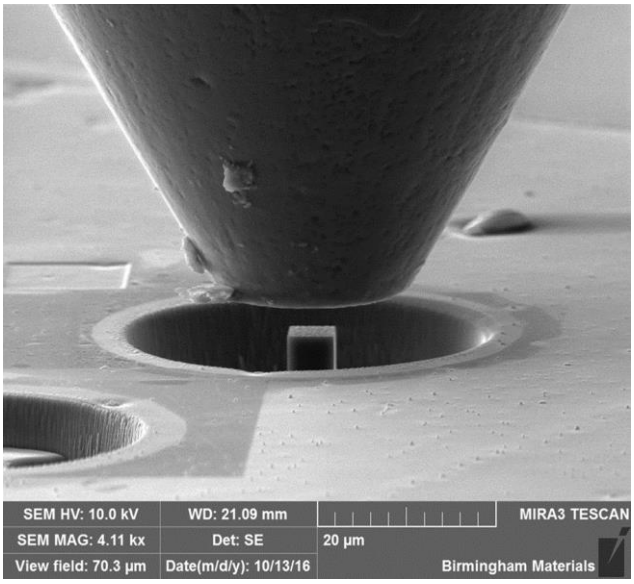

Figure 3.18: SEM image of the indenter and micro-pillar just before the compression

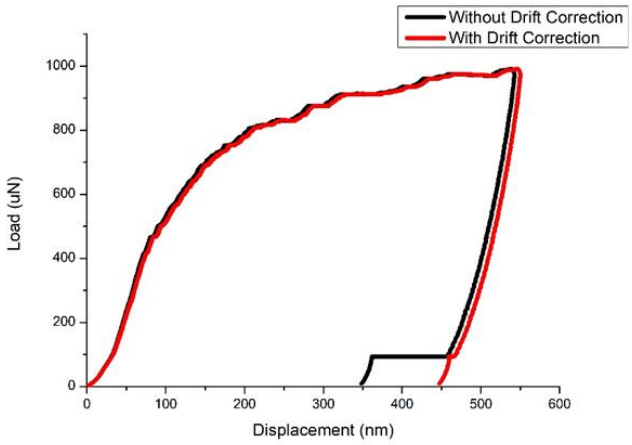

Figure 3.19: Load vs displacement curve with and without the drift correction

Table 3.2: Micro-pillar compression testing parameters

Loading Direction	**Test Temperature** (^{o}C)	**Test Mode**	**Drift Correction**	**Loading Rate** (μN/s)	**Peak Load** (μN)
[11$\bar{2}$1]	23, -28, -94	Load-controlled	Manual	200	1200,1600,2000
[0001]	23, -20, -90			1000	8000,12000,14000
[1$\bar{3}$20]	23, -28, -94			300	1800,2400,3000

3.5 Post-compression characterization

After compression, the next step was to perform post-mortem analysis on the deformed micro-pillars to establish the link between testing conditions and underlying deformation mechanisms.

For this purpose, Scanning Electron Microscopy (SEM) and Transmission Electron Microscopy (TEM) were used.

3.5.1 Scanning electron microscopy

In the first stage, scanning electron microscopy was performed on the deformed pillars using the Tescan MIRA3 SEM to observe any sort of deformation marks/traces on the face of a deformed pillar. These marks/traces were then related to the anticipated slip/twinning modes using slip trace analysis. A viewing angle of 30-40 degrees (specimen stage tilt) was used for the SEM imaging. An SEM image of a deformed micro-pillar with prominent slip trace/step is shown in Figure 3.20.

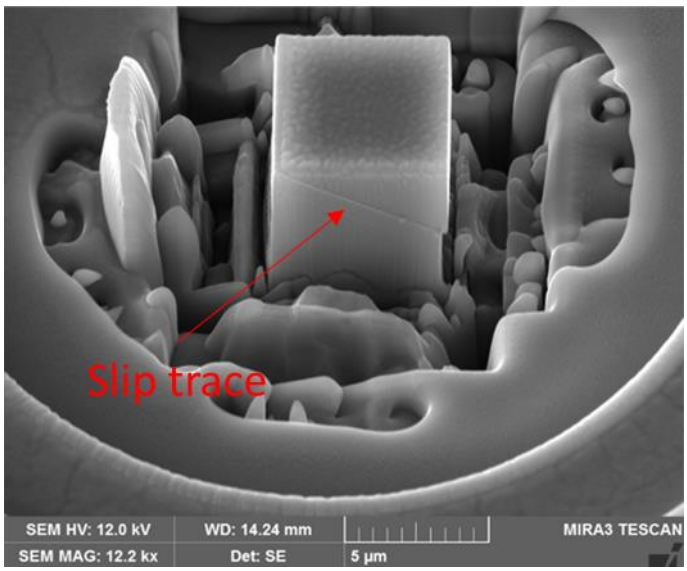

Figure 3.20: SEM image of a deformed micro-pillar with prominent slip traces

3.5.2 Transmission electron microscopy

In the later stage, an FEI Talos TEM operating at 200 kV was used to examine the dislocation substructure in the deformed pillars on. For dislocation analysis, 200-300 nm thin sections were prepared from the deformed micro-pillars using the FIB and a standard lift-out procedure was

employed. The procedure to make TEM foils is outlined at the end of this section. This microscopy technique was mainly used to observe the dislocations structure in the deformed micro-pillars and to identify the Burgers vector of the dominant dislocations in relation to a specific deformation mode. TEM images of initial microstructures of the specimens extracted from the three grains, used in this work to activate basal <a> slip, tension twinning and pyramidal <c+a> slip, are shown in Figures 3.21 (a-c). These figures show presence of small number of pre-existing dislocations highlighted in white ellipses. To identify the Burgers vector of the dislocations in the compressed pillars, dislocation image extinguishing method was used which is sometimes referred to as dislocation invisibility method. In this method, reflecting planes are determined for which a particular type of dislocation (with a characteristic Burgers vector) is invisible in TEM but becomes visible for some other reflecting planes. This condition of visibility/invisibility of the dislocations is achieved by setting up a two-beam condition in the diffraction imaging mode of the TEM. A diffraction image of a two-beam condition is shown in Figure 3.22 (c). A specific two-beam condition is achieved by tilting the specimen away from a standard diffraction zone axis along a specific Kikuchi line in such a way that the electron beam is diffracted from only one set of parallel planes and two beams only can be seen: one is the directl transmitted beam and other is the diffracted beam from the corresponding crystallographic plane. Based on the beam used to image the dislocations, bright field or dark field TEM images are obtained. An example of bright field and dark field images of the same set of dislocation for a distinct two-beam condition is shown in Figures 3.22 (a,b). In addition to dislocation analysis, Selected Area Diffraction Patterns (SADP) were used to identify the twins resulted during some of the compression experiments.

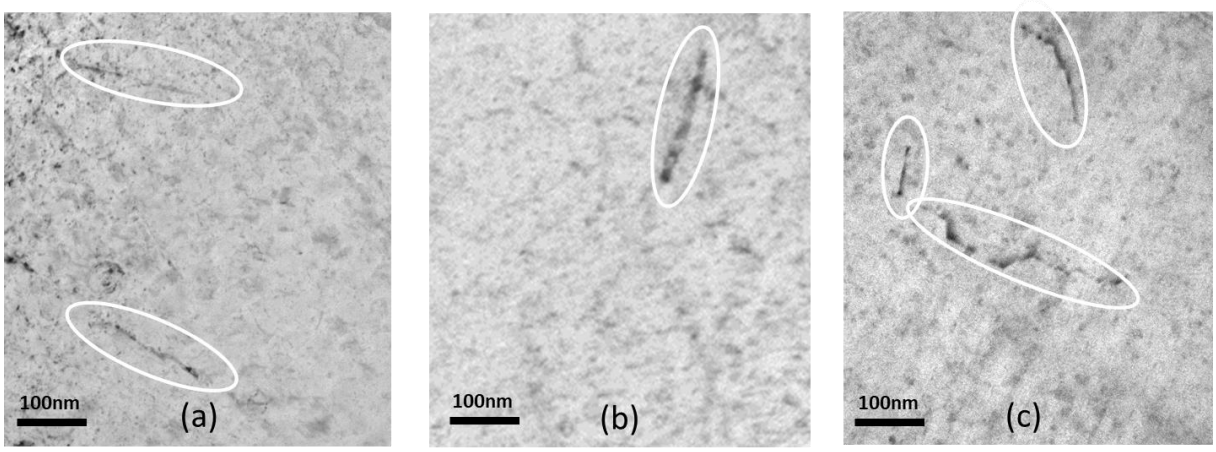

Figure 3.21: TEM images showing initial microstructure of the grains used in this work to make micro-pillars oriented for (a) basal<a> slip, (b) tension twinning and (c) pyramidal <c+a> slip. The white ellipses show presence of very small number of pre-existing dislocations prior to compression

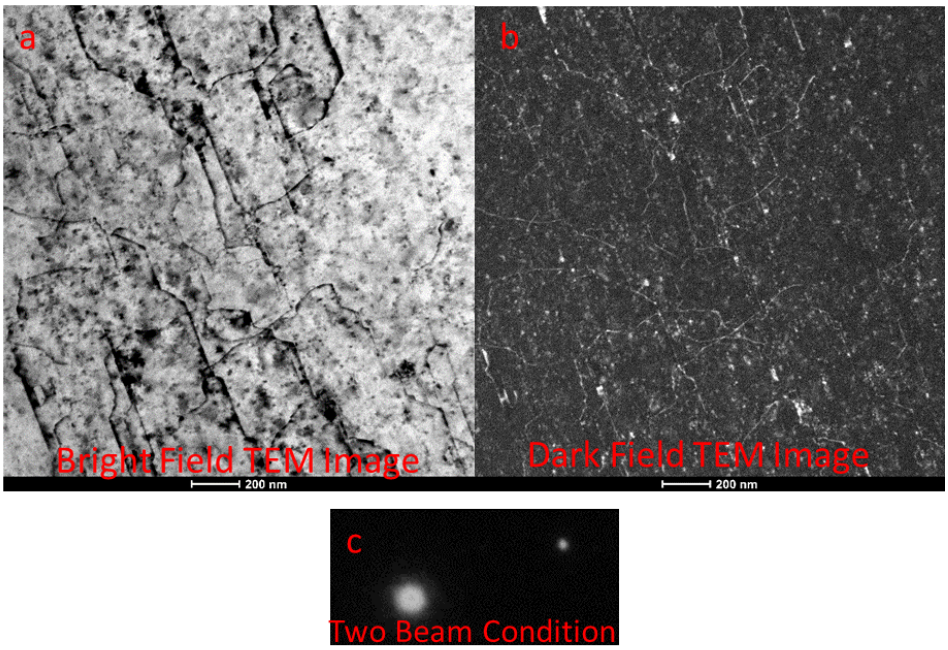

Figure 3.22: Two-beam bright field (BF) and dark field (DF) TEM images of a pure magnesium specimen containing non-basal dislocations taken along BD ~ $[\bar{2}110]$ *using 0002 reflection, (a) BF, (b) DF, and (c) diffraction set-up of the imaging condition*

3.5.3 Transmitted Kikuchi Diffraction

In addition to TEM dislocation analysis of the TEM foils, Transmission Kikuchi Diffraction (TKD) was also used on some of these foils to identify the presence of twins and their crystallographic relationship with the matrix. The set-up for the TKD experiment is the same as for that of a conventional EBSD experiment except for the tilt of the specimen with respect to the horizontal axis which is usually 20 degrees as compared to 70 degrees for a routine EBSD experiment. This 20-degree tilt allows the maximum chances of signal collection by the EBSD detector. In this research work, a special pre-tilt TKD holder was used for TKD experiments inside the Tescan SEM (Figure 3.23).

Figure 3.23: Two different EBSD pre-tilt holders

3.5.4 TEM lamella preparation

FEI Helios G4 PFIB CXe was used to extract thin TEM foils from the deformed micro-pillars. This FIB equipment uses Xenon (Xe) ions which gives a higher milling output as compared to the Ga FIB. The main steps to make a TEM foil are shown in Figures 3.24 (a-h) and are explained below:

1. 3 μm thick platinum (Pt) protective coatings were deposited on top, left and right sides of the pillars (Figures 3.24 a-b).

2. Trenches were milled in front and back sides of the pillar so that a ~2 μm thick specimen was left in a stand-alone position (Figures 3.24 c-d).

3. This 2 μm thick specimen was then attached to a mechanical manipulator needle using the platinum deposition layer and cut from the bottom of the specimen to separate from the rest of the bulk material (Figures 3.24 e-f).

4. The specimen was then attached to the copper grid and detached from the mechanical manipulator (Figure 3.24 g).

5. The 2 μm thick specimen was then milled to a thickness of 200-300 nm by performing successive milling steps on the top and bottom sides of the specimen (Figure 3.24 h).

6. Finally, a lower kV cleaning step was carried out on both sides of the specimen at higher tilting angles to reduce the ion beam damaged layer.

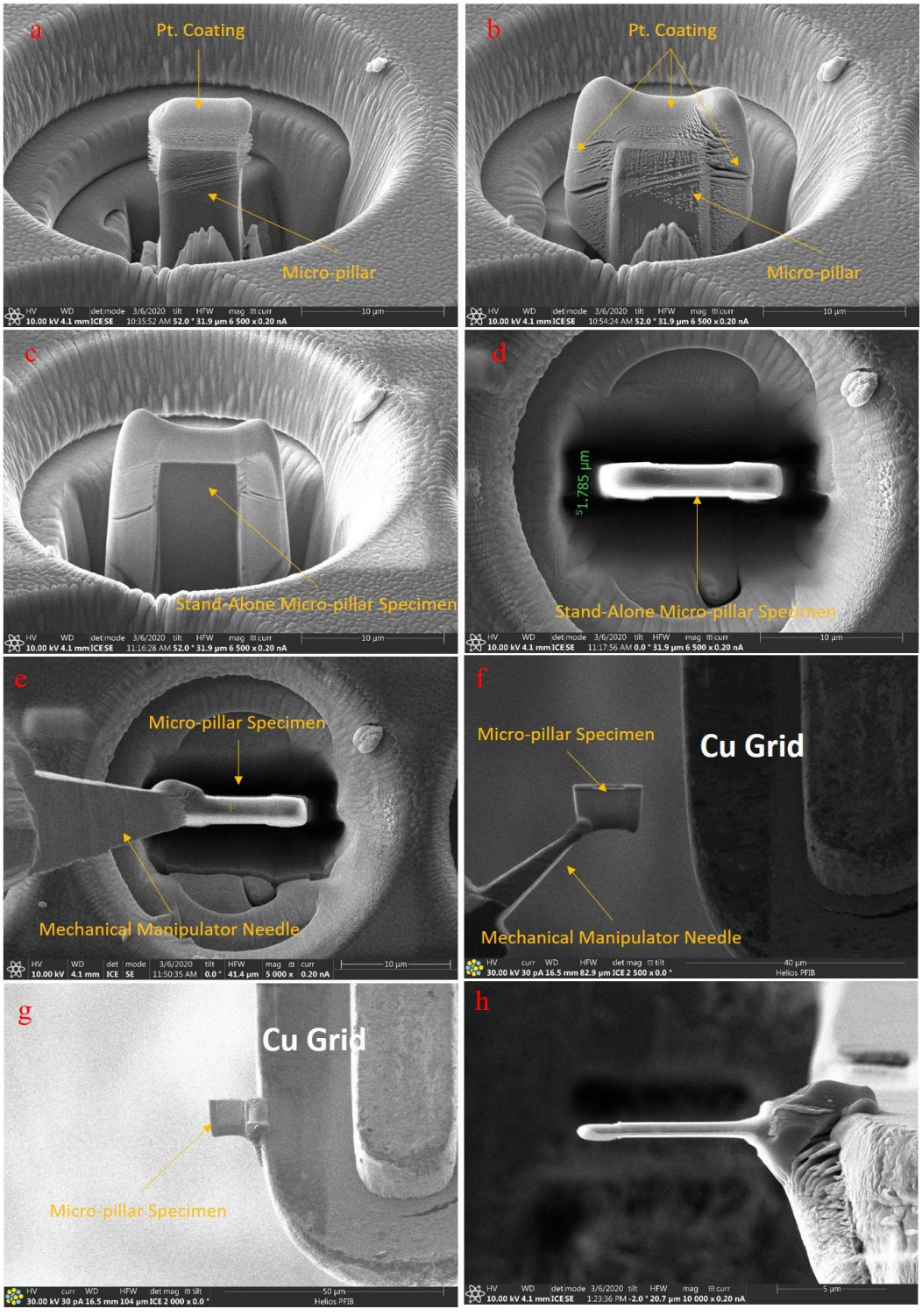

Figure 3.24: Steps involved in TEM specimen preparation using FIB (a,b) Protective platinum (Pt.) coating on top and both sides of the micro-pillar, (c-d) micro-pillar TEM specimen after coarse-milling from upper and lower sides to leave the specimen in stand-alone position, (e) specimen attached to the mechanical manipulator needle, (f) manipulator with the specimen next to the Copper (Cu) grid (g) specimen attached to the Cu grid after detachment from the manipulator needle and (h) final TEM specimen after thinning down to the required thickness

4 The temperature dependence of basal <a> slip

4.1 Results

In this set of experiments, micro-pillars with loading direction $[11\bar{2}1]$ were compressed to activate basal <a> slip at three different temperatures, 23°C, -28°C and -94°C with different peak loads but at the same loading rate. Three pillars were compressed at each test temperature. The compression tests were performed under load-controlled mode at a loading rate of 200 μN/s. This loading rate resulted in an initial strain rate of ~$5x10^{-3}$ s^{-1}, calculated from the displacement vs time data. By initial strain rate is meant from the point of the first contact, between the indenter-tip and the pillar top-surface, to the first significant change in the flow behaviour of the micro-pillars. For the $[11\bar{2}1]$ loading direction, the Schmid factor calculated for common deformation modes in magnesium are enlisted in Table 4.1 along with their CRSSs reported in the past literature. The Schmid factor of 0.42 for basal <a> slip together with its lowest CRSS of 0.5 MPa makes it favourable for the activation along $[11\bar{2}1]$ loading direction in preference to other deformation modes. That is why $[11\bar{2}1]$ oriented micro-pillars were selected to study the temperature dependence of basal <a> slip in magnesium single crystals.

Table 4.1: CRSS for different deformation modes reported in past literature along with Schmid factor for loading direction of $[11\bar{2}1]$

Deformation Mode	**CRSS** (MPa)	**Schmid Factor (m)**
		LD ~$[11\bar{2}1]$
Basal <a>	0.5 [20], [23], [24]	0.42

Prismatic <a> slip	39 [32]	0.33
Pyramidal <c+a>	40 [44]	0.43
Tension twinning	12 [158]	0.20

4.1.1 Stress-strain curves

4.1.1.1 Room temperature

The stress-strain curves of the $[11\bar{2}1]$ oriented micro-pillars compressed at 23°C are shown in Figure 4.1. This figure shows that these micro-pillars initially underwent elastic deformation until the first strain burst occurred in the stress-strain curves. From that stress level onwards, the plastic deformation proceeded by more strain bursts until a pre-defined peak load was reached, which was set up at the beginning of every compression experiment. These kinds of strain bursts are usually present whenever micro-pillar compression experiments are performed under load-control mode and the micro-pillars deform essentially by slip-dominated plasticity [115], [142], [159], [160]. Between two successive strain bursts, there is a small segment of elastic loading that results in a higher stress level for the succeeding strain burst than that of the previous strain burst [143], [161].

In this work, the stress at which the first strain burst appears is taken as the yield stress. The yield stress defines the stress required to initiate plastic deformation being shown by the transition in elastic to plastic deformation in the stress-strain curve which is the appearance of first strain burst here. Referring to the past literature, different authors have used different criteria to select yield stress In this regard, the stress at a fixed strain of somewhere between 0.2% and 5% has been taken as the yield stress considering that sufficient plastic deformation

had occurred by that strain level [94], [115], [159]. At room temperature, the average value of yield stress is measured to be 33.7 ± 2.6 MPa for the basal <a> slip. The corresponding CRSS is then calculated to be 14.1 ± 1.1 MPa, which is obtained by multiplying the yield stress by the Schmid factor of 0.42 for the basal <a> slip. The yield stress and CRSS values for individual micro-pillars are summarised in Table 4.2.

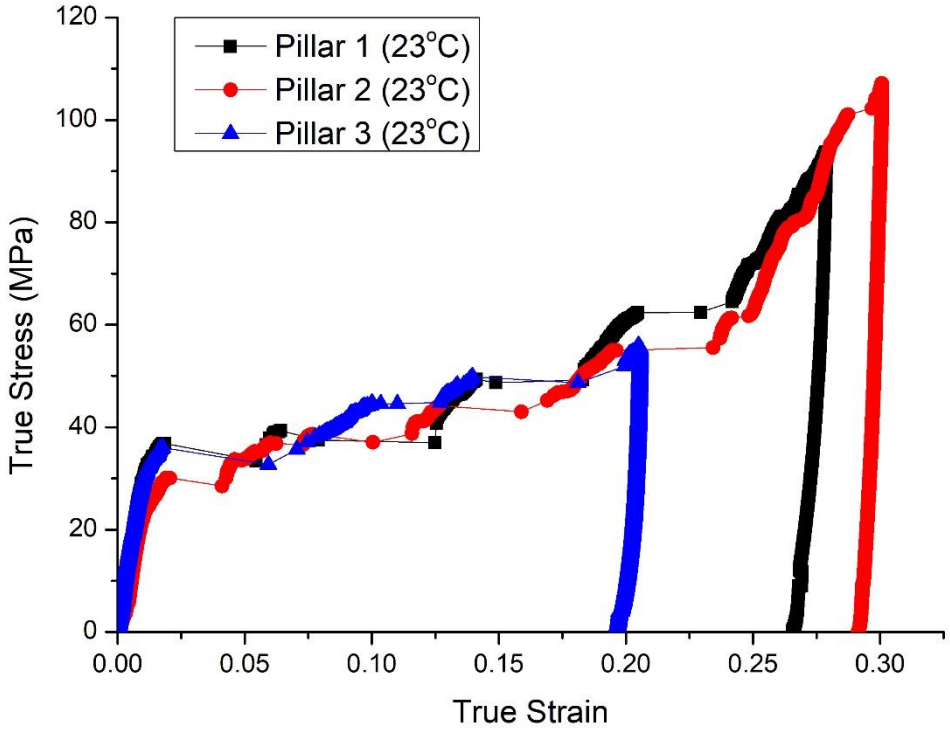

Figure 4.1:Stress-strain curves of $[11\bar{2}1]$ *oriented micro-pillars compressed at 23°C*

4.1.1.2 Cryogenic temperatures

The stress vs strain curves for the $[11\bar{2}1]$ oriented micro-pillars at -28°C and -94°C are presented in Figures 4.2 and 4.3 respectively. The appearance of these curves is quite similar to those for room temperature which suggested that the overall plastic deformation mechanism is the same at all three tested temperatures. Following the same approach for yield stress

measurement, the yield stress was taken as the stress at which the first strain burst occurred. The average yield stress values were measured to be 44.3±1.2 MPa and 55.7±4.0 MPa at -28°C and -94°C respectively. The corresponding CRSS values for basal <a> slip are calculated to be 18.6±0.5 MPa and 23.4±1.7 MPa at -28°C and -94°C respectively. For comparison purposes, the yield stress and CRSS values for all three test temperatures are given in Table 4.2. This table indicates that yield stress and CRSS values are the highest for -94°C and lowest for 23°C.

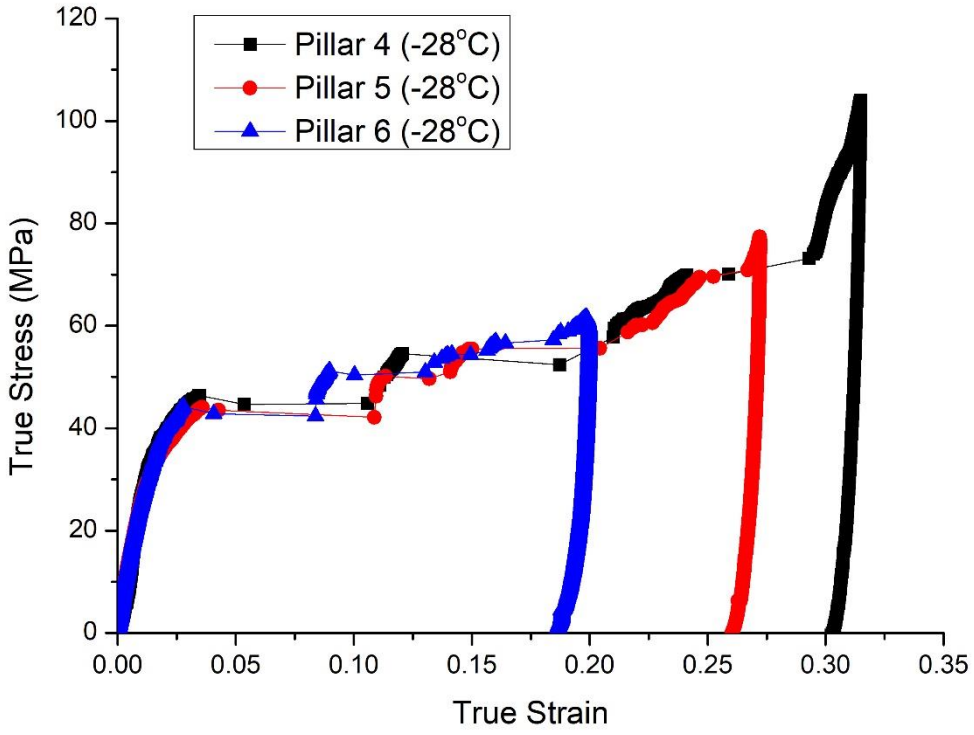

Figure 4.2: Stress-strain curves of $[11\bar{2}1]$ *oriented micro-pillars compressed at -28°C*

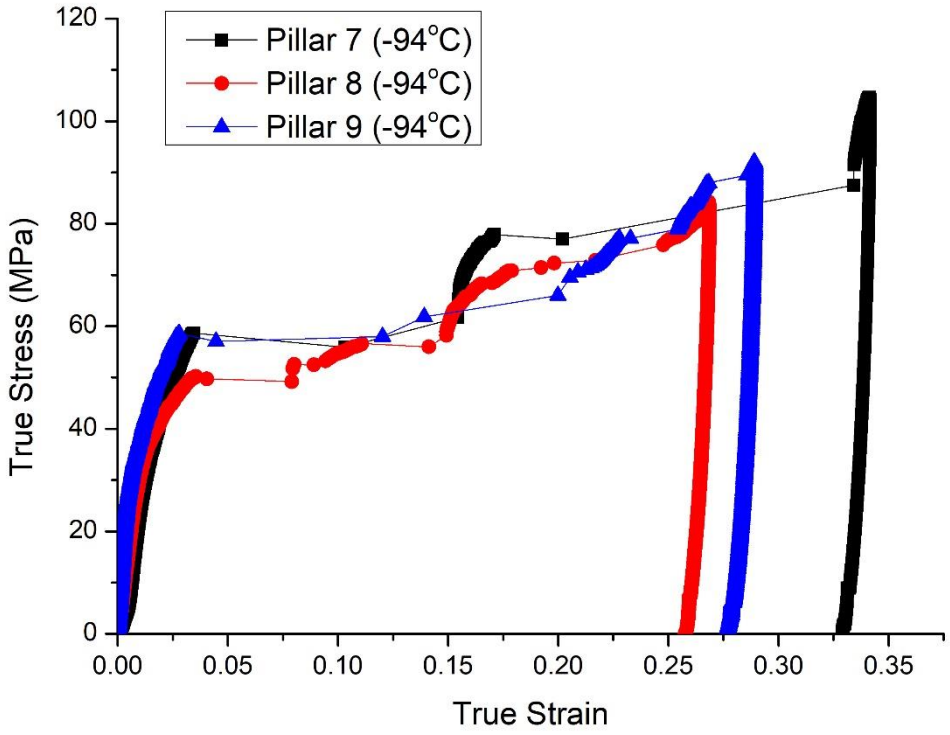

Figure 4.3: Stress-strain curves of $[11\bar{2}1]$ *oriented micro-pillars compressed at -94°C*

Table 4.2: Yield stress and CRSS values of basal <a> slip for $[11\bar{2}1]$ *oriented micro-pillars at different test temperatures. In column 3, the measured yield stress values of individual pillars are rounded up / down to the nearest 1 (MPa).*

Pillar Number	**Temperature** (°C)	**Yield Stress** (MPa)	**Average Yield Stress** (MPa)	**CRSS** (MPa)	**Average CRSS** (MPa)
1	23	36	33.7±2.6	15.1	14.1±1.1
2		30		12.6	
3		35		14.7	
4	-28	46	44.3±1.2	19.3	18.6±0.5

5		43		18.1	
6		44		18.5	
7		58		24.4	
8	-94	50	55.7±4.0	21.0	23.4±1.7
9		59		24.8	

4.1.2 Post-mortem SEM

To confirm the activated deformation mode in $[11\bar{2}1]$ oriented micro-pillars under different temperature conditions, the surfaces of the compressed micro-pillars were observed using scanning electron microscopy (SEM). These observations are outlined below:

4.1.2.1 Room temperature

The representative post-mortem SEM image of the Pillar 1 compressed at room temperature is shown in Figure 4.4. There are very prominent straight and sharp deformation bands/steps on the surface of the compressed micro-pillar. Since all these traces are parallel, making the same angle with the loading direction, this suggests a single slip. The formation of each deformation band is a consequence of a strain burst event appearing in the stress-strain curve. The origin of these slip traces was determined to be $\frac{1}{3}(0001)[11\bar{2}0]$ basal <a> slip using slip trace analysis and marked in the red dashed line in Figure 4.4 which was also to be the expected slip system. Thus, confirming that the $[11\bar{2}1]$ oriented micro-pillars were deformed by the activation of basal <a> slip at room temperature.

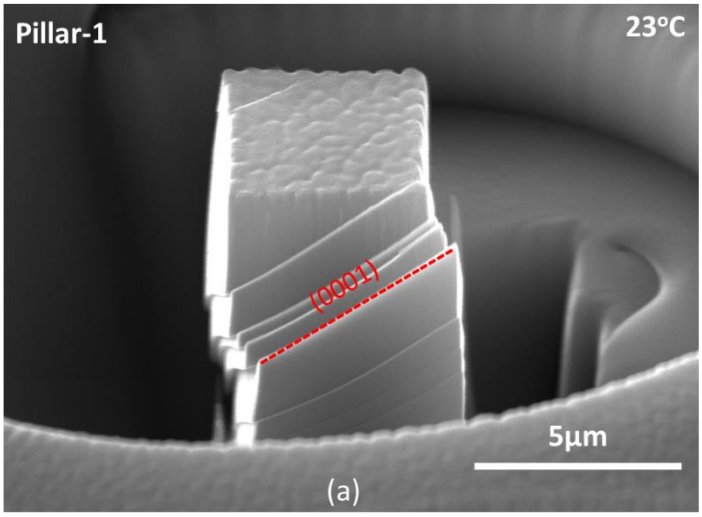

Figure 4.4: Representative post-mortem SEM image of Pillar 1 compressed at room temperature. The slip bands marked in red colour correspond to the trace of the basal plane. The images were taken with a stage tilt of 30 degrees

4.1.2.2 Cryogenic temperatures

The representative post-mortem SEM images of Pillar 4 compressed at -28°C and Pillar 9 compressed at -94°C are shown in Figures 4.5 and 4.6. Both the micro-pillars are showing deformation bands on their surfaces similar to those of room temperatures compressed micro-pillar (see Figure 4.4). The close resemblance of these deformation marks to the room temperature micro-pillar slip traces indicated that basal <a> slip is the main deformation mode at all the three test temperatures.

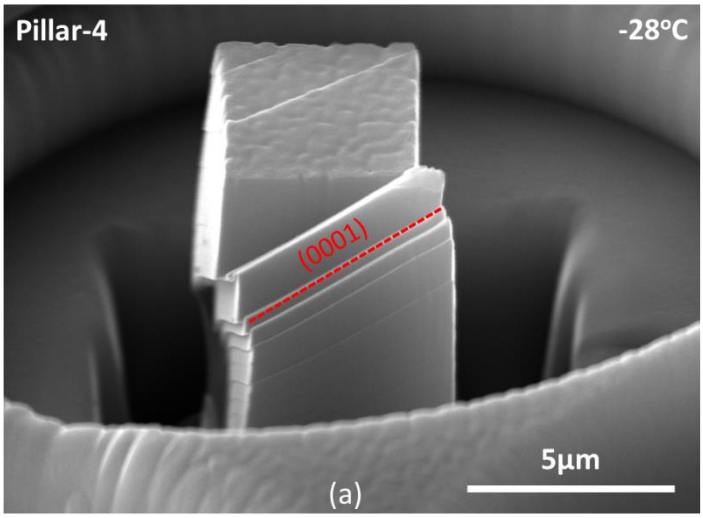

Figure 4.5: Representative post-mortem SEM image of Pillar 1 compressed at -28°C. The slip bands marked in red colour correspond to the trace of the basal plane. The images were taken with a stage tilt of 30 degrees

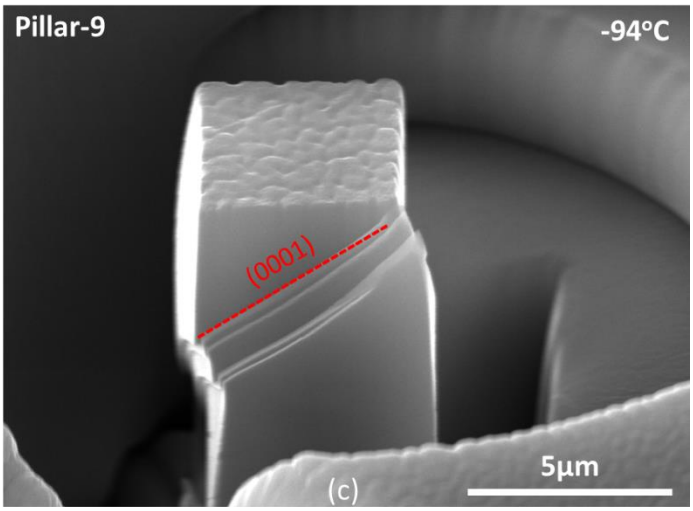

Figure 4.6: Representative post-mortem SEM image of Pillar 9 compressed at -94°C. The slip bands marked in red colour correspond to the trace of the basal plane. The images were taken with a stage tilt of 30

4.1.3 Post-mortem TEM

For further confirmation of the dominant slip system and identification of the Burgers vector of the activated dislocations at different test temperatures, post-mortem TEM was carried out. For this purpose, TEM specimens were extracted from the deformed micro-pillars parallel to the slip traces using FIB. The Burgers vector of the predominant gliding dislocations was determined by employing g.b invisibility criteria as explained in the previous chapter.

4.1.3.1 Room temperature

BF and DF TEM images of the specimen extracted from room temperature compressed Pillar 1 are presented in Figure 4.7. The electron beam direction was nearly parallel to [0001] and, BF and DF images were taken using g=$10\bar{1}0$, g=$01\bar{1}0$ and g=$1\bar{1}00$. There is a very high density of long and curved dislocations which are marked by yellow arrows inside the yellow box. This group of dislocations have the Burgers vector of $\frac{1}{3}[11\bar{2}0]$ as they are invisible when g=$1\bar{1}00$ (Figures 4.7 e-f) and visible when g=$10\bar{1}0$ (Figures 4.7 a-b) and g=$01\bar{1}0$ (Figures 4.7 c-d). Some of these basal <a> dislocations are schematically shown in Figure 4.7 (g) highlighted in yellow colour. Their dominant presence throughout the specimen suggested that $\frac{1}{3}[11\bar{2}0]$ type dislocations played the main role in the plastic deformation at room temperature of $[11\bar{2}1]$ oriented micro-pillars. In addition to this group of dislocations, a few other dislocations can also be seen, marked with blue arrows in Figures 4.7 (e-f) and schematically shown in Figure 4.7 (g) in blue colour, resulting from the activation of a secondary basal slip or non-basal (pyramidal <c+a>) slip systems during a later stage of plastic deformation. Moreover, some twins were also present in the TEM specimen and confirmed by TKD as shown in Figure 4.9. The presences of secondary dislocations and twins along with primary basal

dislocations support the argument for the mechanism of rapid rate of work hardening observed during the later stage of the compression tests (Figure 4.1).

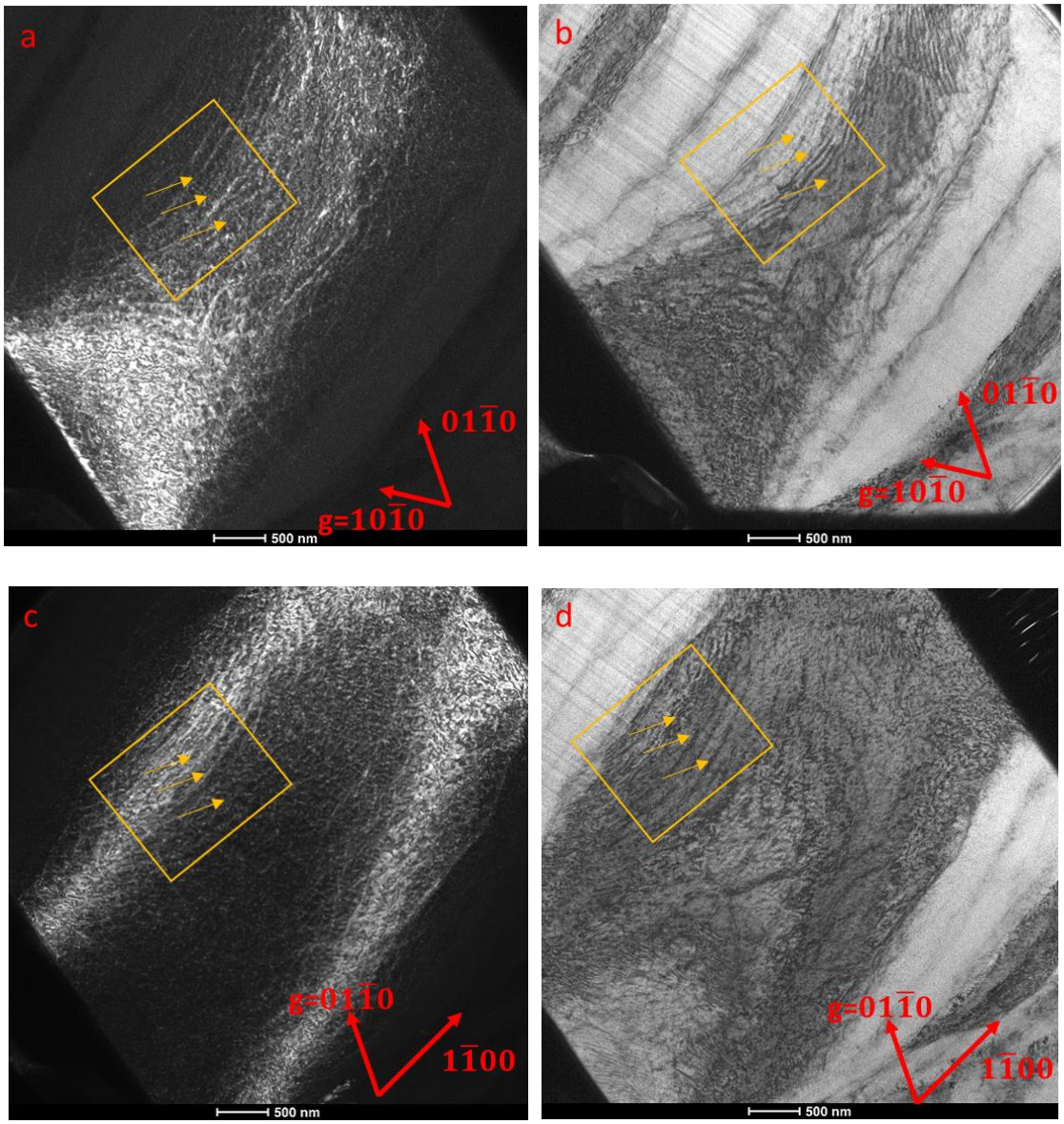

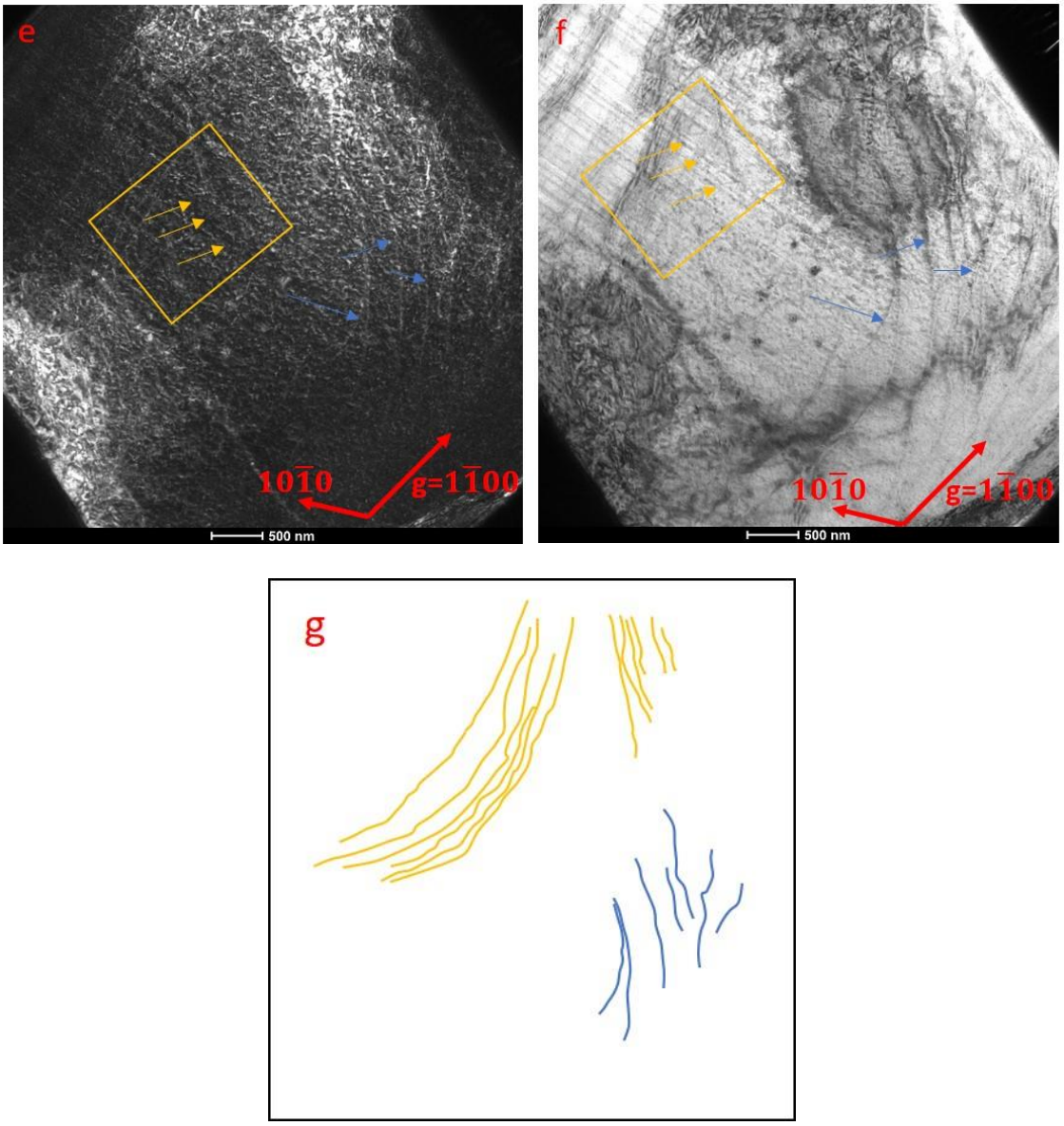

Figure 4.7: TEM images of the Pillar 1(with respect to the stress-strain curves) compressed at 23oC along BD ~ [0001]. (a-b) DF and BF images using $g=10\bar{1}0$*, (c-d) DF and BF images using* $g=01\bar{1}0$ *and (e-f) DF and BF images using* $g=1\bar{1}00$*.(g) A schematic illustration of the dislocations observed in the TEM specimen of Pillar 1. The yellow coloured dislocations in (g) represent the primary basal dislocations with* $\frac{1}{3}(0001)[11\bar{2}0]$ *Burgers vector which are present in the yellow outlined boxes in (a-d) and absent in (e-f). The blue colored dislocations in (g) correspond to the secondary dislocations highlighted with blue arrows in (e-f).*

4.1.3.2 Cryogenic temperatures

For low-temperature post-mortem TEM analysis, TEM specimen was extracted from Pillar 9 compressed at -94°C as representative of both cryogenic test temperatures compressed micro-pillars. The BF and DF TEM images were taken along the [0001] electron beam direction using $10\bar{1}0$, $01\bar{1}0$, and $1\bar{1}00$ reflections (Figure 4.8). Similar to the room temperature TEM specimen, there is an abundance of long and curved dislocations throughout the specimen with a Burgers vector of $\frac{1}{3}[11\bar{2}0]$ as they are out of contrast for $1\bar{1}00$ (Figures 4.8 e-f) and in contrast for $10\bar{1}0$ (Figures 4.8 a-b) and $01\bar{1}0$ (Figures 4.8 c-d) reflections. These basal <a> dislocations are schematically shown in Figure 4.8 (g). A few other secondary dislocations and twins were also observed. These had probably contributed towards the rapid work hardening similarly to the case of room temperature compressed micro-pillars.

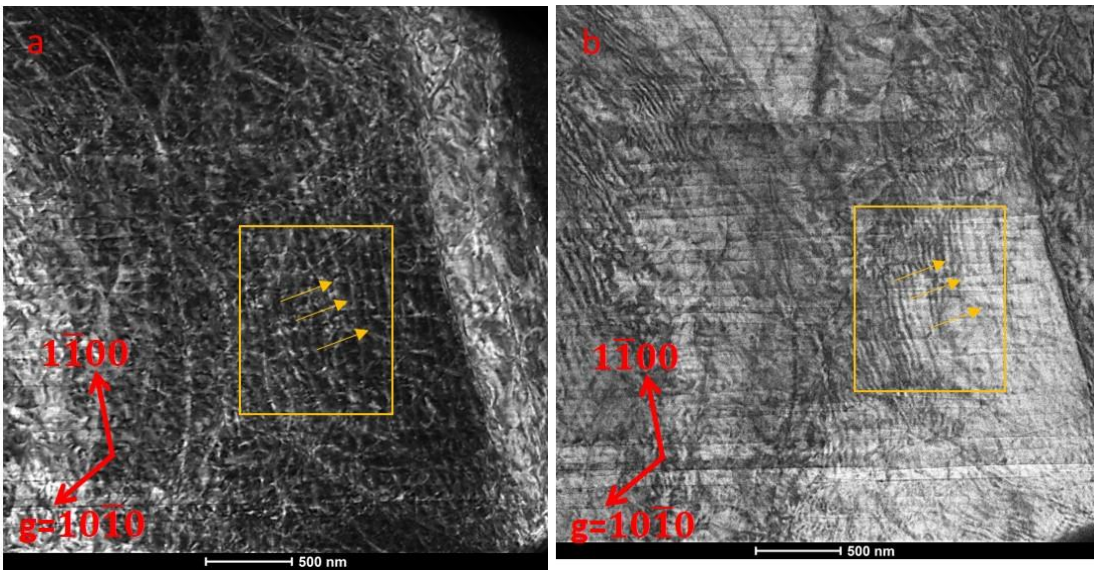

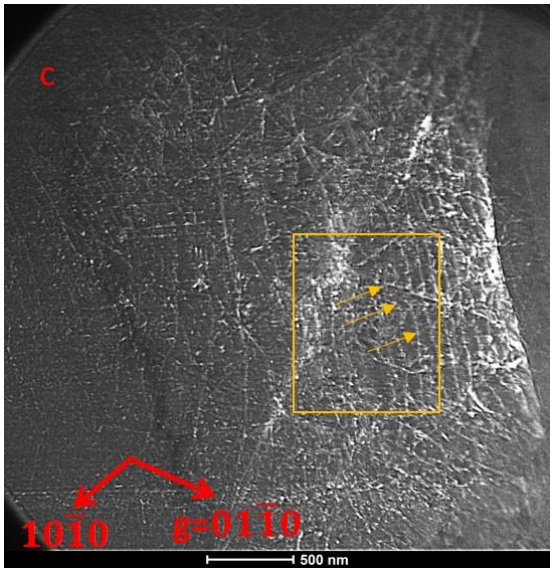
c
$10\bar{1}0$
$g=01\bar{1}0$
500 nm

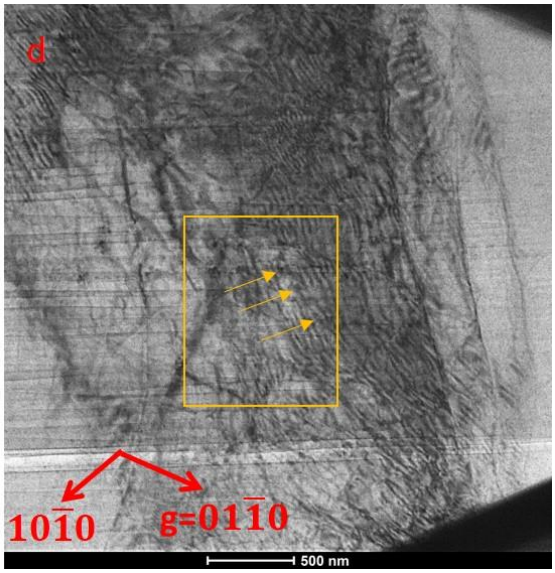
d
$10\bar{1}0$
$g=01\bar{1}0$
500 nm

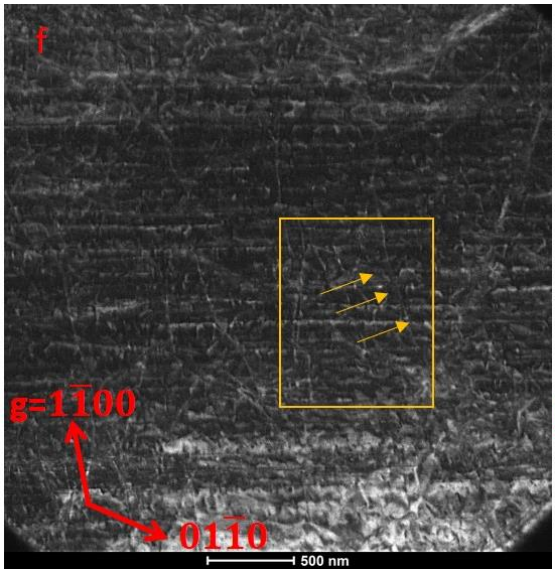
f
$g=1\bar{1}00$
$01\bar{1}0$
500 nm

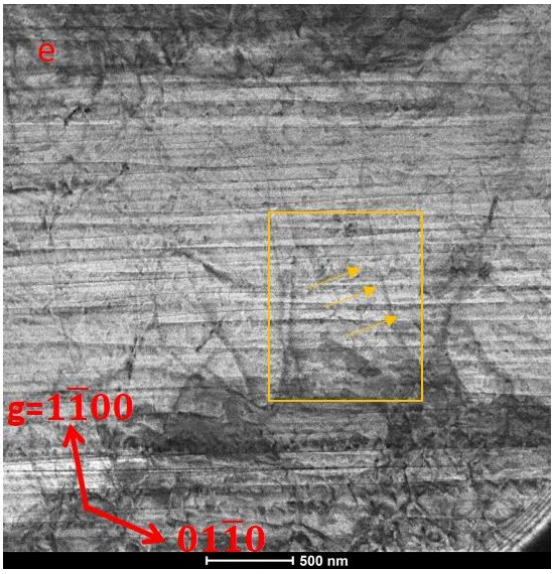
e
$g=1\bar{1}00$
$01\bar{1}0$
500 nm

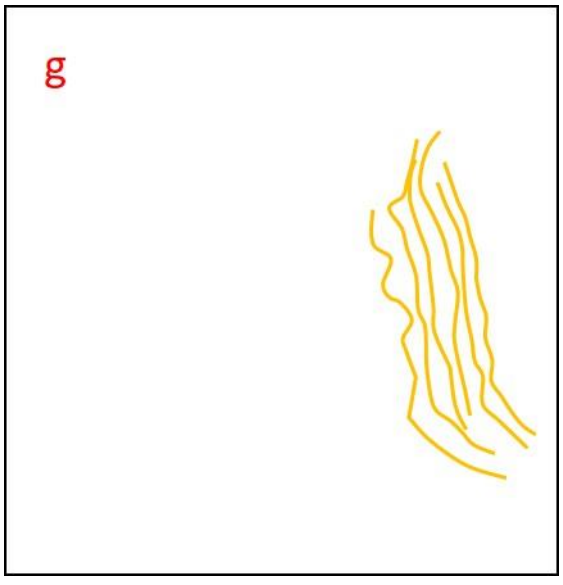
g

Figure 4.8: TEM images of Pillar 3 compressed at -94°C along BD ~ [0001]. (a-b) DF and BF images using g=$10\bar{1}0$*, (c-d) DF and BF images using g=*$1\bar{1}00$ *and (e-f) DF and BF images using g=*$01\bar{1}0$*. (g) A schematic illustration of the dislocations observed in the TEM specimen of Pillar 3. The yellow coloured dislocations in (g) represents the primary basal dislocations with* $\frac{1}{3}$*(0001)[*$11\bar{2}0$*] burgers vector which are present in the yellow outlined boxes in (a-d) and absent in (e-f).*

4.1.4 TKD mapping

To confirm the presence of twins, TKD was performed on the same TEM foil that was used for room temperature dislocation analysis (Pillar 1 compressed at 23°C). The TKD map of the specimen is shown in Figure 4.9 which confirms the presence of twins in the sample. The blue coloured area of the phase map (Figure 4.9 b) corresponds to the presence of twins. Their volume, however, is quite small compared with the slip dominated volume of the sample. These twins are believed to originate during the later stage of the micro-pillar compression tests.

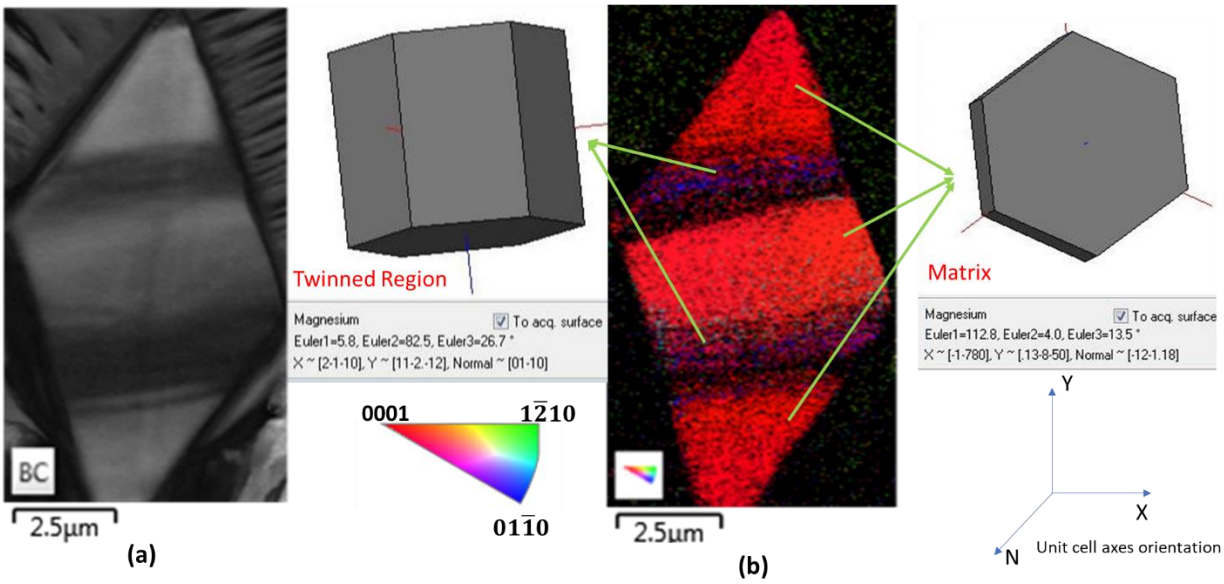

Figure 4.9: TKD map for room temperature compressed micro-pillar TEM specimen, (a) band contrast, and (b) phase map. The red and blue regions in (b) show the matrix (parent grain) and twinned regions respectively.

4.2 Discussion

In the first group of experiments, square-shaped micro-pillars with [11$\bar{2}$1] loading direction were compressed at 23°C, -28°C and -94°C to study the effect of temperature on the activation of basal <a> slip. The post-mortem SEM and TEM observations confirmed the activation of (0001) [11$\bar{2}$0] basal <a> slip as main deformation mode for this loading direction not only at room temperature but at cryogenic test temperatures as well. A high density of long and curved dislocations of Burgers vector $\frac{1}{3}$[11$\bar{2}$0] were present in both the TEM specimens of room temperature tested micro-pillar and -94°C compressed micro-pillar, indicating their dominant role in the plastic deformation of this set of micro-pillars suggesting that the dislocation structure for [11$\bar{2}$1] oriented micro-pillars did not change with the change in testing temperature. The dislocation structure in the TEM foils was so dense, due to very high level of

strains (> 20%) in the compressed pillars from which the TEM foils were extracted, that it was not possible to measure dislocation density quantitatively. The stress-strain behaviour of the micro-pillars suggests that the overall plastic deformation mechanism remains the same throughout the test temperature range except for the yield stress and the corresponding CRSS values. The representative stress-strain curve for each test temperatures is shown in Figure 4.10. The variation in CRSS values is plotted in Figure 4.11 as a function of the test temperature. This plot shows that the CRSS for basal <a> slip increases with decrease in temperature between 23°C to -94°C.

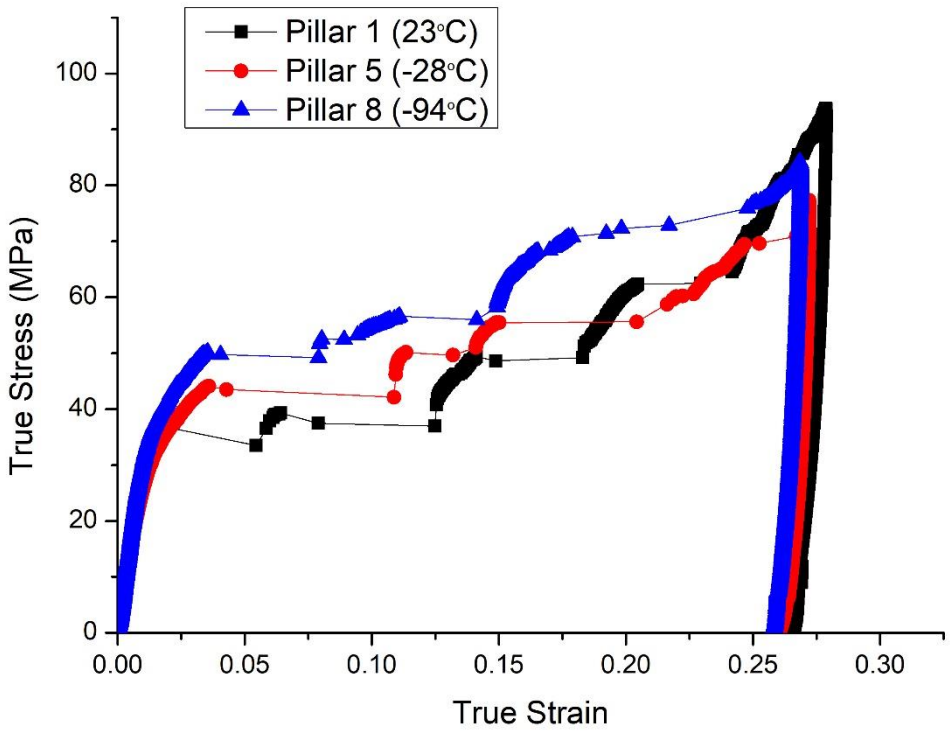

Figure 4.10: Representative stress-strain curves of $[11\bar{2}1]$ *oriented micro-pillars at three test temperatures*

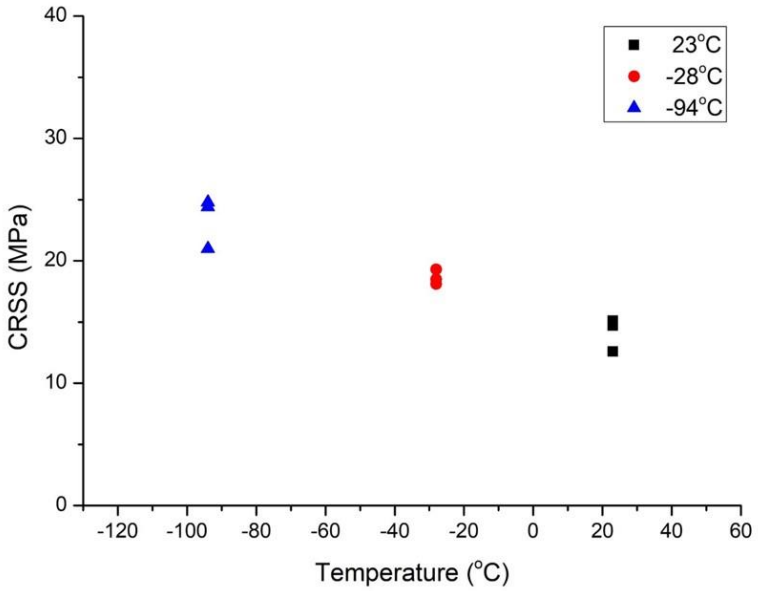

Figure 4.11: Variation in CRSS as a function of test temperature for $[11\bar{2}1]$ *oriented micro-pillars*

In theory, CRSS refers to a stress level needed to activate the softest dislocation source for a particular deformation mode in a single crystal test specimen. In a single crystal micro-pillar compression experiment, the plastic deformation initiates preferably by the motion of pre-existing dislocations on their respective glide plane after overcoming the Peierls lattice friction. These gliding dislocations then sweep through the whole pillar to reach the edge of the pillar and ultimately escape from the pillar surface, leaving the pillar in a dislocation-starved condition. Further deformation then proceeds by nucleation of new dislocations and their subsequent motion.

In the context of the present study, both the key processes of glide of pre-existing dislocations and dislocations nucleation for the initiation of basal <a> slip are reported to be thermally activated in magnesium.[162]–[164]. Molecular Dynamics and Meta-Dynamics simulation

studies of basal <a> slip in magnesium suggested that a <a> type dislocation require less activation free energy to nucleate on the basal plane at a higher temperature than that of lower temperature resulting into the need of smaller value of shear stress for the nucleation of <a> dislocation on the basal plane at higher temperatures and hence the smaller CRSS [162], [163]. Further on this, Uranagase and Matsumoto [162] estimated shear stresses of 978 MPa, 931 MPa and 863 MPa required to generate a <a> dislocation loop on the basal plane in magnesium single crystal at -173°C, 27°C and 227°C respectively in their computer simulation study of magnesium single crystal. Similar to the effect of temperature on nucleation of basal <a> dislocations, the mobility of <a> dislocations on the basal plane also got affected by the test temperature to some extent as suggested by the Molecular Dynamics (MD) and Molecular Statics (MS) simulation work of Groh et al. [164]. They observed higher mobility of <a> dislocations on the basal plane at higher temperature due to the more thermal energy being available to the moving dislocation at higher temperature resulting into the smaller CRSS at higher temperatures. Thus, decrease in activation free energy for the nucleation of <a> dislocations and decrease in the lattice friction to the gliding <a> dislocation, on the basal plane, with the increase in temperature, are likely the reasons of smaller CRSS for basal <a> slip in magnesium at higher temperature observed in this study.

A similar increasing trend in basal <a> slip CRSS values in magnesium with the decrease in temperature between room temperature and below has been reported in the past literature. Bhattacharya [28] and Conrad et al. [23] reported an increase in CRSS from 0.4 MPa to 0.7 MPa and 0.52 MPa to 1.22 MPa, respectively, for this slip system between room temperature and -195°C. Although the trend is the same, however, our CRSS values of 14.1 MPa and 23.4 MPa are relatively higher in the test temperature range from 23°C to -94°C as shown in Figure 4.12. The reason for this more pronounced increase in CRSS value in the much

narrow temperature range can be explained based on the test sample size. In this work, micron-sized pillars were used compared with millimetre-sized samples in the work of Bhattacharya [28] and Conrad et al. [23] which resulted in the limited dislocation sources inside our micro-pillars. Hence, a higher resolved shear stress was needed to activate the scarce dislocation sources not only at room temperature but also at lower test temperatures. Similar trends in yield stress with the decrease in temperature has also been reported for micro-pillar compression experiments of Ta, Mo, W, Nb and Fe for single slip favoured orientations [140], [141], [144], [165].

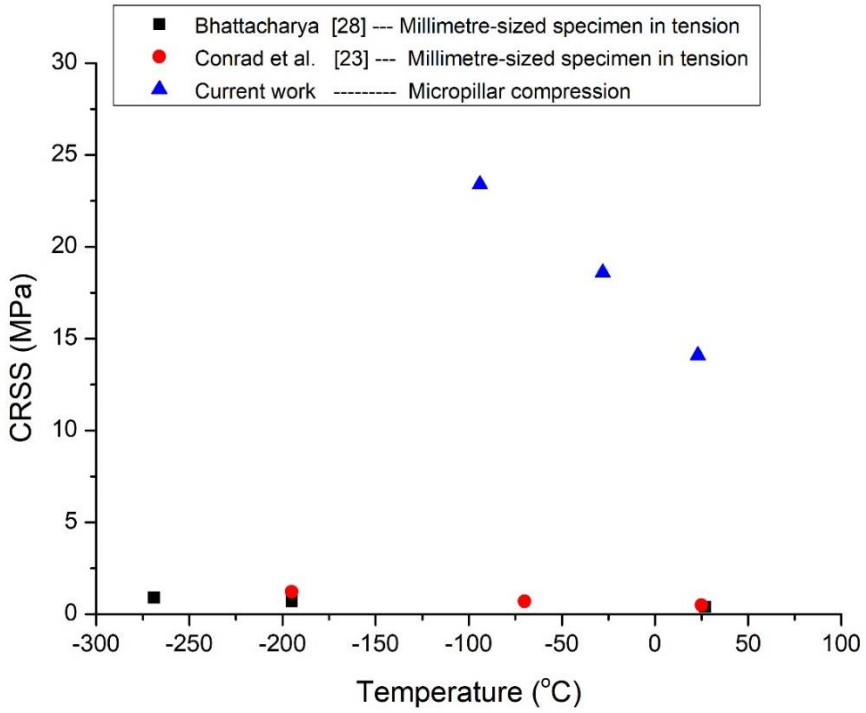

Figure 4.12: Plot of CRSS for basal <a> slip as a function of test temperature to compare current work with the literature. The CRSS values from literature are reported by Bhattacharya [28] and Conrad et al. [23]

In recent years, the activation of basal <a> slip in magnesium and its alloys has been studied by some authors via micro-pillars compression to investigate the effects of micro-pillar size, and concentration of alloying elements on the CRSS of basal <a> slip [15], [17], [136]. In these studies, the CRSS for basal <a> slip in pure magnesium single crystal micro-pillars are found to be in the range between 5 MPa to 50 MPa depending upon the pillar size [15], [16], [18], [19]. In this context, our room temperature measured CRSS for basal <a> slip (14.1 MPa) is comparable to those of Kim [15] who reported CRSS a value of 15 MPa at room temperature for 5 μm sized micro-pillars.

Another important feature observed during our micro-pillars experiments is the presence of multiple strain bursts in the stress-strain curves at all test temperatures which is not an uncommon feature during slip dominated micro-pillars compression studies. This kind of stress-strain behaviour could be explained by the widely accepted mechanism of "dislocation-starvation", first introduced by Greer et al. [114]. They suggested that upon yielding, plastic deformation is first initiated via the motion of pre-existing primary basal dislocations which are then likely to leave the micro-pillar surface without interaction/multiplication. Consequently, the whole volume of the micro-pillar is likely to become 'dislocation starved'. Further plastic deformation is then suggested to be accomplished by the nucleation of new primary basal dislocations and their subsequent motion resulting in a strain burst event in the stress-strain curve. This process of nucleation of new mobile dislocations, as a result of dislocation starvation, needs a higher resolved shear stress for every successive strain burst event.

4.3 Summary

The effect of test temperature on the activation of basal <a> slip in pure magnesium single crystals has been studied by in-situ micro-pillar compression at 23°C, -28°C and -94°C using a

specially designed cryo-stage. The yield stress and CRSS show a significant increasing trend with the decrease in temperature from 14.1 MPa to 23.4 MPa between 23°C and -94°C, respectively. This increase in CRSS is attributed to the thermal activation to overcome the Peierls lattice friction for the dislocation motion and the activation free energy for the nucleation of <a> dislocation on the basal plane in magnesium single crystals. The test temperature between 23°C and -94°C does not have significant effect on the dislocation structure for basal <a> slip in magnesium single crystal at the micron length scale.

5 Temperature dependence of tension twinning

5.1 Results

In the second group of experiments, uniaxial compression of $[1\bar{3}20]$ oriented micro-pillars were performed at room temperature, -28°C and -94°C to study the temperature dependence of tension twinning in magnesium single crystals. The micro-pillar compression was performed in load-controlled mode with a loading rate of 300 μN/s corresponding to an initial strain rate of ~2 x 10^{-3} s^{-1}. Four micro-pillars were tested at each test temperature with different peak loads in the range from 1800 μN to 3000 μN giving strains between 1.8% and 9.4%. The Schmid factor for various deformation modes for $[1\bar{3}20]$ loading are given in Table 5.1 along with the CRSS values as reported in the past literature. According to the highest Schmid factor criterion, prismatic <a> slip might be expected here with a Schmid factor of 0.49. But this is not the case whenever magnesium single crystals are compressed with similar loading directions. The reason is the different CRSSs of these competing deformation modes. Table 5.1 shows that the CRSS for basal slip is by far the lowest, but the Schmid factor for basal slip is zero for this loading direction, resulting in minimal chances of its activation. On the other hand, prismatic <a> slip has the highest Schmid factor of 0.49, but also the highest CRSS at the same time. In this context, tension twinning would be expected to be activated first, considering its Schmid factor and CRSS. This is the reason why micro-pillars with a loading direction parallel to $[1\bar{3}20]$ are selected to study the temperature dependence of tension twinning in magnesium single crystals.

Table 5.1: CRSS of different deformation modes reported in the past literature, along with the Schmid factor for a loading direction of [1$\bar{3}$20] with respect to the matrix and a loading direction of [$\bar{4}$ 8 $\bar{4}$ 15] with respect to the twinned region.

Deformation Mode	**CRSS** (MPa)	**Schmid Factor (m)**	
		LD ~ [1 $\bar{3}$ 2 0] (matrix)	**LD ~ [$\bar{4}$ 8 $\bar{4}$ 15]** (Twin)
Basal <a>	0.5 [20], [23], [24]	0.00	0.40
Prismatic <a> slip	39 [32]	0.49	0.10
Pyramidal <c+a>	40 [44]	0.43	0.45
Tension twinning	12 [158]	0.43	0.41

5.1.1 Stress-strain curves

5.1.1.1 Room temperature

Figure 5.1 shows stress-strain curves obtained by compression of [1$\bar{3}$20] oriented micro-pillars at room temperature. There are two significant features in these curves: one, the strain bursts, with limiting rate of work hardening (Pillars 2,3 and 4), and other, a rapid rate of work hardening at a later stage of the deformation (Pillars 2 and 3). The strain bursts were observed to appear around ~1.5 % strain. There is a large strain burst of average size (span) ~4.6% strain in the curves of Pillars 2, 3 and 4. The presence of strain bursts in the stress-strain curve is likely

due to the twinning events because of rapid twin propagation and growth once the twin nucleation has taken place.

For these stress-strain curves, the onset of plasticity or the yield stress is taken as the flow stress for 0.2% offset strain. These yield stress values are used to compute CRSS for the twin nucleation / activation based on the observations of smaller strain bursts (microplasticity) in the stress-strain curves appearing even before 0.2% strain which (smaller strain bursts-microplasticity) is believed to be the result of twin nucleation. These smaller strain bursts are very evident in case of Pillars 2,3 and 4 (Figure 5.1), however less evident in case of Pillar 1 due to the scale used here to plot the stress-strain curves. The average yield point and CRSS for activation of twinning were then measured which are 64.2 ± 17.0 MPa and 27.6 ± 7.3 MPa respectively for the $[1\bar{3}20]$ oriented micro-pillars. The yield stress and the CRSS values for the twin nucleation for all the four pillars are summarised in Table 5.2. There is a large scatter in the yield stress values due to the stochastic nature of twinning because yielding here is believed to be caused by twin nucleation which in turns depends upon stochastic conditions of local stress / strain concentration [19], [87], [135], [166].

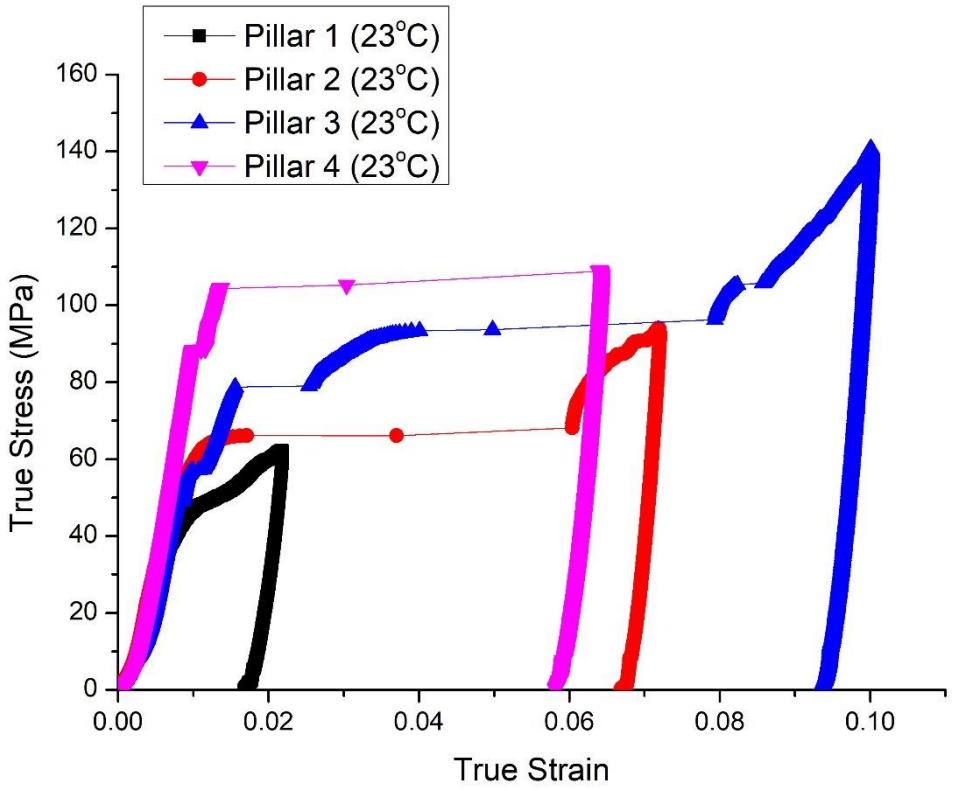

Figure 5.1: Stress-strain curves of [1$\bar{3}$20] oriented micro-pillars compressed at 23°C. Presence of strain bursts in the stress-strain curves are indicative of occurrence of twinning here.

5.1.1.2 Cryogenic temperatures

For the cryogenic mechanical behaviour, four micro-pillars with the same loading direction were compressed at -28°C and four micro-pillars at -94°C. The stress-strain curves for both cryogenic test temperatures are shown in Figures 5.2 and 5.3. The features of the cryogenic stress-strain curves are similar to those for room temperature as strain bursts and the late rapid work hardening can be seen in both the figures. However, the strain bursts are not as large as at room temperature. The average size (span/length) of the strain burst is ~0.8% strain for the -28°C micro-pillars and ~0.9% strain for -94°C tested micro-pillars (c.f. ~4.6% at RT). For

comparison purposes, the stress-strain curve with the largest strain burst for each test temperature is plotted in Figure 5.4.

Following the same approach to measuring yield stress as for the room temperature set of experiments, the average yield stress was measured to be 62.5 ± 22.2 MPa and 65.2 ± 10.0 MPa at -28°C and -94°C respectively and the corresponding CRSSs for twin nucleation / activation were calculated to be 26.9 ± 10.0 MPa and 28.1 ± 4.3 MPa, respectively. These values of the critical stresses at cryogenic temperatures are comparable to the room temperature measured critical stresses for $[1\bar{3}20]$ oriented micro-pillars for the activation of tension twinning. The values of yield stress are plotted as a function of temperature in Figure 5.5 whereas the yield stress and CRSS values for the individual micro-pillars are mentioned in Table 5.2.

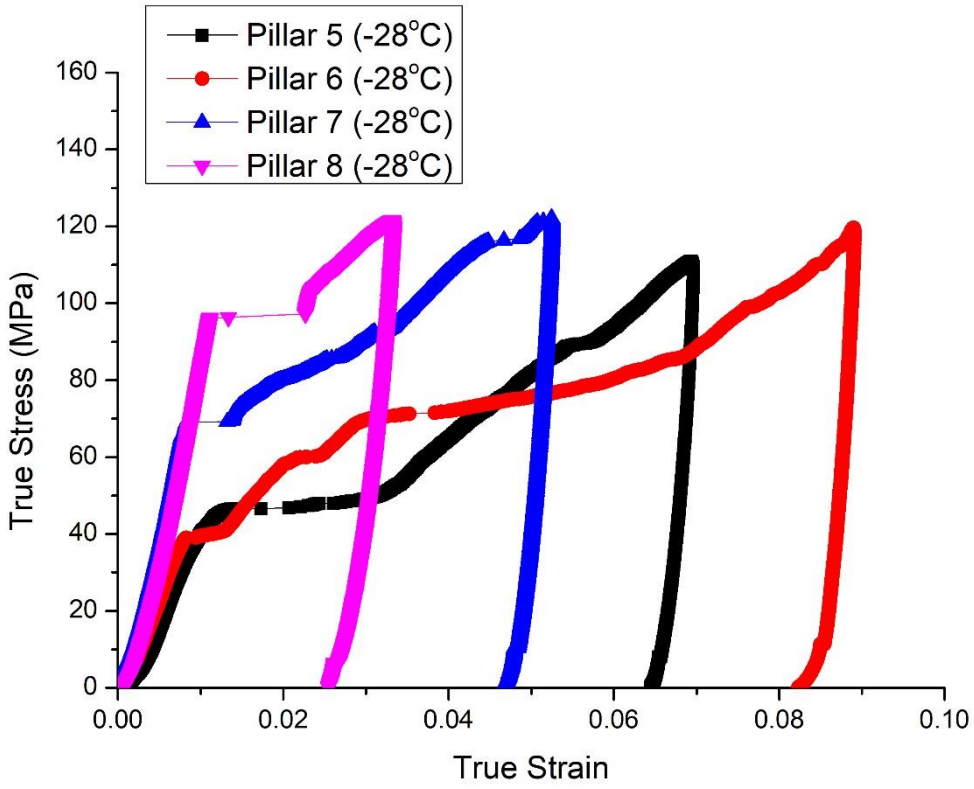

Figure 5.2: Stress-strain curves of [1$\bar{3}$20] oriented micro-pillars compressed at -28°C. Presence of strain bursts in the stress-strain curves are indicative of occurrence of twinning at -28°C.

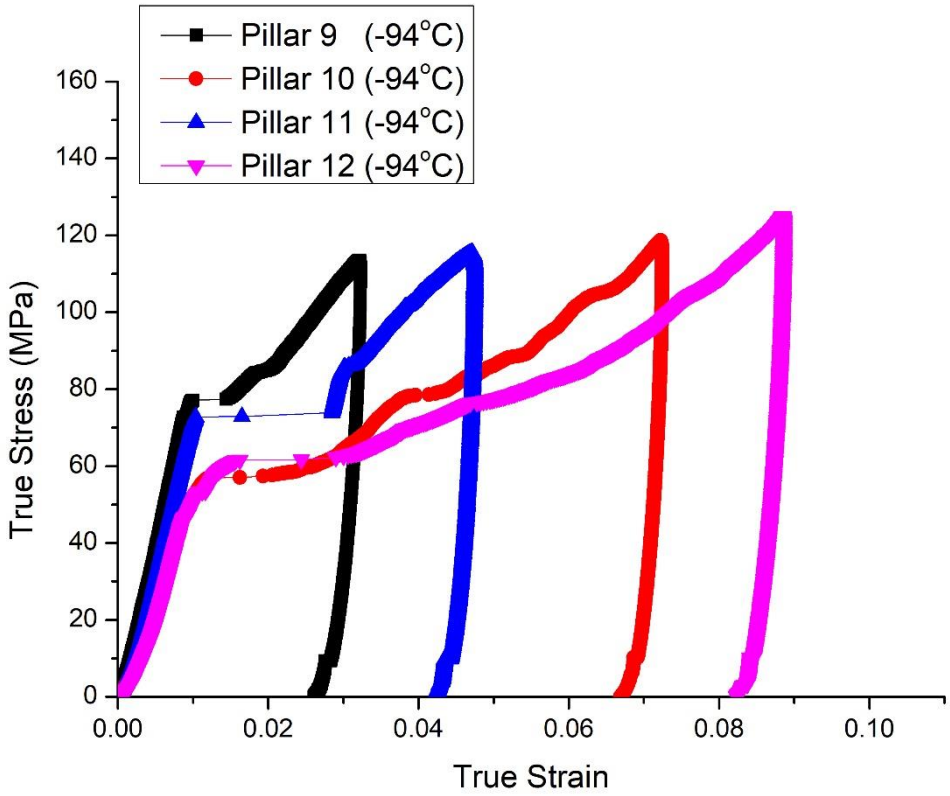

Figure 5.3: Stress-strain curves of [$1\bar{3}20$] oriented micro-pillars compressed at -94°C. Presence of strain bursts in the stress-strain curves are indicative of occurrence of twinning at -94°C.

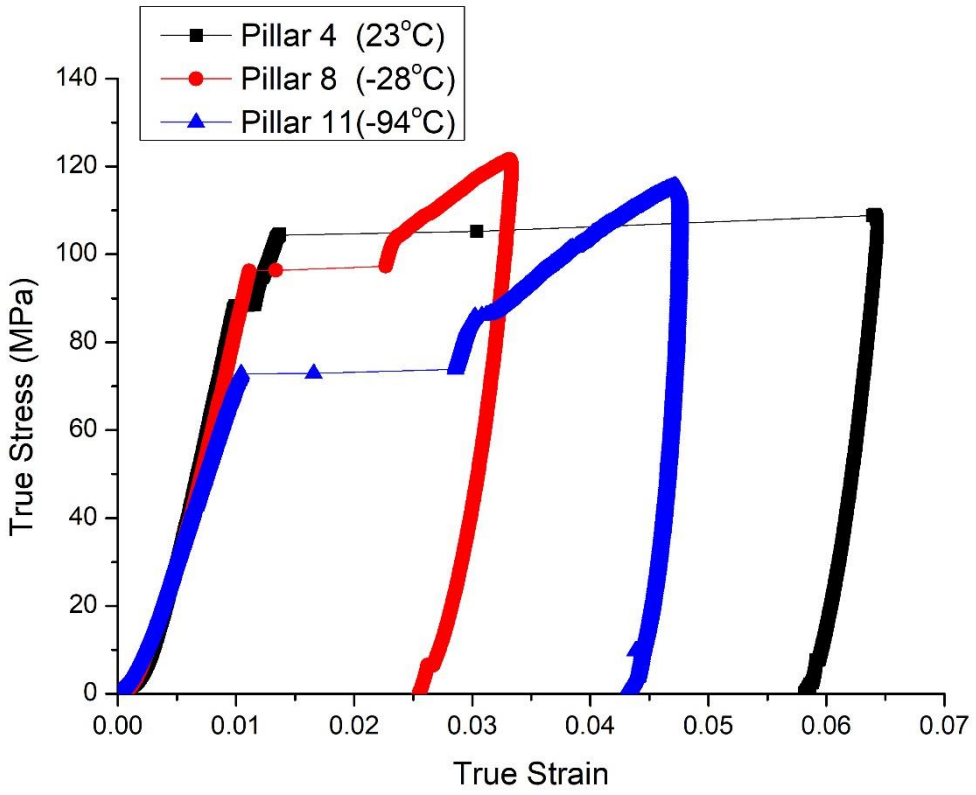

Figure 5.4: Stress-strain curves of [$1\bar{3}20$] oriented micro-pillars; one curve at each test temperature having the largest strain burst

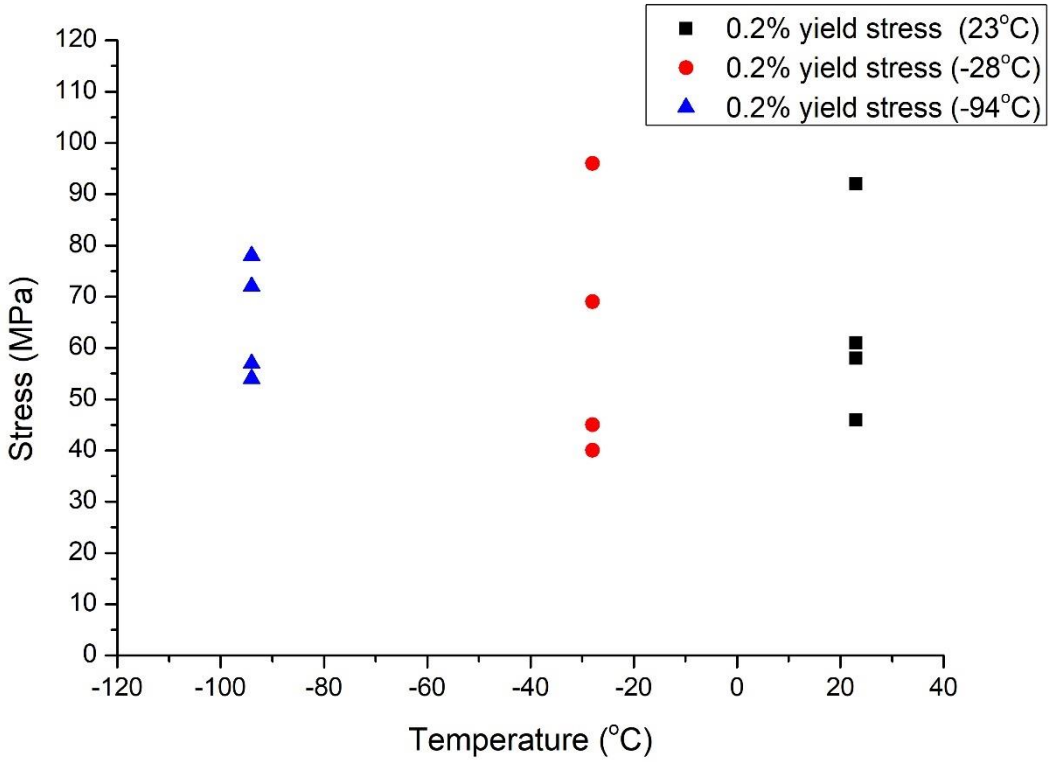

Figure 5.5: Variation in yield stress for tension twinning as a function of temperature for all [1$\bar{3}$20] oriented micro-pillars

Table 5.2: Yield stress and CRSS for twin nucleation for [1$\bar{3}$20] oriented micro-pillars at different test temperatures. The yield stress is taken as flow stress at 0.2% strain and is measured from the respective stress-strain curves.

Pillar Number	**Temperature** (°C)	**Yield Stress** (MPa)	**Average Yield Stress** (MPa)	**CRSS for Twin Nucleation** (MPa)	**Average CRSS for Twin Nucleation** (MPa)
1	23	46.0	64.2 ± 17.0	19.9	27.6 ± 7.3
2		61.0		26.2	
3		58.0		24.9	
4		92.0		39.6	
5	-28	45.0	62.5 ± 22.2	19.4	26.9 ± 10.0
6		40.0		17.2	
7		69.0		29.7	
8		96.0		41.3	
9	-94	78.0	65.2 ± 10.0	33.5	28.1 ± 4.3
10		57.0		24.5	
11		72.0		31.0	
12		54.0		23.2	

5.1.2 Post-mortem SEM

5.1.2.1 Room temperature

Representative post-mortem SEM images of room temperature compressed [$\mathbf{1\bar{3}20}$] micro-pillars are shown in Figures 5.6 and 5.7. Figure 5.6 is the SEM image of Pillar 1 having ~1.8% strain and Figure 5.7 of Pillar 4 which got ~5.9% strain. There were two prominent features observed on the surfaces of these micro-pillars: twin bands, highlighted in red colour on the surfaces of Pillars 1 and 4 (Figures 5.6 and 5.7), and the sharp straight steps / lines spreading across the pillar faces in case of Pillar 4 only (Figures 5.7 a-d), which are believed to be the slip-steps because of their appearance, and labelled in yellow colour. Presence of twin bands on both the pillar surfaces indicates that twinning is activated in both micro-pillars.

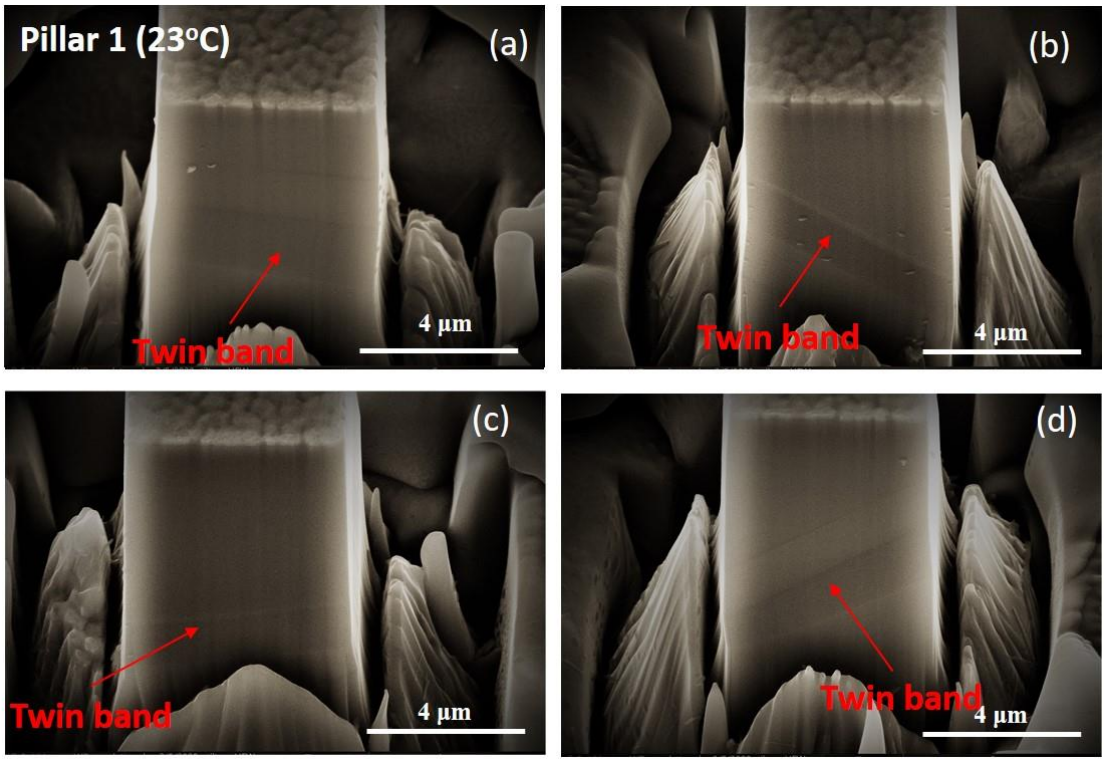

Figure 5.6: (a-d) Post-mortem SEM images of four faces of room temperature compressed Pillar 1 with ~ 1.8 % strain. Twin bands are apparent on all four faces (a-d) and highlighted in red colour. Images were taken with stage tilt of 30 degrees.

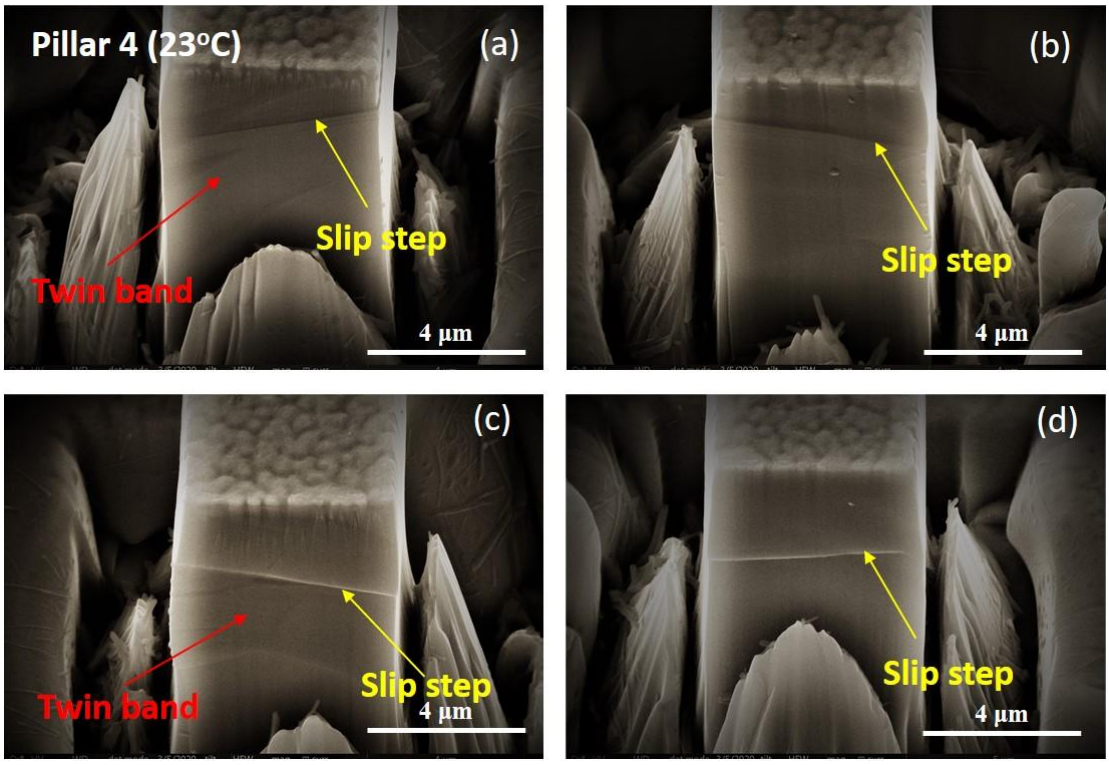

Figure 5.7: (a-d) Post-mortem SEM images of four faces of room temperature compressed Pillar 4 with ~ 5.9 % strain. Twin band is apparent in (a, c) and highlighted in red colour whereas slip-step are present on all four sides (a-d) and highlighted in yellow colour. All the images were taken with stage tilt of 30 degrees.

The presence of a slip-step on the surface of Pillar 4 and not in Pillar 1 suggests that the slip activity would have been taken place after exceeding at least 1.9 % strain as Pillar 1 got 1.9 % strain and there is no slip step observed on its surface indicating that twinning was activated first on the onset of plasticity and then the slip activity followed. Similar twin bands and slip-steps were also observed in other room temperature compressed micro-pillars. Collectively, these observations indicate that micro-pillars with a $[1\bar{3}20]$ loading direction deform initially by twinning, followed by the slip activity.

5.1.2.2 Cryogenic temperatures

Post-mortem SEM images of Pillar 5 and Pillar 8, representative of the -28°C test temperature, are shown in Figures 5.8 and 5.9. Pillar 5 and Pillar 8 were given strains of ~6.5% and ~2.4% respectively. The micro-pillars' surfaces are showing similar features like room temperature compressed micro-pillars including twin bands and slip-steps. The twin bands can be seen in both the pillars as marked in red colour in Figures 5.8 and 5.9 whereas slip-steps is present in case of Pillar 5 only, highlighted in yellow colour. The appearance of slip step in Pillar 5 suggests that, at -28°C, the micro-pillars deformed initially by the activation of twinning and once the micro-pillars attained a critical amount of strain then slip steps started to appear on the pillar surface which was the case for RT compressed micro-pillars as well.

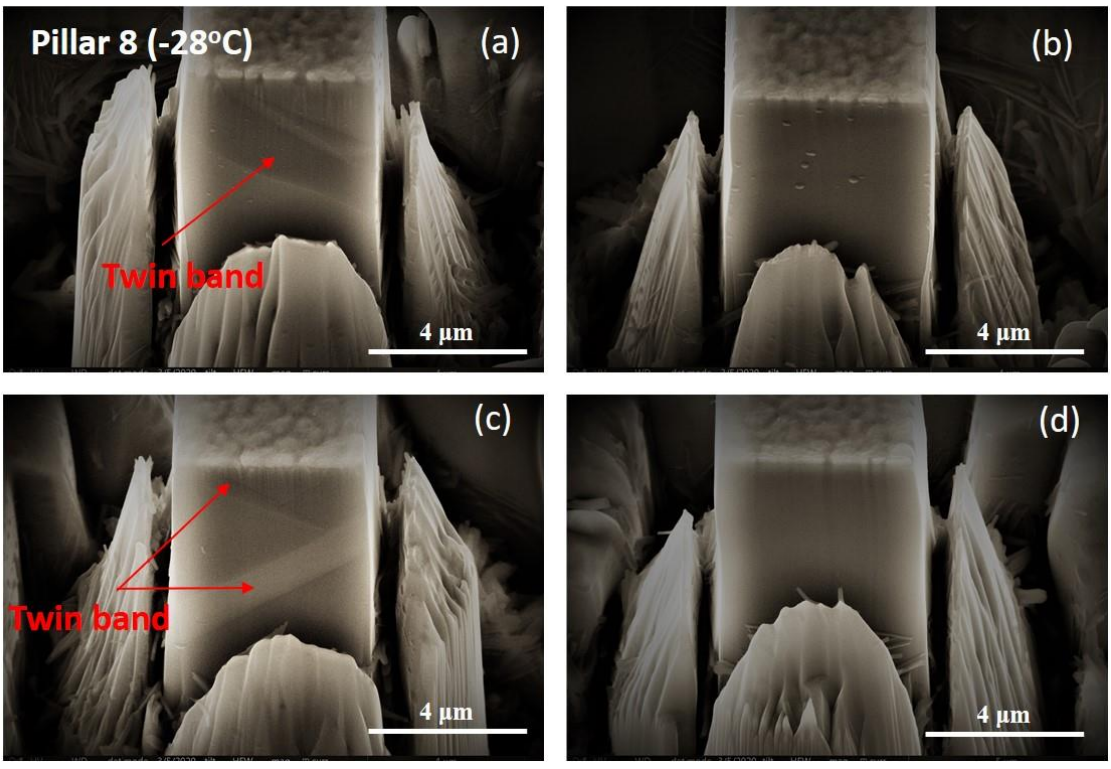

Figure 5.8: (a-d) Post-mortem SEM images of four faces of -28°C compressed Pillar 8 with ~ 2.4 % strain. Twin bands are apparent in (a, c) and highlighted in red colour. Images were taken with stage tilt of 30 degrees.

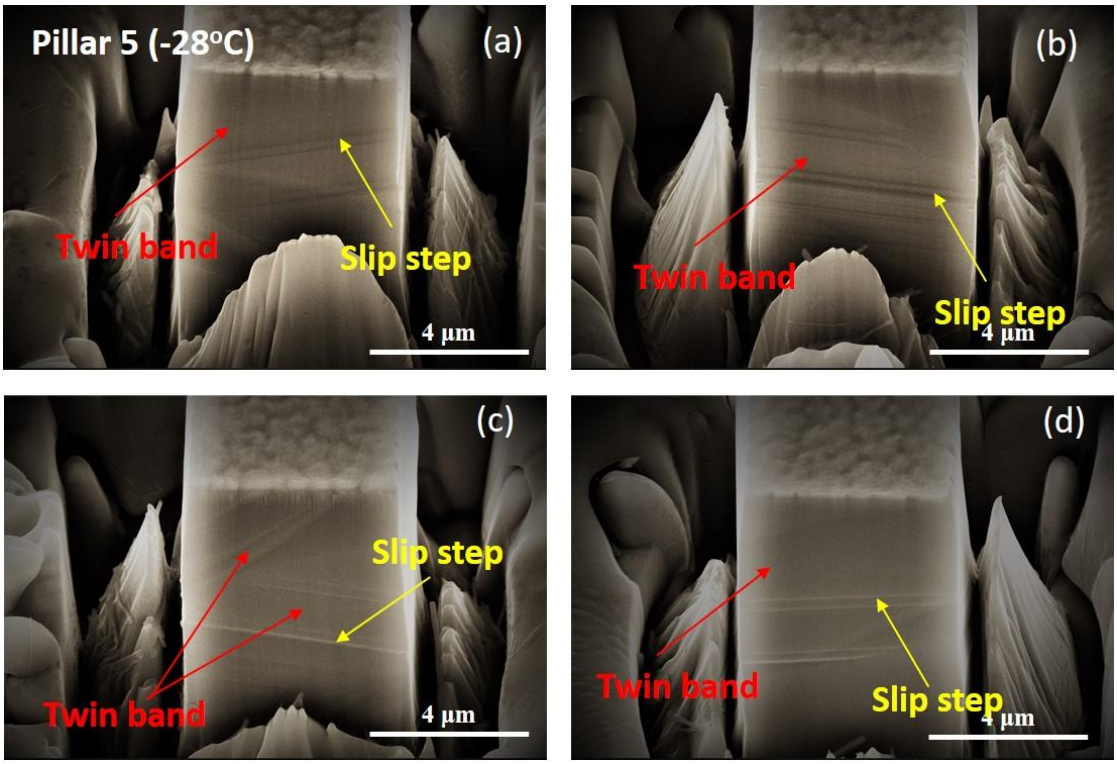

Figure 5.9: (a-d) Post-mortem SEM images of four faces of room -28°C compressed Pillar 5 with ~ 6.5 % strain. Twin bands and slip steps are apparent in (a-d) and highlighted in red colour and yellow colour respectively. All the images were taken with stage tilt of 30 degrees.

Figures 5.10 and 5.11 show the SEM images of Pillar 9 and Pillar 10 respectively, compressed at -94°C along the same loading direction. Pillar 9 and Pillar 10 have received strains of ~2.6 % and ~ 6.7% respectively. Figures 5.10 and 5.11 also show similar features of twin bands in both the pillars' surfaces, highlighted by red colour, and the slip-steps on the surface of Pillar 10 only, highlighted by yellow colour which suggests that the overall deformation mechanisms remained the same at all three test temperatures.

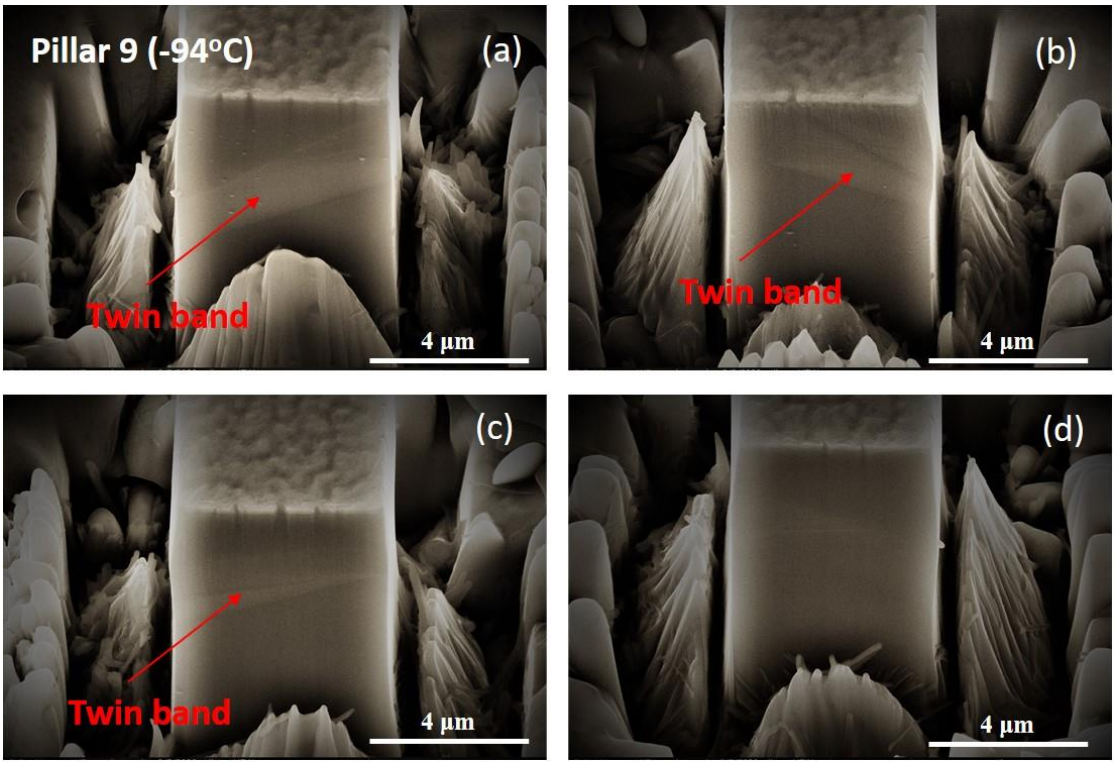

Figure 5.10: (a-d)Post-mortem SEM images of four faces of -94°C compressed Pillar 9 with ~2.6 % strain. Twin band is apparent in (a-c) and highlighted in red colour. All the images were taken with stage tilt of 30 degrees.

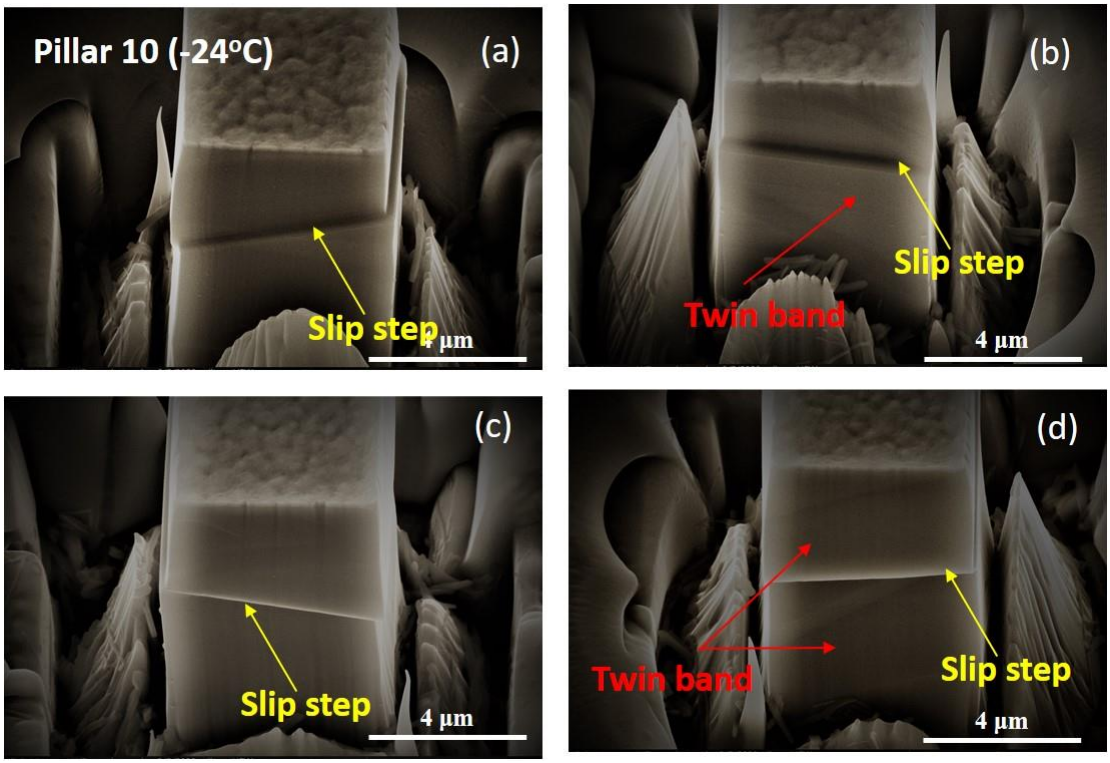

Figure 5.11: (a-d) Post-mortem SEM images of four faces of -94°C compressed Pillar 9 with ~6.7% strain. Twin band is apparent in (b and d) highlighted in red colour whereas slip steps are present in (a-d) and highlighted in yellow colour. All the images were taken with stage tilt of 30 degrees

5.1.3 Post-mortem TEM

5.1.3.1 Room temperature

To observe the substructure of the room temperature compressed [$1\bar{3}20$] micro-pillars, a TEM foil was extracted from Pillar 4, having compressed to ~6% strain, by the lift out method using FIB. The Pillar 4 was selected here for TEM analysis because it could reveal both the key features of twin bands and slip steps observed in the room temperature compressed micro-pillars (Figure 5.7). The TEM specimen was made along the loading axis. The stress-strain curve and SEM image of Pillar 4 are shown in Figures 5.12 (a) and (b) respectively, where red

dashed rectangle shows the position of the extracted TEM foil (Figure 5.12 (b)) with reference to the compressed pillar.

A montage of BF TEM images of the whole pillar is shown in Figure 5.13 (a) with BD ~ $[\bar{2}110]_{twin}$ using the 0002 reflection. There are two strain bursts of different magnitudes (length / size) apparent on the stress strain curve (Figure 5.12 a) and believed to be related to the two twin areas of different sizes in TEM Figure 5.13 (a). The larger twin covering most of the pillar from top to bottom in Figure 5.13 (a) is likely to correspond to the larger strain burst in the stress-strain curve. Additionally, a smaller twin can be seen near the pillar top surface in Figure 5.13 (a) which is likely due to the smaller strain burst in the stress-strain curve, marked by a black arrow in Figure 5.12 (a). The selected area diffraction patterns (SADP) from the matrix and the twinned regions are shown in Figures 5.13 (b-c). The angle between the basal planes in the matrix and the twinned region was measured to be ~86 degrees confirming $\{10\bar{1}2\}$tension twinning as the main deformation mode during compression along the $[1\bar{3}20]$ loading direction as this mode of twinning cause ~ 86 degree rotation of basal plane between matrix and twinned regions.

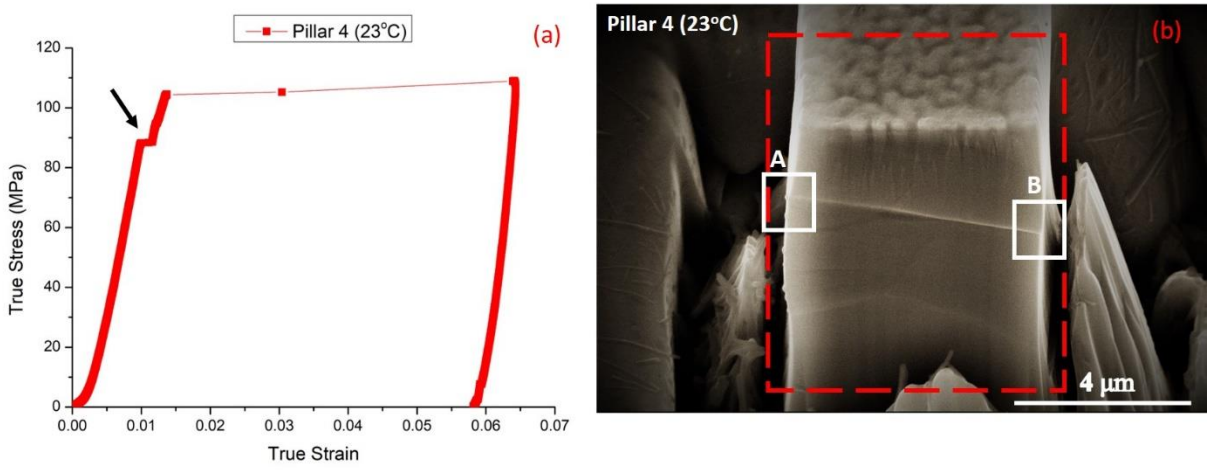

*Figure 5.12: (a) Stress-strain curve and (b) post-mortem SEM image of Pillar 4 compressed at 23°C. The black arrow in (a) shows the small strain burst. The red dashed rectangle in (b) is the position from where TEM foil was extracted and white small rectangles, marked as **A** and **B** are the positions of slip step across the micro-pillar face.*

The slip-step present in the SEM image, at positions A and B in Figure 5.12 (b), can also be identified in the TEM image, marked with the same lettering, traced with a white dashed line inside the large twin by connecting the small slip steps on both sides of the TEM image (Figure 5.13 (a)), which also indicates that the slip activity was taken place within the twinned region. Figure 5.13 (d and e) are magnified TEM images of the slip-step observed at Positions A and B in both SEM and TEM images. To investigate the origin of the slip-step, the crystal orientation of the twinned region was determined using TKD. The TKD data suggested that the loading axis of the twinned region is changed from $[1\bar{3}20]$, the initial loading direction of the micro-pillar before compression, to $[\bar{4}\ 8\ \bar{4}\ 15]$ (the new loading direction of the twinned region after compression). The Schmid factors of the various deformation modes for the

$[\bar{4}\ 8\ \bar{4}\ 15]$ loading direction are listed in Table 5.1. The lowest CRSS for basal slip combined with a Schmid factor of 0.4 explains the basal slip at the stress levels where strain bursts are appearing in the corresponding stress-strain curves. For schematic illustration, the crystal orientations of the twinned region and the matrix are drawn in Figure 5.13 (f).

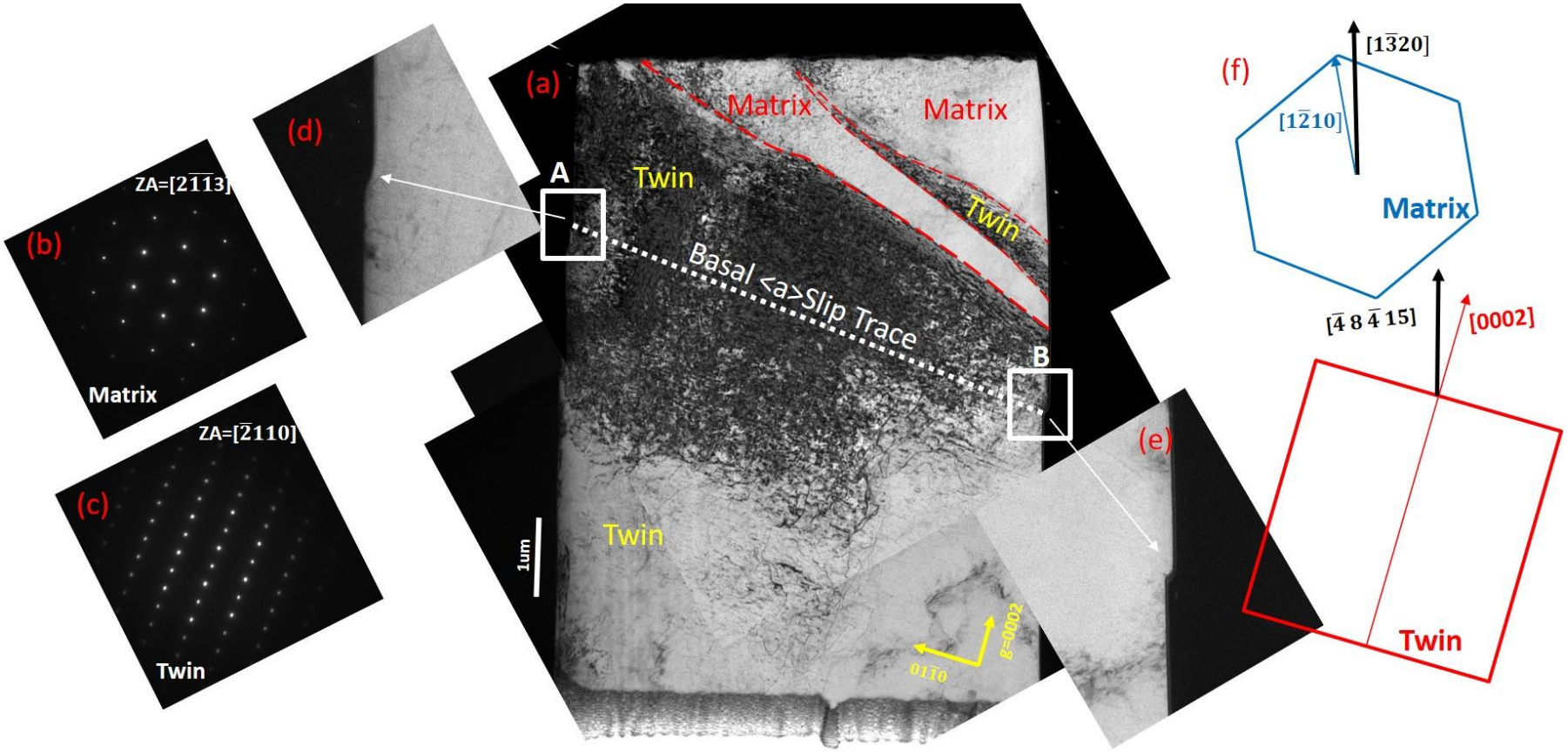

Figure 5.13: TEM data for Pillar 4 compressed at 23°C. (a) Montage of BF TEM images across the whole specimen with ***BD ~ [$\bar{2}$110]$_{Twin}$*** *using* ***g=0002*** *, (b) SADP of* ***ZA=*** *[**2$\bar{1}\bar{1}$3**] taken from the matrix (c) SADP of* ***ZA= [$\bar{2}$110]*** *from the twinned region, (d,e) magnified views of the positions* ***A and B*** *of (a) showing positions of slip-step, and (f) schematic illustration of the crystal orientations of the matrix and the twinned region*

In addition to the dominant twinning activity and the basal slip inside the twinned region, a high density of <**c**> or <**c+a**> dislocations can also be seen, within the twinned region, as shown in Figure 5.14. The image was taken from the area inside the twinned region marked as B in Figure 13 (a) with BD ~ $[\bar{2}110]$ using the 0002 reflection. Because the dislocations are visible using g=0002, the dislocations have either <**c**> or <**c**+**a**> Burgers vector and likely resulting from some pyramidal <**c+a**> slip activity inside the twinned region as well. However, it was not possible to distinguish between <c> and <c+a> in the current TEM specimen due to the difficulty in getting right diffraction imaging conditions for this purpose.

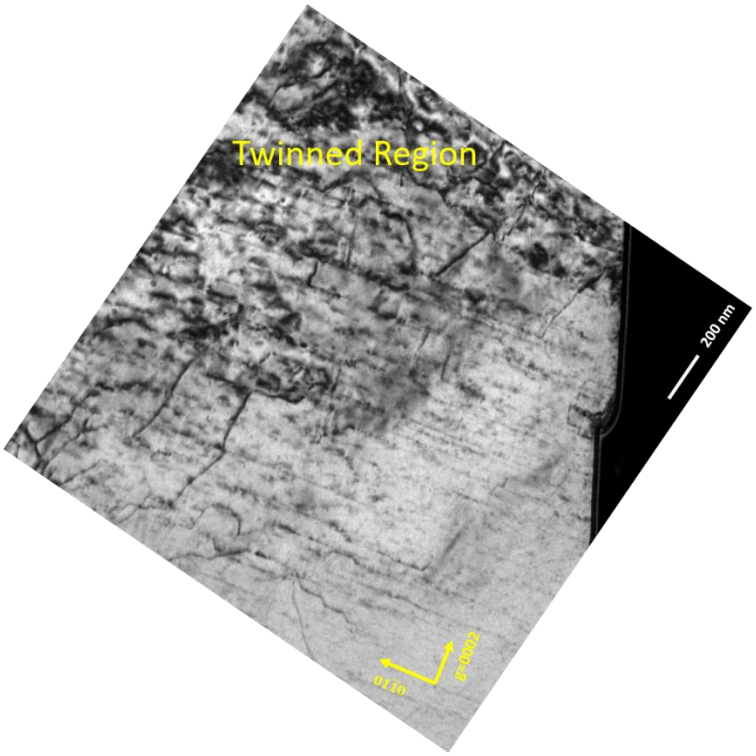

*Figure 5.14: TEM BF image from the area of Pillar 4 TEM specimen marked as position B in Figure 5.13 (a) within the twinned region using beam direction $[\bar{2}110]$ and g=0002. <**c**> component dislocations are visible with this imaging condition.*

5.1.3.2 Cryogenic temperatures

For cryogenic temperatures, a TEM specimen was made from Pillar 11, which had been compressed at -94°C to an overall strain of ~ 5%, taken as representative of the low temperature compression. The specimen was extracted along the loading axis. The SEM image and stress-strain curve for Pillar 11 are shown in Figure 5.15 (a, b). The red dashed rectangle in Figure 5.15 (b) shows the position of the TEM foil with respect to the compressed pillar. Figure 5.16 (a) shows a montage of BF TEM images across the whole pillar with BD ~ $[\bar{2}110]$ and g = 0002, with respect to the twinned region. This figure shows that there is one large twin corresponding to the large strain burst in the stress-strain curve. The SADPs from the matrix and twin are shown in Figure 5.16 (b) and (c). The angle between the basal planes in the matrix and twinned regions was measured to be ~ 86 degrees thus confirming $\{10\bar{1}2\}$ tension twinning as the main deformation mode at cryogenic temperatures as well.

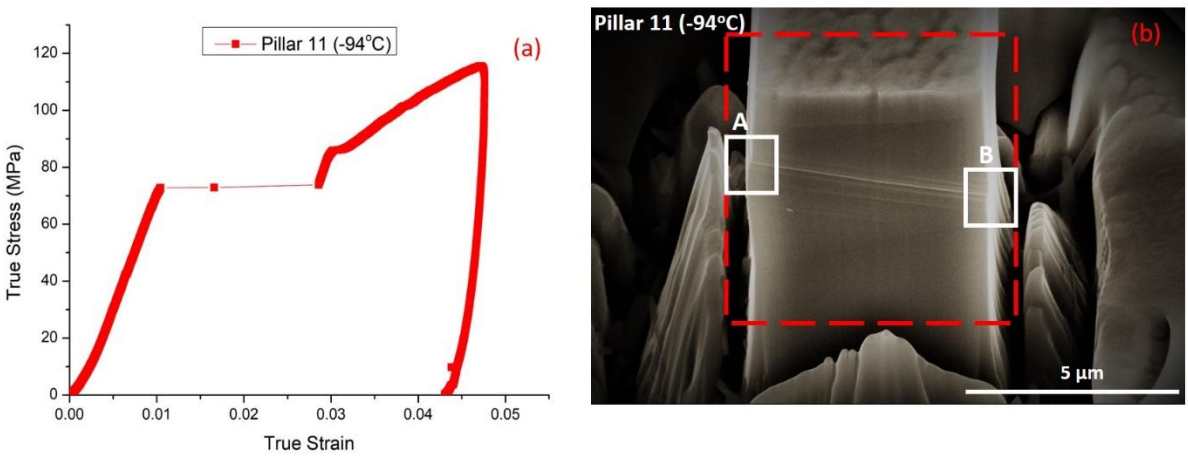

*Figure 5.15: (a) Stress-strain curve and (b) post-mortem SEM image of Pillar 11 compressed at -94°C. The red dashed rectangle in (b) is the position from where TEM foil was extracted and white small rectangles, marked as **A** and **B,** are the positions of slip step across the micro-pillar face.*

Figure 5.16 (a) also shows the presence of a slip step inside the twinned region after compression at -94°C, marked by the white dashed line between markings A and B. This slip step is the same that can also be seen in the corresponding SEM image of the compressed micro-pillar in Figure 5.15 (b), extending from one side of the pillar at position A to the other side of the pillar at position B. Figure 5.16 (d,e) are the TEM magnified views of the slip-step across the pillar surface. The reasons for the occurrence of the slip-step are the same as discussed above for RT deformation. The crystal orientations of the matrix and twinned regions are schematically presented in Figure 5.16 (f).

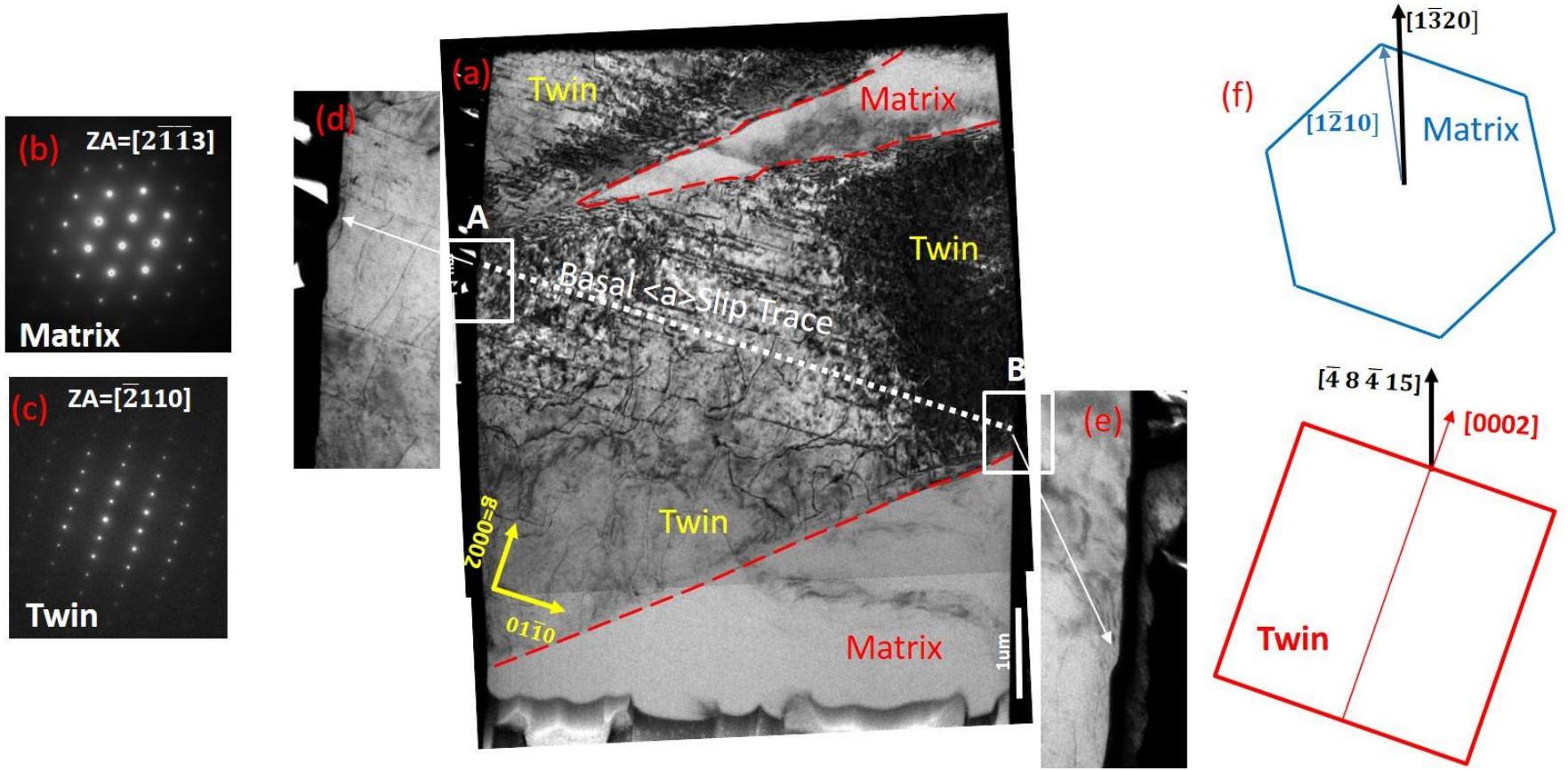

Figure 5.16: TEM data for Pillar 11 which was compressed at -94°C. (a) Montage of BF TEM images across the whole specimen with ***BD ~[$\bar{2}$110]$_{Twin}$*** *using* ***g=0002*** *, (b) SADP of* ***ZA=*** *[2$\bar{1}\bar{1}$3] taken from the matrix (c) SADP of* ***ZA= [$\bar{2}$110]*** *from the twinned region, (d,e) magnified views of the positions* ***A and B*** *of (a) showing positions of slip-step, and (f) schematic illustration of of the crystal orientations of the matrix and the twinned region*

Figure 5.17 shows the presence of non-basal dislocations of <c> or <c+a> character inside the twinned region resulting from pyramidal <**c+a**> activity. This TEM image was taken from position B inside the twinned region (Figure 5.16 (a)) with BD ~ $[\bar{2}110]$ using g=0002.

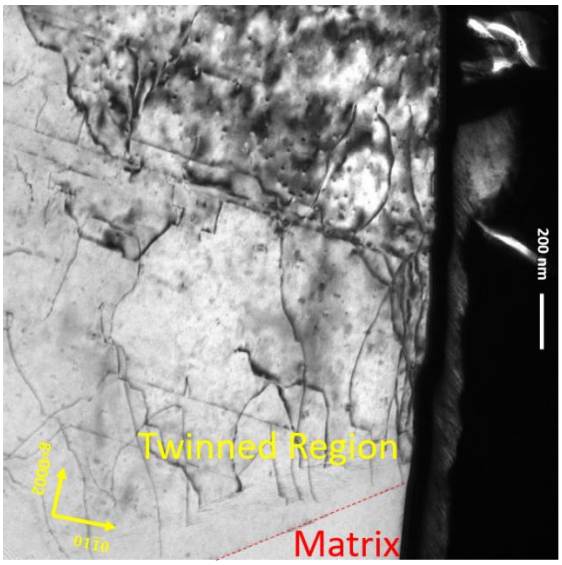

*Figure 5.17: TEM BF image from the area of TEM specimen of Pillar 11 marked as position B in Figure 5.16 (a) inside the twinned region using BD~ [$\bar{\mathbf{2}}$**110**] and g=0002.<c> component dislocations are visible in the twinned region with this imaging condition.*

5.2 Discussion

The stress-strain curves of the $[1\bar{3}20]$ oriented micro-pillars suggest that the micro-pillars deformed by similar plastic deformation mechanisms at all test temperature. The presence of strain bursts in the stress-strain curves and the post-mortem SEM and TEM observations confirm that tensile twinning was the main deformation mode at all three test temperatures for this loading direction. The rate of work hardening remained minimal during the strain burst events due to the accelerated twin growth and then increased rapidly due to the interaction

between the basal and non-basal dislocations within the (large) twinned region, as observed in the TEM images (Figures 5.14 and 5.17). The basal and non-basal (pyramidal <c+a>) slip systems are believed to be activated inside the twinned region here because loading direction of the twinned region was changed from $[1\bar{3}20]$ to $[\bar{4}\,8\,\bar{4}\,15]$ due to the twinning associated reorientation which enable these slip systems to become activated due to the increased Schmid factor (see Table 5.1) and hence, enhanced resolved shear stresses. The main difference lies in the size of the strain bursts which become smaller with the decrease in temperature as can be observed in Figure 5.4. Both the deformation modes, twin growth and the following basal slip activity are believed to be responsible for massive strain bursts in the stress strain curves at all the test temperatures [15]. With the decrease in test temperature, there is less thermal energy available to the mobile twinning dislocations and mobile basal <a> dislocations, thus, resulting in reduced mobility and, hence a slower rate of their propagation and smaller strain burst size.

The deformation mechanism of magnesium microcrystals compressed along the basal plane at room temperature has been investigated by different authors [15], [39], [40]. Under such loading conditions, tension twinning is reported to be the main deformation mode which agrees with the findings of this study. Plastic deformation by twinning starts with the nucleation of a twin embryo at a point of stress concentration during micro-pillar compression. Twin nucleation is a heterogeneous process and depends on localised stress concentration within the test specimen. In the case of bulk polycrystals, twin nucleation occurs at grain boundaries, twin boundaries, crystal defects and crack tips [87], [167], [168]. However, in this study, the twin embryo is likely to form near the top pillar surface as this is the point of highest stress concentration when the flat indentation tip first meets the pillar top-surface during a micro-pillar compression test. This is likely the reason to observe the presence of twin near the top pillar surfaces (Figures 5.13 and 5.16) in this study and other micro-pillar compression literature

[15], [39], [40], [169]. The second most likely place for high stress concentration is the pillar edges/corners of the square-shaped micro-pillars and thirdly Ga damage layer on the micro-pillar surface developed during micro-pillar fabrication using Ga FIB. While it is difficult to identify the true twin nucleation stress during micro-pillar compression, due to the stochastic nature of the twin nucleation, their occurrence, however, can be traced by the microplasticity events in the stress-strain curves as apparent in the inset to the Figure 5.18, where one stress-strain curve from each test temperature is plotted. After twin nucleation, the next stage is lateral twin propagation with a progressive increase in the applied stress necessary. Finally, a stress level is reached where rapid twin growth takes place, perpendicular to the shear direction, in an accelerated manner, through twin boundary migration. This stage of rapid twin growth is likely to be responsible for the strain bursts present in the stress-strain curves at all test temperatures.

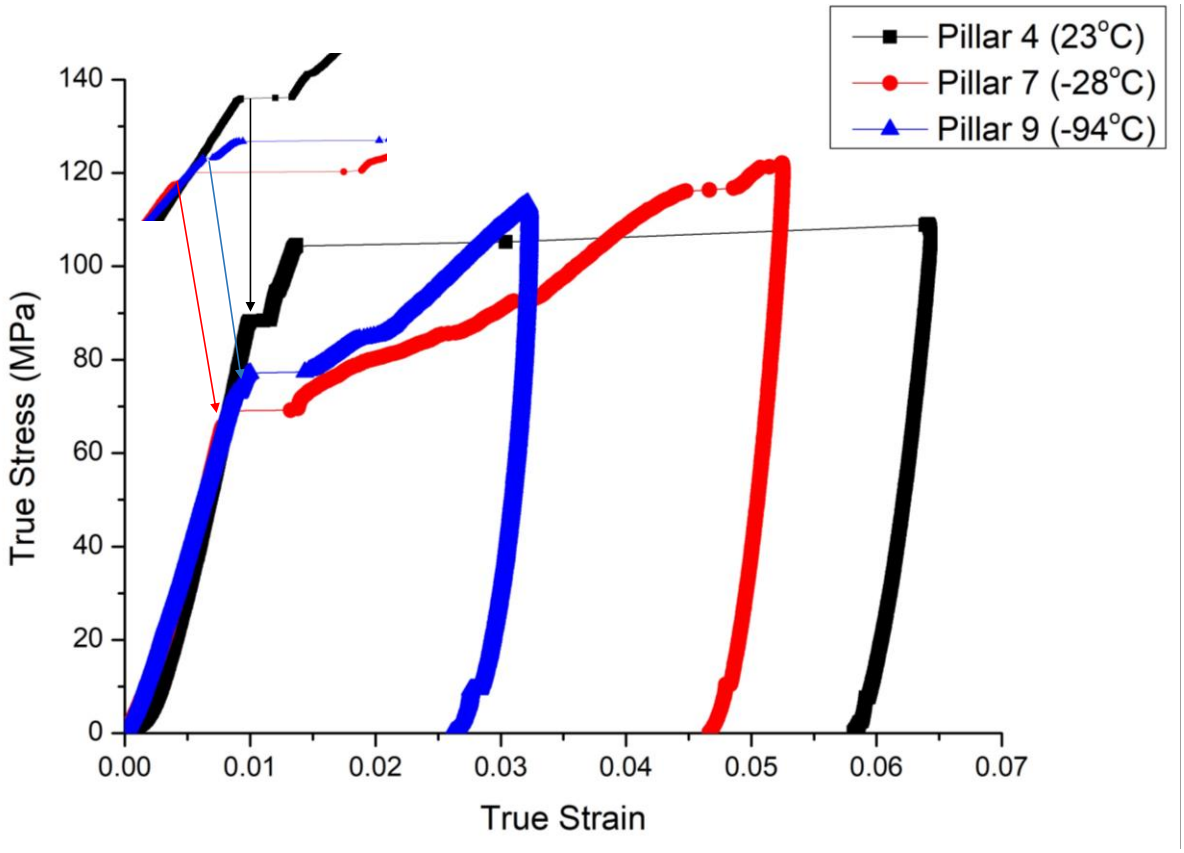

Figure 5.18: Stress-strain curves of [1$\bar{3}$20] oriented micro-pillars; one curve at each test temperature showing microplasticity bursts, magnified in the inset.

Experimentally, it is challenging to measure the true twin nucleation stress by micro-pillar compression in load control mode, due to heterogeneous twin nucleation, resulting from the local stress concentration. The onset of plasticity/yielding is therefore measured at 0.2% offset strain, which is believed to be occurred by the activation of tension twinning, and corresponding CRSS for the twin activation / nucleation were computed at all the three test temperatures. The variation in the yield stress with temperature has been shown in Figure 5.5. This plot clearly shows that there is no change in the yield stress due to the activation of tension twinning with the temperature between room temperature and -94°C, which indicates that the yield stress and hence the CRSS for the twin activation / nucleation is not temperature sensitive in the current

test temperature range. The temperature insensitivity of the yield stress observed here is likely due to the more pronounced role of local stress concentration state than the effect of temperature on the twin nucleation stress. This is likely to mitigate the effect of temperature on twin nucleation stress and hence on the yield stress. This is dissimilar to the conclusions drawn by Barrett et al. [170]. They reported a decrease in twin nucleation stress with the increase in temperature from -173°C and 127°C during a molecular dynamics study of "stress-free" perfect magnesium single crystals. It must be pointed out that, in their simulation, Barret et al. do not include any stress concentrators like point defects, pre-existing dislocations or free surface effects. Hence, the difference between the present study and the simulation work of Barrett et al. [170] is the state of stress under which twin nucleation stress is studied for the temperature dependence.

There is no previous experimental study reported on the temperature dependence of CRSS of tension twinning using uniaxial compression on magnesium single crystal at any length scale, neither below the room temperature nor above the room temperature. On macro-scale level, Bhattacharya [28] performed uniaxial tension on magnesium single crystal specimens favourably oriented for tension twinning between 27°C and -269°C whereas Chapuis et al. [94] employed plain strain compression between 25°C and 450°C . However, in both these studies, no significant effect of temperature on CRSS of tension twinning was reported at the macro-length scale which is similar to the trend observed in present study at micron length scale.

Another important aspect of tensile twinning is the rapid twin growth which is also analyzed here. The occurrence of twin growth can be characterized by massive strain bursts in the stress-strain curves as apparent in Figures 5.1 – 5.3. In this regard, the stress at which the massive strain burst occurred is taken as twin growth stress. The CRSS for twin growth is then computed

for each micro-pillar showing massive strain burst in their stress strain curves at all test temperatures and plotted as a function of temperature in Figure 5.19. The room temperature values of CRSS for twin growth have a large scatter due to the stochastic nature of twinning, but these values are in line with the past literature for similar-sized specimens [39], [171], [172]. The CRSS values at -28°C and -94°C lie within the scatter of room temperature CRSSs for twin growth, showing no change in CRSS for twin growth with the change in temperature. This temperature insensitivity of CRSS for twin growth can be explained by exploring the mechanism of twin growth. Recently, micro-pillar compression has been used to study the influence of alloy content, pillar size and temperature on the critical stresses associated with twin growth in magnesium single crystals [39], [171], [172]. In the context of the present work, Sim et al. [39] reported a similar temperature insensitivity of twin growth in magnesium between 0°C to 75°C, but an increase in CRSS for twin growth at 100°C. They attributed this "anomalous" increase in CRSS for twin growth at 100°C to the annihilation of glissile twinning dislocations from the pillar surface at a higher temperature which otherwise would have been responsible for twin boundary migration. The source of these glissile twinning dislocations is likely the interaction between prismatic dislocations and the twin boundary [173]–[175]. So, at the higher temperature, the lack of available mobile dislocation segments would result in higher stresses for the concurrent twin growth by requiring the activation of less favourable dislocation sources. Following the same logical argument, the temperature insensitivity of the CRSS of twin growth below room temperature can also be explained. At cryogenic temperatures, since these glissile twinning dislocations remain within the pillar specimen without affecting the number of mobile dislocation segments, so the stress required for twin growth remained unaffected. However, lowering the temperature is likely to affect the mobility of these twinning dislocations due to the increase in Peierls lattice friction resulting in the smaller strain bursts in

the stress-strain curves observed at cryogenic temperatures as compared to room temperature (Figures 5.4 and 5.18).

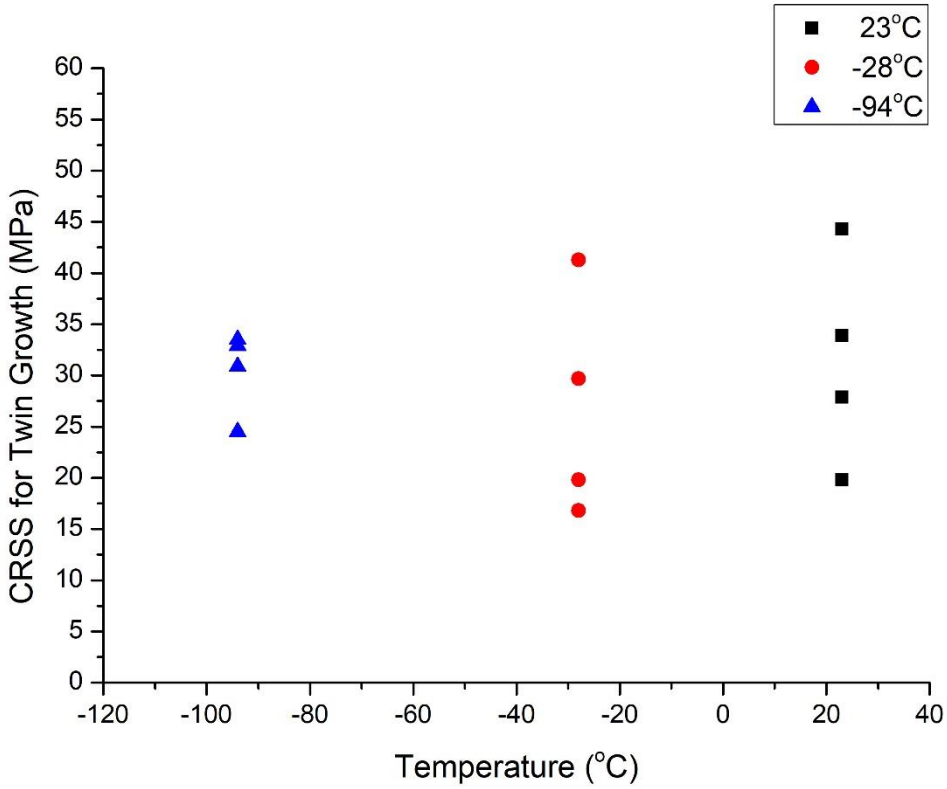

Figure 5.19: Temperature vs CRSS of twin growth for all the micro-pillars

5.3 Summary

The temperature dependence of tensile twinning in magnesium single crystals has been studied via micro-pillar compression. $[1\bar{3}20]$ oriented micro-pillars were compressed at room temperature, -28°C and -94°C. The stress-strain curves mostly showed prominent strain bursts on the onset of plasticity indicating activation of twinning in the temperature range between 23°C to -94°C for this loading direction. Post-mortem SEM and TEM confirmed $\{10\bar{1}2\}$ tensile twinning as the main deformation mode followed by basal <a> slip and pyramidal <c+a> slip

within the twinned region. The CRSS for twin nucleation and the CRSS for twin growth was measured from the stress-strain curves. The comparison between the CRSSs for the twin nucleation and for the twin growth at different temperatures indicate the temperature insensitivity for both the critical stresses associated with the tension twinning. The temperature insensitivity of CRSS of twin nucleation is likely due to the heterogeneous nature of twin nucleation during micro-pillar compression, where the role of stress concentrators on the twin nucleation stress is suggested to be more pronounced than the influence of temperature. Similar to the trend in CRSS for twin nucleation, the CRSS for twin growth is also found to be temperature insensitive which is likely related to the mechanism of initiation of twin growth based on the available dislocation sources and mobile dislocation segments that are suggested to remain unaffected under the influence of temperature within the temperature range between 23°C and -94°C.

6 Temperature dependence of pyramidal <c+a> slip

6.1 Results

In the third group of experiments, uniaxial compression was performed on square shaped micro-pillars of magnesium single crystals along the [0001] loading direction at 23°C, -20°C and -90°C to study the temperature dependence of pyramidal <c+a> slip in magnesium. Three micro-pillars were compressed at each test temperature. The experiments were carried out in load-controlled mode with a loading rate of 1000 μN/s that resulted in an initial strain rate of ~2.5 x 10^{-3} s^{-1}. Three micro-pillars were compressed at each test temperature with varying peak loads ranging between 8000 μN to 14000 μN. The Schmid factors for different deformation modes for the [0001] loading direction are listed in Table 6.1 along with their CRSSs taken from the past literature. Based on the CRSS values, basal <a> slip is the easiest mode to activate in magnesium, but the Schmid factor for this deformation mode along with prismatic <a> slip is zero for the [0001] loading direction resulting in a minimum chance of their activation. Instead, second order pyramidal <c+a> slip on the $\{11\bar{2}2\}$ planes is expected for this loading direction and this is what has been previously reported [15], [18], [58], [135]. Therefore, [0001] oriented micro-pillars were selected to study the influence of temperature on the activation of pyramidal <c+a> slip in magnesium single crystals.

Table 6.1: CRSS for different deformation modes reported in past literature along with the Schmid factor for loading direction of [0001]

Deformation Mode	**CRSS** (MPa)	**Schmid Factor (m)**
		LD ~[0001]
Basal <a>	0.5 [20], [23], [24]	0.00
Prismatic <a> slip	39 [32]	0.00
Pyramidal <c+a>	40 [44]	0.45
Tension twinning	12 [158]	0.50

6.1.1 Stress-strain curves

6.1.1.1 Room temperature

The stress-strain curves of [0001] oriented micro-pillars, compressed at room temperature, are shown in Figure 6.1. Initially, the micro-pillars deformed elastically to a point where the change from elastic to plastic deformation as evidenced by strain bursts, marked with green arrows on the stress-strain curves (see Figure 6.1). The micro-pillars deformed plastically afterwards with an increasing rate of work hardening until a massive strain burst appeared around ~ (8-10)% strain, marked with yellow arrows in the case of Pillar 2 and Pillar 3 in Figure 6.1, even before reaching the peak load that was set up at the start of the compression experiment.

The stress at which first strain burst (of size > 0.1% strain) appears in the respective stress-strain curves is taken as the yield point. The average yield point for [0001] oriented micro-pillars was measured to be 285 ± 15 MPa and corresponding CRSS value for the pyramidal <c+a> slip was calculated to be 128 ± 7 MPa.

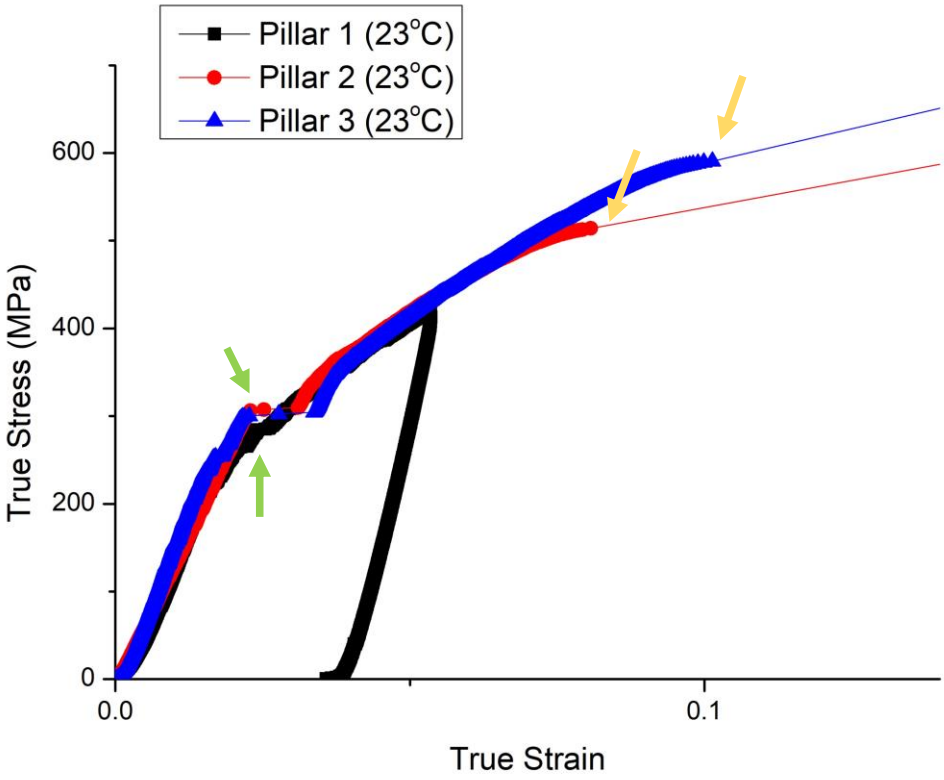

Figure 6.1: Stress-strain curves of [0001] oriented micro-pillars compressed at 23°C. Green arrows show the positions of strain bursts at yield whereas yellow coloured arrows show the positions of subsequent massive strain bursts.

6.1.1.2 Cryogenic temperatures

Figures 6.2 and 6.3 present stress-strain curves for [0001] oriented micro-pillars compressed at -20°C and -90°C respectively. The characteristic of the stress-strain curves of the micro-pillars compressed at cryogenic temperatures are similar to those for room temperature ones; the initial elastic deformation regime terminated with the appearance of a strain burst, marked with green arrows in Figures 6.2 and 6.3. Further deformation then took place with likewise a rapid rate of work hardening. However, there are no massive strain bursts present at the ends of the stress-strain curves at both cryogenic test temperatures which were present in the case of room temperature tested Pillars 2 and 3 (Figure 6.1).

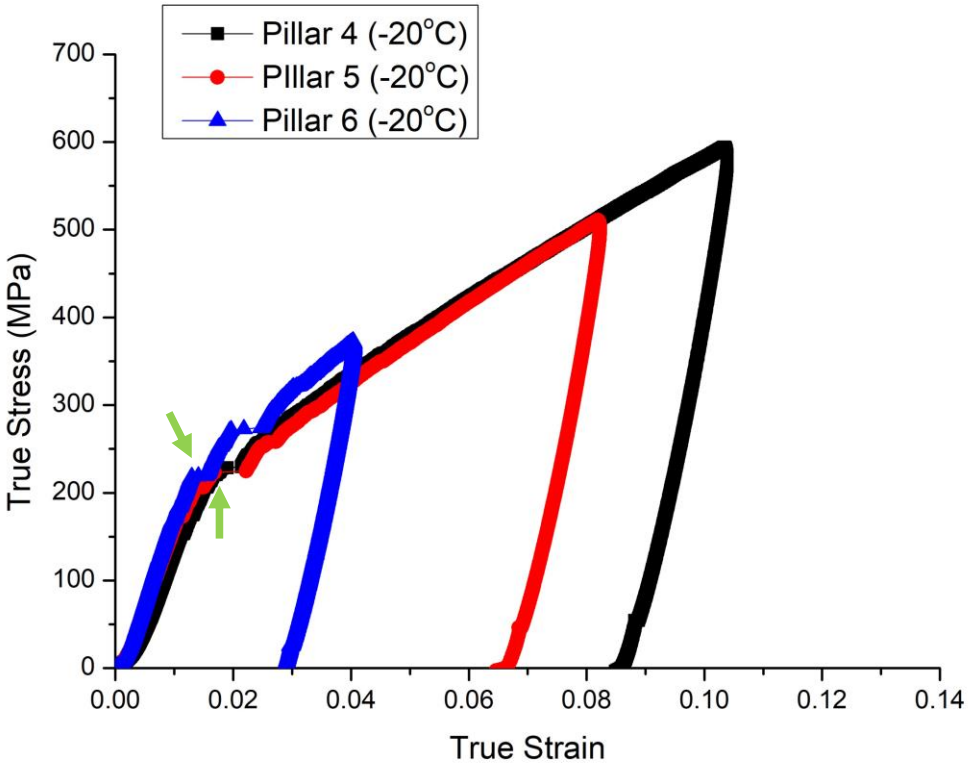

Figure 6.2: Stress-strain curves for [0001] oriented micro-pillars compressed at -28°C. Green arrows show the positions of strain bursts at yield

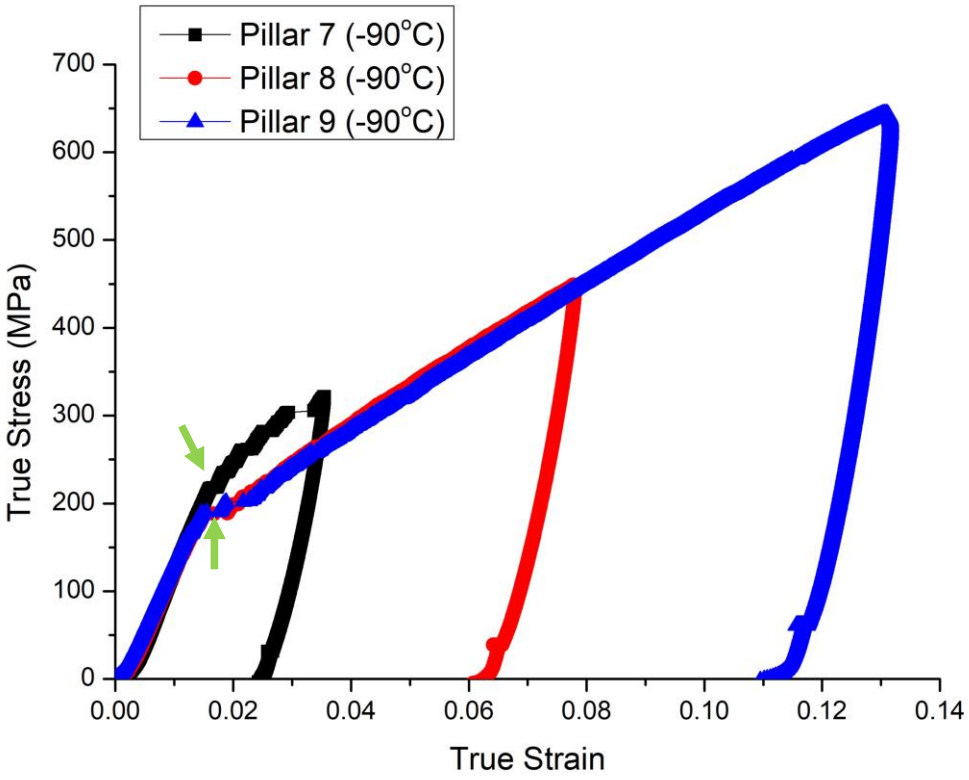

Figure 6.3: Stress-strain curves of [0001] oriented micro-pillars compressed at -90°C. Green coloured arrows show the positions of strain bursts at yield

From these stress-strain curves; the yield stress was measured as the stress of first strain burst (of size > 0.1% strain) in the same way as that of room temperature micro-pillars. The yield stress was measured to be 215 ± 8 MPa and 198 ± 15 MPa at -20°C and -90°C respectively and the corresponding CRSS values were calculated to be 97 ± 4 MPa and 89 ± 7 MPa respectively for the activation of pyramidal <c+a> slip.

To compare the mechanical behaviour of [0001] oriented micro-pillars at different test temperatures, one curve for each test temperature is plotted in Figure 6.4 and the variation of yield stress with temperature is plotted in Figure 6.5. Figures 6.4 and 6.5 suggest that the yield stress for pyramidal <c+a> slip is decreasing with decreasing temperature and the strain at any

level of flow stress during the course of plastic deformation is more at the low temperatures than at room temperature. A summary of the yield stress values, along with the CRSSs, obtained at different test temperatures for the activation of pyramidal <c+a> slip is presented in Table 6.2.

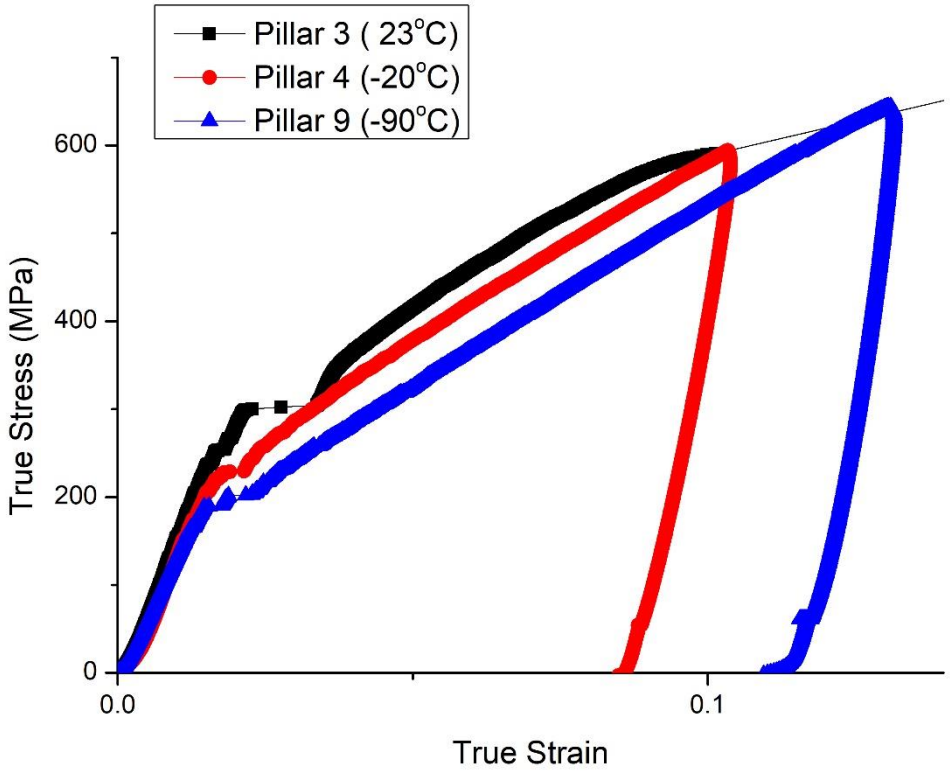

Figure 6.4: Stress-strain curves of [0001] oriented micro-pillars; one curve at each test temperature.

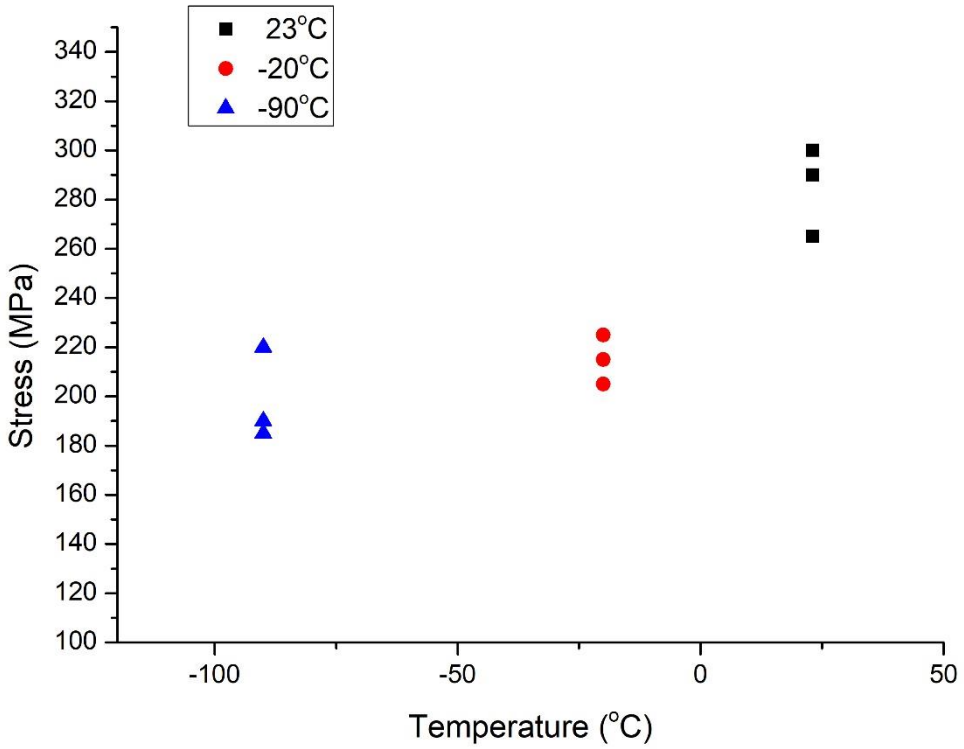

Figure 6.5: Variation in yield stress with test temperature for all [0001] oriented micro-pillars

Table 6.2: Yield stress and CRSS values of pyramidal <c+a> slip for all the [0001] micro-pillars tested at different test temperatures.

Pillar Number	**Temperature** (°C)	**Yield Stress** (MPa)	**Average Yield Stress** (MPa)	**CRSS** (MPa)	**Average CRSS** (MPa)
1	23	265	285 ± 15	119	128 ± 7
2		300		135	
3		290		130	
4	-20	225	215 ± 8	101	97 ± 4
5		205		92	

6		215		97	
7	-90	220	198 ± 15	99	89 ± 7
8		190		86	
9		185		83	

6.1.2 Post-mortem SEM

6.1.2.1 Room temperature

The post-mortem SEM images of room temperature compressed [0001] micro-pillars are shown in Figure 6.6 (a-c). There were two different features observed in these micro-pillars: no deformation marks in the case of Pillar 1 (Figure 6.6 (a)), (a strain ~3%) and sudden collapse of Pillars 2 and 3 (Figure 6.6 (b,c) after achieving strains of ~9% at around 550-600MPa. Absence of any deformation marks on Pillar 1 is likely due to the distribution of strain on six equivalent pyramidal planes as a result of compression along the [0001] loading direction making slip on any individual pyramidal plane not enough in magnitude to reach the pillar surface. In the case of Pillars 2 and 3, their appearance suggests that some chunk from the middle of the pillars has sheared out as top and bottom parts of the pillars can be seen retaining their square shapes (Figure 6.6 (b,c)). The collapse of these two pillars corresponds to the massive strain bursts at the end of the stress-strain curves (Figure 6.1). Similar observations of the sudden collapse of micro-pillars have also been reported by other authors [15], [18], [56], [58] during c-axis micro-pillar compression of magnesium single crystals. Such collapse of the [0001] oriented micro-pillars is believed to be related to the instability in the micro-pillars caused by the slight bending of the pillars likely due to the pyramidal <c+a> slip rather than the misalignment between the indenter and pillar.

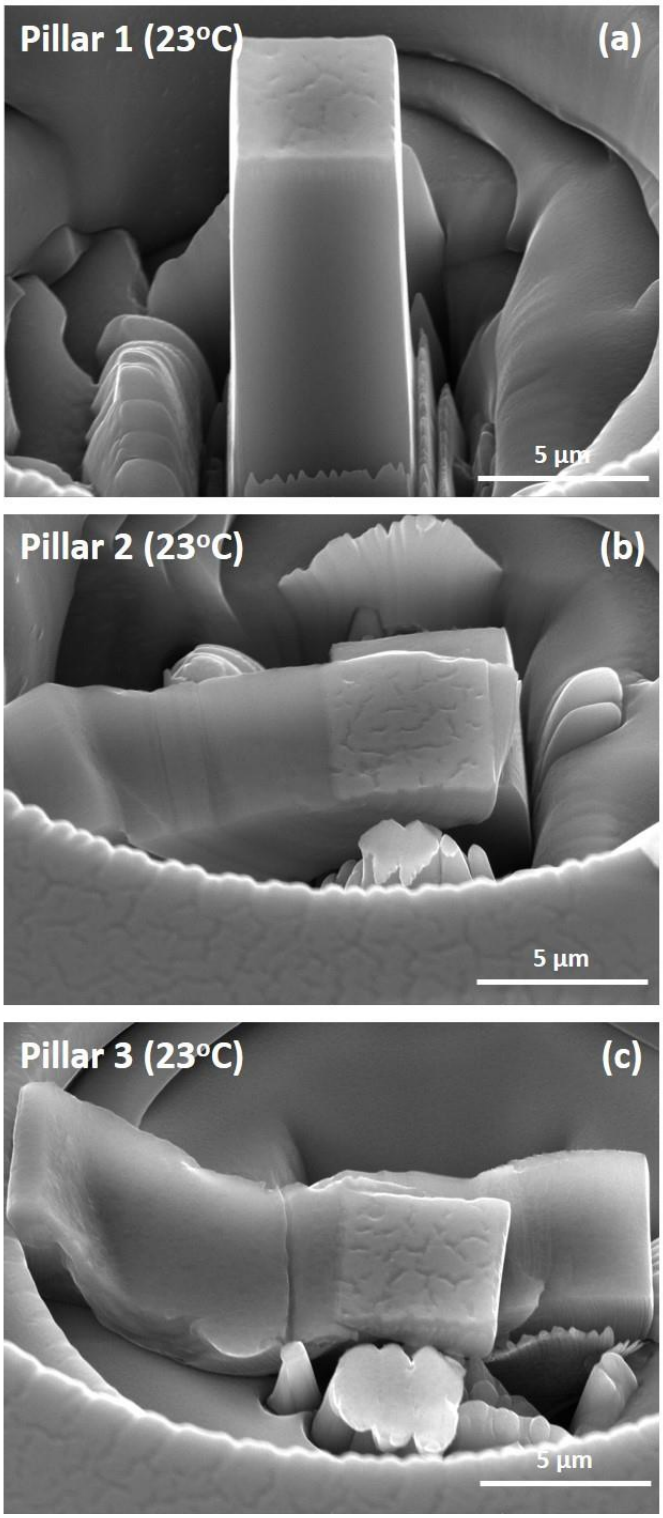

Figure 6.6: (a-c) Post-mortem SEM images of Pillars 1,2 and 3 compressed at 23°C. (b,c) sudden collapse of Pillars 2 and 3

6.1.2.2 Cryogenic temperatures

Figures 6.7 and 6.8 show post-mortem SEM images of [0001] micro-pillars deformed at -20°C and -90°C respectively with varying strain levels. Both sets of micro-pillars show no signs of deformation marks on their surfaces, even in pillars with higher strain levels like Pillar 4 with 9% strain (Figure 6.7) compressed at -20°C, and Pillar 9 with 11% strain (Figure 6.8) tested at -90°C. In comparison to the room temperature tests, there was no pillar collapse at any of the cryogenic test temperatures. However, slight bending is observed in the case of Pillar 5 (-20°C), and Pillars 8 and 9 (-90°C), marked by blue arrows in their respective SEM images. The similar sort of bending is hinted in the previous section for room temperature compressed Pillars 2 and 3 (see Figure 6.6 (b, c)) which then lead to the unstable shearing out of some middle part of the pillar causing the collapse. At cryogenic test temperatures, observations of slight bending in the compressed micro-pillars only at higher strain levels suggests that this phenomenon is not a result of issues related to the compression test procedure, but rather is related to the underlying deformation mode of pyramidal <c+a> slip in these groups of micro-pillars. The bending observed here is non-directional indicating that it is not related to the misalignment issues but rather likely due to the simultaneous activation of <c+a> slip on six equivalent pyramidal $\{11\bar{2}2\}$ planes, beyond certain strain level, which are systematically distributed with respect to the [0001] loading axis [15], [18], [56].

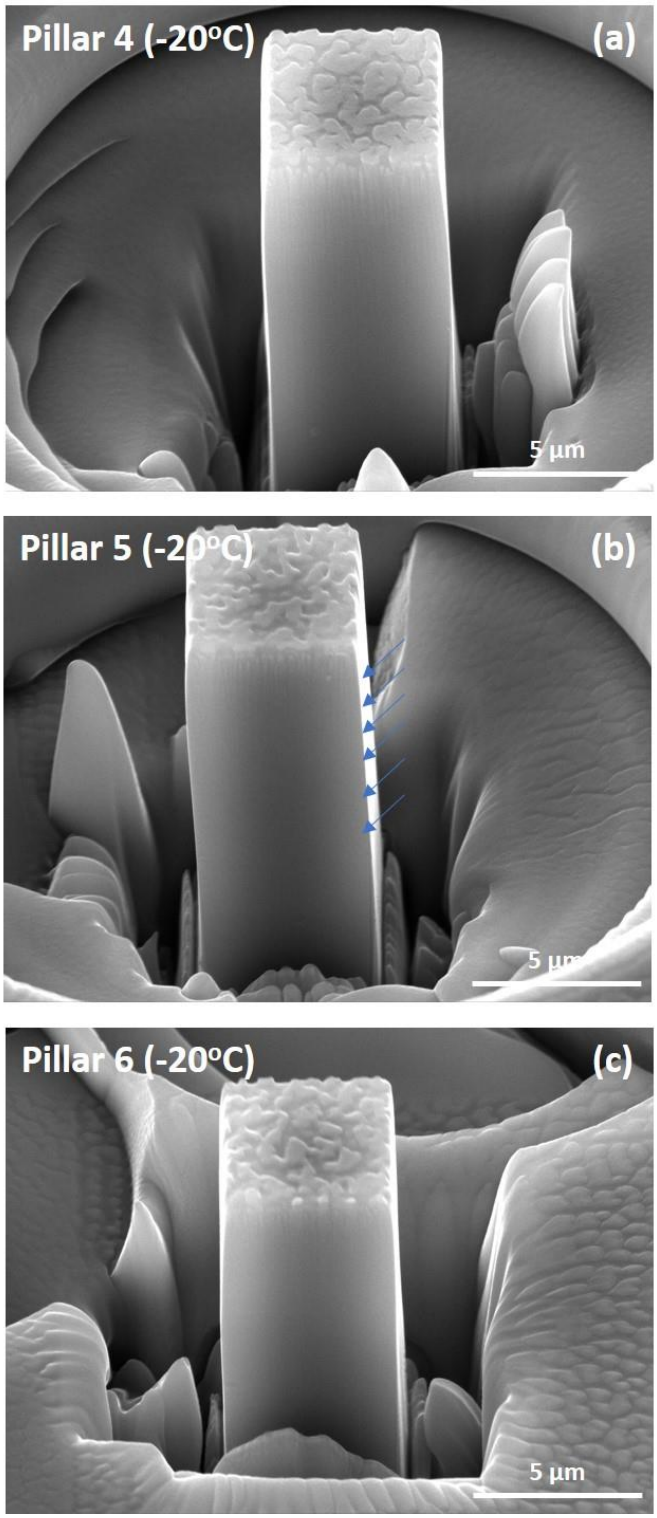

Figure 6.7: (a-c) Post-mortem SEM images of Pillar 3, 4 and 5 compressed at -20°C. (b) a slight bending in Pillar 2 highlighted with blue arrows.

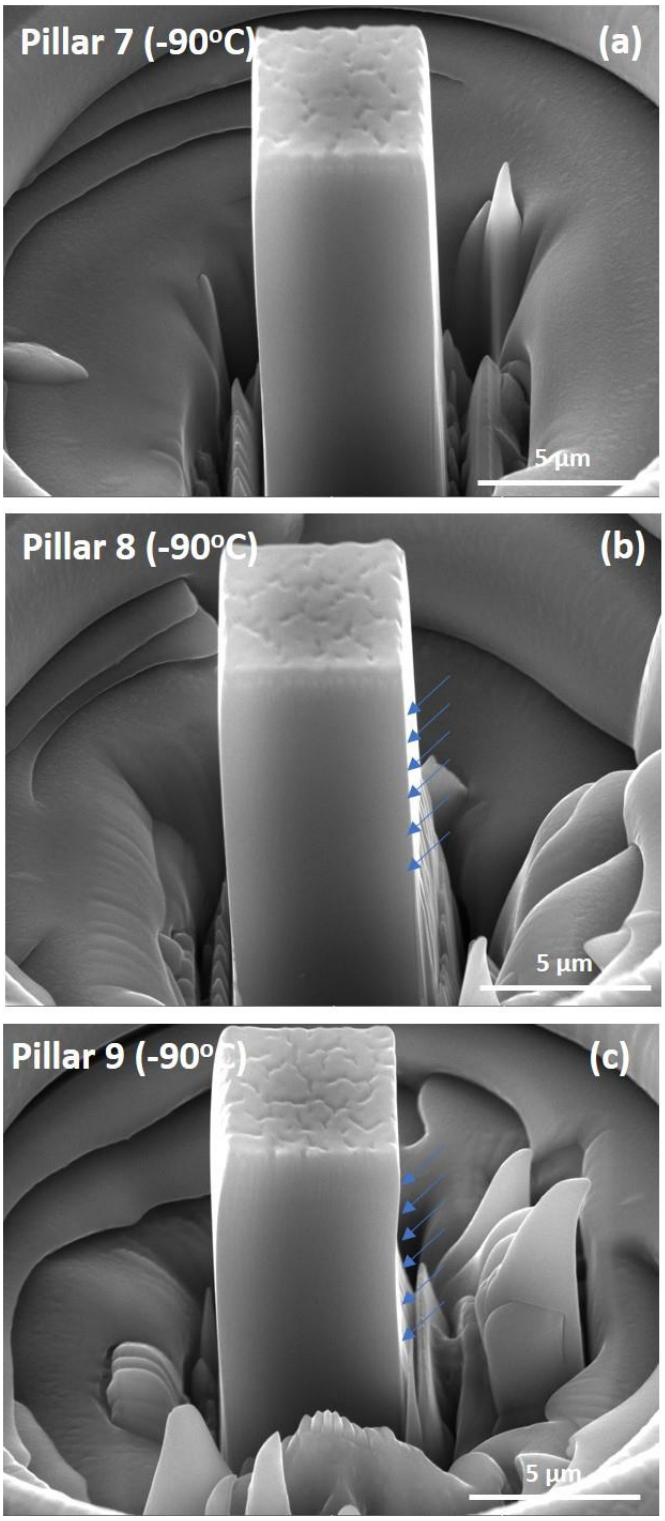

Figure 6.8: Post-mortem SEM images of Pillar 7, 8 and 9 compressed at -90°C. (b,c) slight bending in Pillar 2 and 3 highlighted with blue arrows.

6.1.3 Post-mortem TEM

6.1.3.1 Room temperature

For post-mortem TEM analysis of room temperature compressed [0001] oriented micro-pillars, a TEM foil was made from a pillar compressed to ~1.5 %. The TEM specimen was extracted parallel to the loading axis having a foil normal ~$[\bar{4}310]$. The BF TEM images of a section of the TEM foil are shown in Figure 6.9. The images were taken with BD ~$[\bar{2}110]$ using g=0002 (Figure 6.9 (a)) and using g=$01\bar{1}0$ (Figure 6.9 (b)). A schematic illustration of different types of dislocations observed in the TEM specimen is collectively shown in Figure 6.9 (c). According to the g.b criterion, the <c+a> dislocations should be visible under both imaging conditions while <c> dislocations should only be visible when g=0002 and invisible when g=$01\bar{1}0$. In this regard, the <c+a> dislocations can be seen to be visible in both images and are marked in yellow (Figure 6.9 (a). Whereas <c> dislocations can only be seen in Figure 6.9 (b) with g=0002 and they are marked in red. Some <a> type dislocations are also present in Figure 6.9 (b) with g=$01\bar{1}0$ and are marked in green. The presence of <c+a> dislocations confirms that pyramidal <c+a> slip is the main deformation mode in this group of micro-pillars at room temperature; the <c> and <a> dislocations are likely the result of the dissociation of sessile <c+a> edge dislocations to acquire energetically more stable configuration. Some of the <c+a> dislocations are showing a stair-like / zig-zag morphology, marked as 1 and 2 in Figures 6.9 (a,c), likely due to the cross-slip of <c+a> dislocations between different pyramidal planes. Figure 6.10 (a) shows magnified image of the dislocation marked as '1' in Figure 6.9 and Figure 6.10 (b) is the schematic illustration of the double cross slip mechanism by which <c+a> acquires the stair-like / zig-zag configuration [49], [50]. Due to the high density of dislocations generated during micro-pillar compression and the possible FIB damage, which resulted in poor

dislocation contrast, it was not possible to determine the Burgers vectors of the individual <c+a> dislocations.

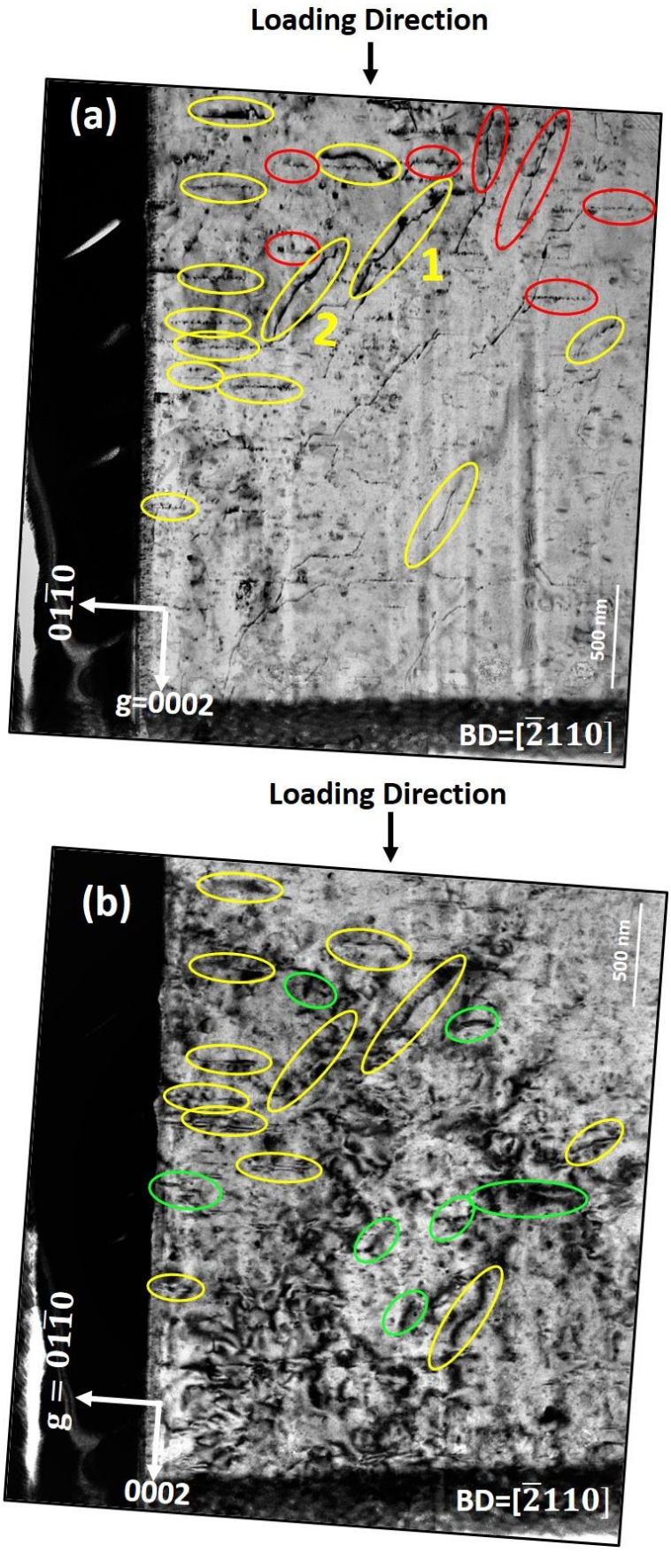
Loading Direction
(a)
1
2
$01\bar{1}0$
g=0002
500 nm
BD=[$\bar{2}$110]
Loading Direction
(b)
500 nm
g = $01\bar{1}0$
0002
BD=[$\bar{2}$110]

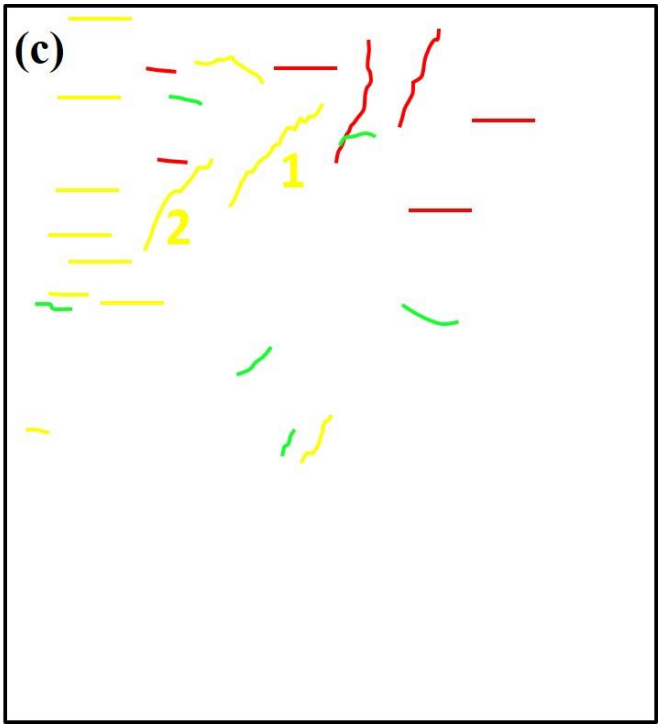

Figure 6.9: BF TEM images of a section of TEM foil taken from a micro-pillar compressed at room temperature to ~1.5% strain with BD ~ $[\bar{2}110]$ *using g=0002 (a), and g=*$01\bar{1}0$ *(b). (c) A schematic illustration of the <c+a>, <c> and <a>t types of dislocations observed in the TEM specimen. <c+a> dislocations are highlighted in yellow (a-c), <c> dislocations are highlighted in red (a,c), <a> dislocations are highlighted in green colours (b,c), and yellow numbered <c+a> dislocations are apparently following stair-like morphology (a,c)*

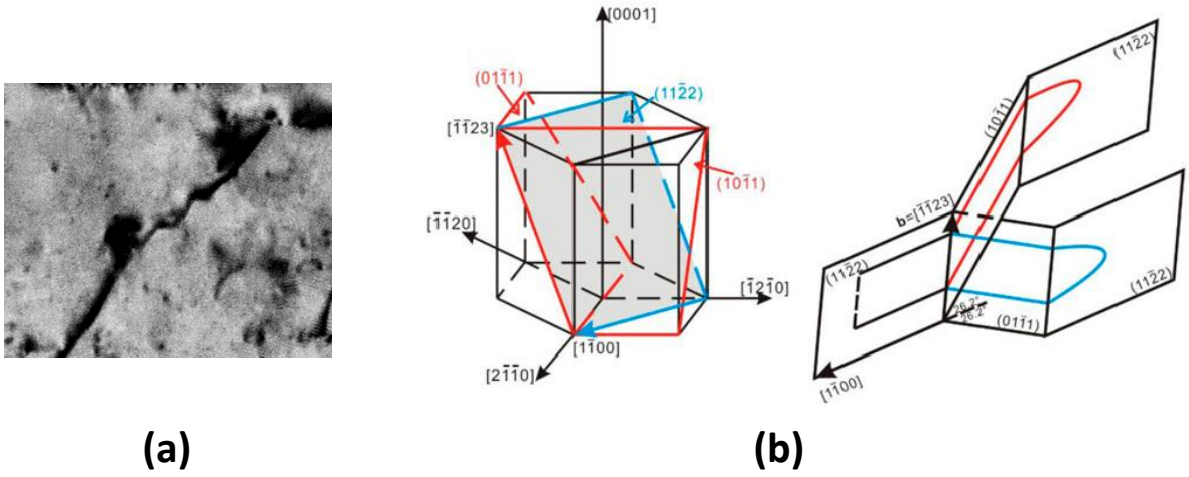

Figure 6.10. Magnified image of <c+a> dislocation with stair-like / zig-zag configuration marked as '1' in Figure 6.9 and (b) schematic illustration of the double cross-slip between pyramidal 1 and pyramidal II planes [50]

6.1.3.2 Cryogenic temperatures

To represent cryogenic temperatures, a TEM specimen was made from a micro-pillar, compressed to ~3% at -90°C. The specimen was made, using FIB, parallel to the loading axis with foil normal ~$[\bar{2}110]$. The BF TEM images of a section from the TEM foil are presented in Figure 6.11. The images were taken with BD ~ $[1\bar{1}00]$ using g=0002 (Figures 6.11 (a)) and g = $11\bar{2}0$ (Figure 6.11 (b)). A schematic illustration of different types of dislocations observed in the TEM specimen is collectively shown in Figure 6.11 (c). Following the g.b criterion, the <c+a> dislocations can be seen in both of the images as highlighted in yellow while <c> dislocations are marked in red and are visible only in Figure 6.11 (a) when g=0002. One of the dislocations present in Figure 6.11(b) is also identified as an <a> dislocation, marked in green and satisfying the visibility criterion of g.b ≠ 0. To confirm the presence of stair-like shaped <c+a> dislocations, Weak Beam Dark Field (WBDF) images (at a higher magnification) from the same section are shown in Figure 6.12 (a,b) using the same imaging conditions and shown

schematically in Figure 6.12 (c). The <c+a> dislocations highlighted by yellow numbers in both the images are showing a stair-like morphology, thus indicating some cross-slip at -90°C as well. The presence of <c+a>, <c> and <a> dislocations in these BF and DF TEM images suggests that the overall deformation mechanism remains the same at cryogenic temperatures as at RT, including cross-slip.

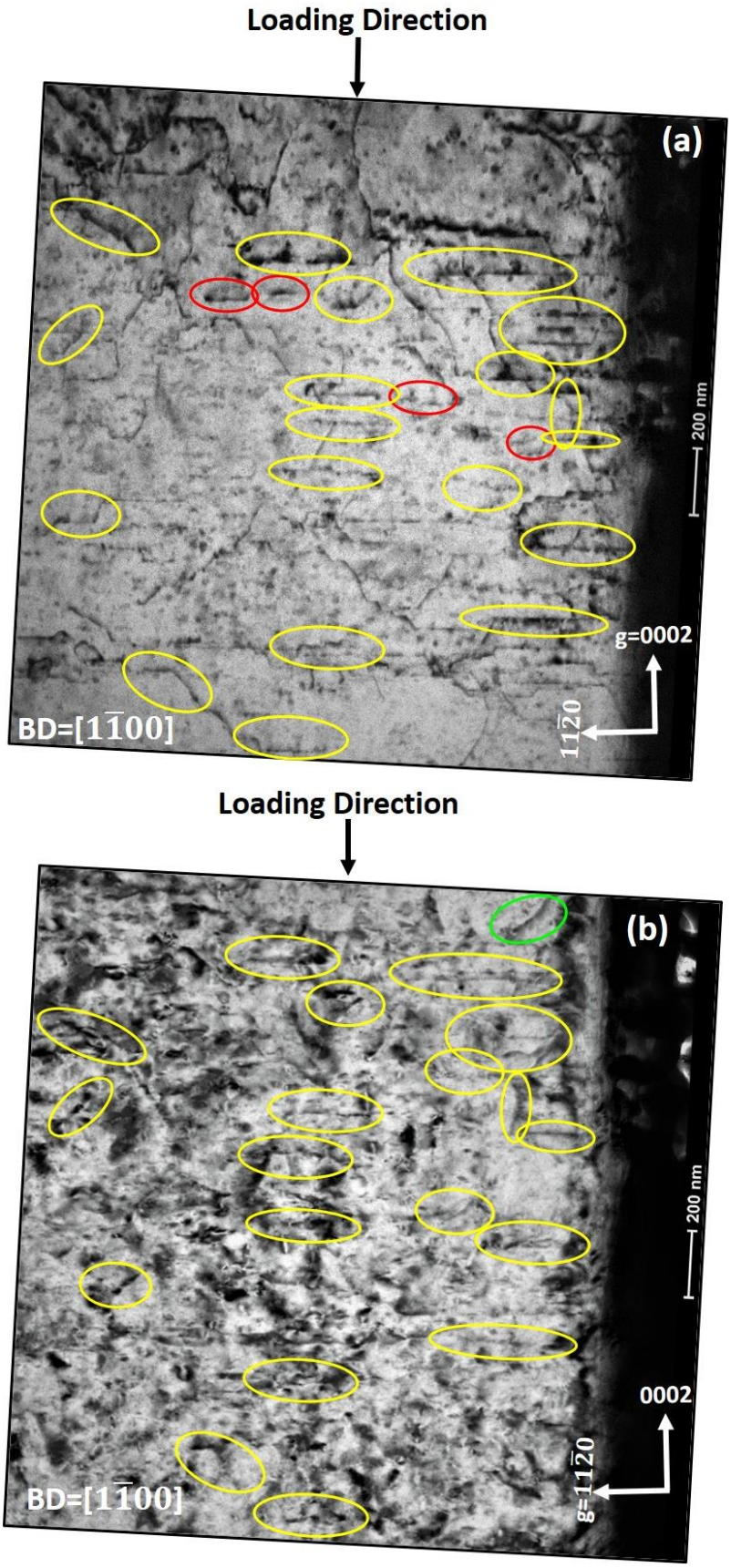
Loading Direction
(a)
200 nm
g=0002
BD=[1$\bar{1}$00]
1$\bar{1}$2$\bar{0}$
Loading Direction
(b)
200 nm
0002
BD=[1$\bar{1}$00]
g=1$\bar{1}$2$\bar{0}$

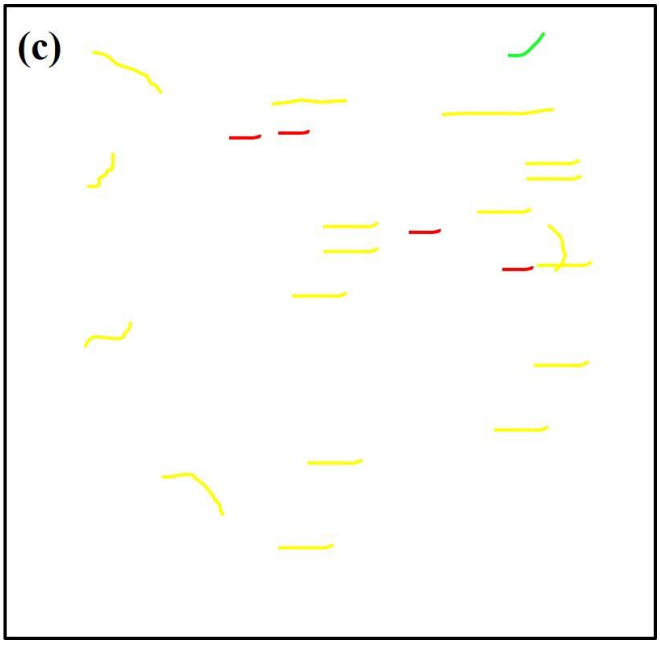

Figure 6.101: BF TEM images of a section of TEM foil taken from a micro-pillar compressed at -90°C to ~3% strain with BD ~ $[1\bar{1}00]$ *using g=0002 (a), and g=*$11\bar{2}0$ *(b). (c) A schematic illustration of the <c+a>, <c> and <a> types of dislocations observed in the TEM specimen. <c+a> dislocations are highlighted in yellow (a-c), <c> dislocations are highlighted in red (a,c) and <a> dislocations are highlighted in green (b,c).*

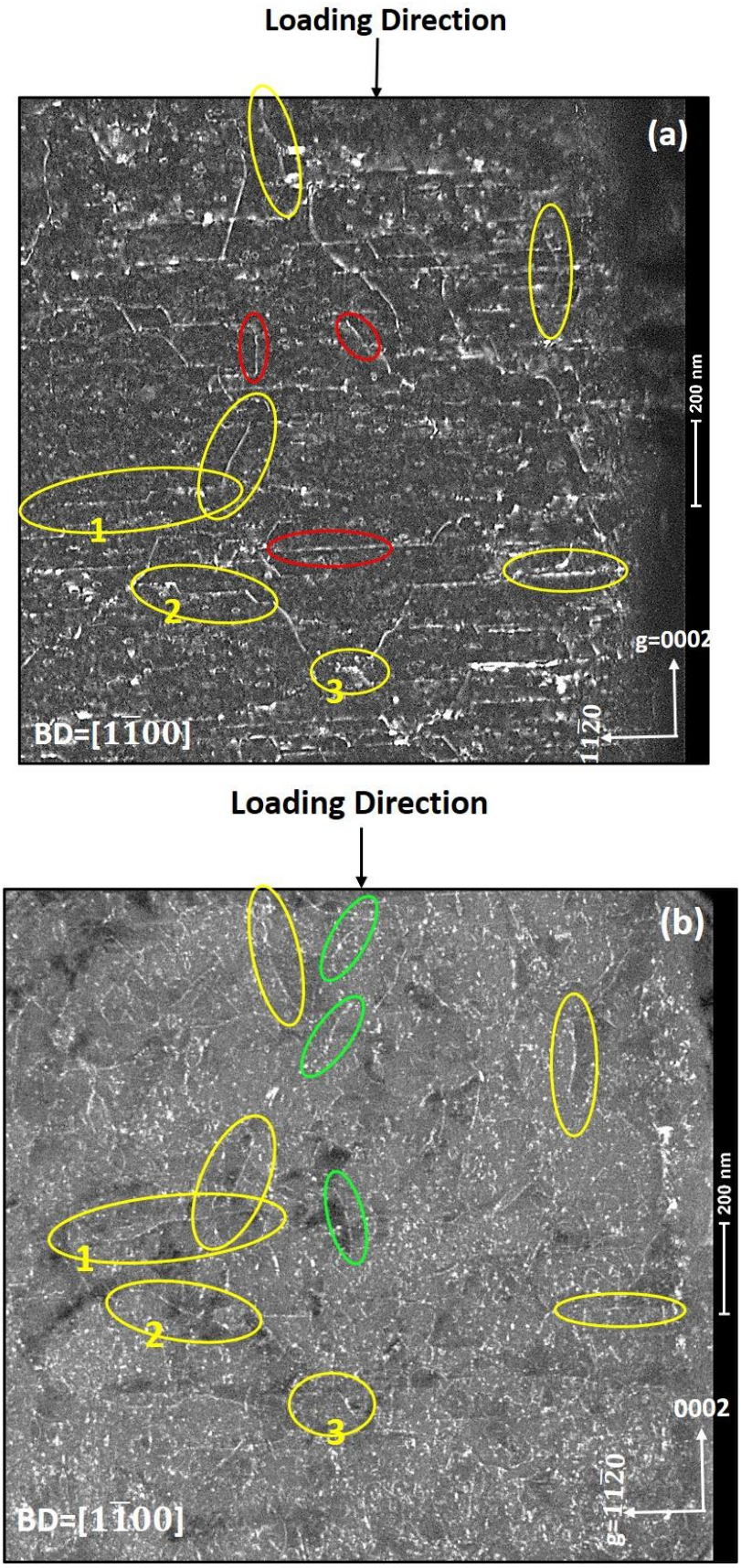
Loading Direction
(a)
200 nm
1
2
3
g=0002
BD=[1$\bar{1}$00]
11$\bar{2}$0
Loading Direction
(b)
200 nm
1
2
3
0002
g=11$\bar{2}$0
BD=[1$\bar{1}$00]

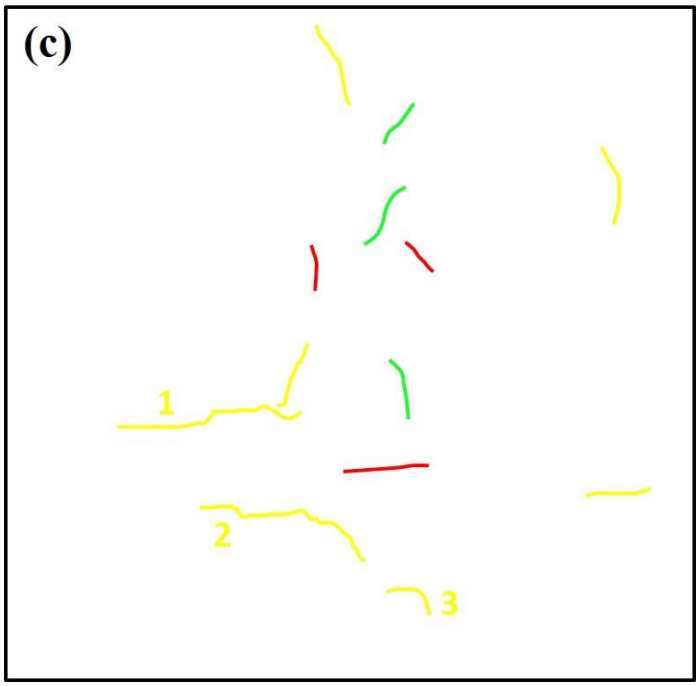

Figure 6.112: WBDF TEM images of a section of TEM foil taken from a micro-pillar compressed at -90°C to ~3% strain with BD ~ $[1\bar{1}00]$ *using g=0002 (a), and g=*$11\bar{2}0$ *(b). (c) A schematic illustration of the <c+a>, <c> and <a>t types of dislocations observed in the TEM specimen. <c+a> dislocations are highlighted in yellow (a-c), <c> dislocations are highlighted in red (a,c), <a> dislocations are highlighted in green (b,c), and yellow numbered <c+a> dislocations have zig-zag morphology (a,c) suggesting cross-slip.*

6.2 Discussion

The results obtained by uniaxial compression of [0001] oriented micro-pillars at the three test temperatures suggest that pyramidal <c+a> slip was the main deformation mode between 23°C to -90°C for this loading direction. The stress-strain behaviour and post-mortem SEM and TEM analysis suggest that the [0001] micro-pillars deformed in a similar fashion irrespective of the test temperature. The main difference lies in the CRSS values for the activation of pyramidal <c+a> slip at different test temperatures. These are found to be different at each test temperature (Table 6.2). Table 6.2 shows that the CRSS values are decreasing with the decrease in temperature between 23°C to -90°C which represents an anomalous temperature dependence in this test temperature range for the pyramidal <c+a> slip. Another important difference lies in the micro-pillar collapse observed in room temperature compressed micro-pillars whereas no such behaviour was observed at cryogenic temperatures. All the micro-pillars compressed at room temperature to about 550-600 MPa collapsed (Pillars 1 and 3 shown in Figure 6.6) whereas cryogenic temperature compressed pillars did not show any such behaviour when compressed to the same stress level (Pillars 4 and 9, compressed at -20°C and -90°C respectively (Figures 6.7 and 6.8)). The flow stress at each test temperature was observed to follow the same trend of CRSS change in temperature as can be seen in Figure 6.13 where flow stress at 5% offset strain is plotted as a function of temperature. In our experiments, it seems reasonable to believe that the preferred glide plane for the <c+a> dislocations activity was second order pyramidal planes $\{11\bar{2}2\}$ keeping in view the Schmid factor criterion and the past literature based on the TEM observations during room temperature compression experiments on magnesium single crystals along the same loading direction of [0001] [15], [44], [50]–[52], [62].

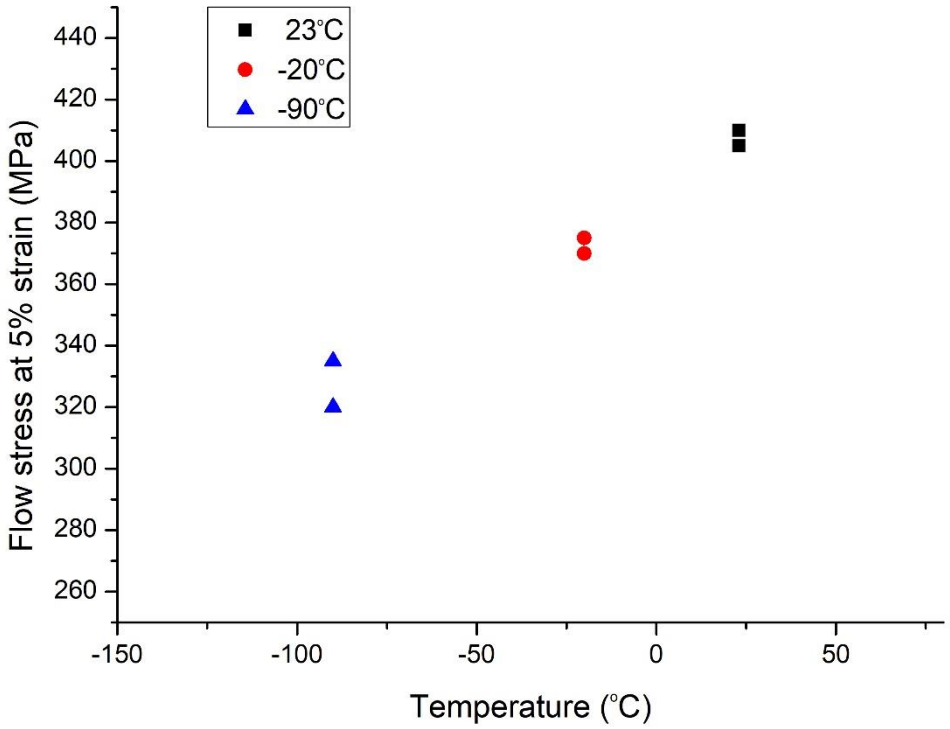

Figure 6.123: Variation of flow stress at 5% strain with test temperature

The room temperature CRSS for pyramidal <c+a> slip recorded in this work is comparable to the other micro-pillar compression studies for the [0001] loading direction. In past literature, the CRSS for pyramidal <c+a> slip is reported for such a loading direction to lie in the range 100-115 MPa [15], [135], [172] for similar sized micro-pillars which is close to our room temperature measured value of 128 ± 7 MPa.

The temperature dependence of CRSS for the activation of pyramidal <c+a> slip in magnesium single crystals has been studied previously by other researchers [28], [44], [52], [62], [94], but there are some conflicting trends in the temperature dependence of CRSS for the pyramidal <c+a> slip within the same temperature range as discussed in Chapter 2 (literature review). One of the possibilities of their contradictory results could be related to the difference in the testing

technique used by these authors as magnesium can show different behaviour in tension and compression along the same loading direction indicating a tension-compression asymmetry while the other reason could be a difference in test-specimen size.

In the context of the scope of this study, the work of Stohr et al. [57] and Kitahara et al. [62] are found more relevant as both these studies were carried out by c-axis compression of magnesium single crystals in the temperature range between -196°C and 197°C. On one side, both these experimental studies reported the anomalous temperature dependence of CRSS of the pyramidal <c+a> slip indicating a decrease in CRSS with the decrease in temperature but they differed in the temperature range for which magnesium single crystals showed such anomalous temperature dependence for this slip system. Kitahara et al. [62] reported this unusual behaviour in the temperature range between -70°C to 20°C whereas Stohr et al. [57] did not report any different temperature dependence for this temperature range (implying an increase in CRSS with the decrease in temperature) and reported an anomalous temperature dependent behaviour between 0°C to 97°C. In this regard, the findings of the present study confirm the observations of Kitahara et al. [62] because our CRSS values for pyramidal <c+a> decrease with decrease in temperature from 128 ± 7 MPa at 23°C to 89 ± 7 MPa at -90°C which is a similar test temperature range to that of Kitahara et al. [62].

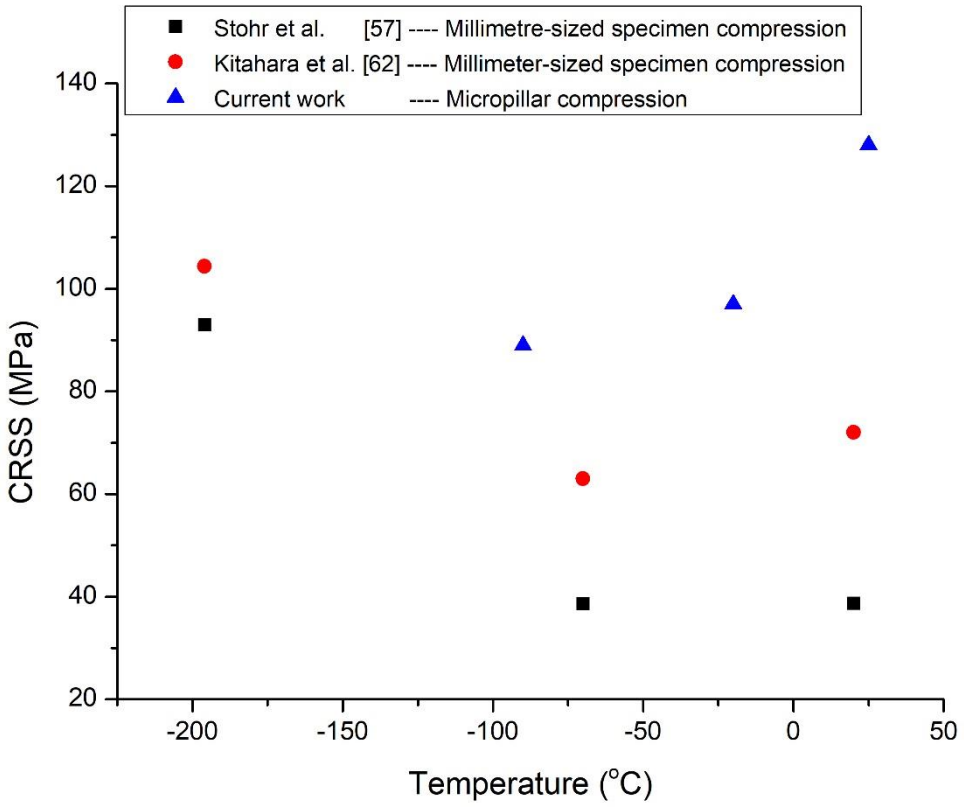

Figure 6.14: Plot of CRSS for pyramidal <c+a> slip as a function of test temperature to compare current work with the literature. The CRSS values from literature are reported by Stohr et al. [57] and Kitahara et al. [62]

The anomalous temperature dependence observed here is not unique for magnesium as it has also been reported for other HCP metals like Cadmium [176]. In this regard, the competition between thermally activated processes of dissociation of sessile <c+a> edge dislocations into energetically stable dislocation products (<a> and <c> type dislocations) and cross slip of <c+a> screw dislocations between pyramidal planes (I and II) are considered to be the main factors for this anomalous temperature dependence of the ease of pyramidal <c+a> slip in some HCP metals [57], [62], [176]. The dissociation of sessile <c+a> edge dislocation has been reported previously based on observations of the presence of junctions between <c>, <c+a> and <a> dislocations or simply the presence of <c> and <c+a> dislocations in deformed specimens

shown by TEM [50], [51]. In the same way, the occurrence of cross-slip during c-axis compression has been reported based on the presence of stair-like <c+a> dislocations structures imaged via TEM [49], [50]. Both these features: <c+a> and <c> dislocations and stair-like /zig-zag <c+a> dislocations were observed in our room temperature and -90°C TEM specimens (Figures 6.9-6.10 and 6.12) indicating that both these thermally activated processes take place not only at room temperature but also at cryogenic temperatures.

As mentioned above, the dissociation of <c+a> is a thermally activated process which is expected to happen more at higher temperatures, resulting in more <c> sessile dislocations. At higher temperature, this increased number of sessile features then acts as a barrier to the incoming glissile screw dislocations, resulting in a decrease in the mean free path of the moving dislocations with the increase in temperature. As a result, higher stresses are needed to continue plastic deformation which is then accommodated by the process of cross slip. So, under the influence of increased stress and high temperature, the chances of cross slip increase and plastic deformation thus proceed with more cross-slip, resulting in a need for a higher CRSS to activate pyramidal <c+a> slip at higher temperatures. This explanation seems reasonable here as well because we have observed both stair-like <c+a> dislocations resulting from cross-slip between pyramidal planes and <c> dislocations originating from the dissociation of sessile <c+a> edge dislocations in our TEM specimens at RT and -90°C as well. From our TEM observations, it seems reasonable to infer that both these thermally activated processes have taken place in our test temperature range. However, it was not possible to ascertain the relative contribution of both of these processes in our experiments due to the different amounts of strain present in our TEM specimens, which is expected to affect the dislocation density of <c+a> dislocations in an exponential increasing manner with the increase in strain during c-axis compression of

magnesium single crystals [50] and hence the amounts of both the key TEM features of <c> dislocations and cross-slip in our case.

The argument mentioned above, it seems reasonable to explain the anomalous temperature dependence of the CRSS of pyramidal <c+a> slip; at the same time, it does not address the possible effects of temperature on the nucleation of individual <c+a> dislocations on the preferred pyramidal plane (I or II) and also on the relative ease of <c+a> dislocations mobility on the competing pyramidal planes. In this regard, computer simulation can be a handy tool to study the temperature effect on both of these key processes [73], [177], [178] as it might not be possible to investigate these aspects of pyramidal <c+a> slip in magnesium with the existing experimental techniques.

Overall, the results of this study confirm the findings of Kitahara et al.[62] regarding the range of temperatures where pyramidal <c+a> slip in magnesium shows anomalous temperature dependence, irrespective of the specimen size. However, it would be more interesting to study the temperature dependence of pyramidal <c+a> slip above room temperature as well, by performing micro-pillar compression experiments at higher temperatures. Moreover, there is still a need to explore the role of temperature on key mechanisms of the activation of pyramidal <c+a> slip, like nucleation of <c+a> dislocations and their preferred glide plane which are currently a point of debate amongst the magnesium research community.

6.3 Summary

In this group of experiments, [0001] oriented micro-pillars were compressed at 23°C, -20°C and -90°C. The stress-strain curves and post-mortem SEM and TEM analysis suggest that pyramidal <c+a> slip remained the main deformation mode over the range of test temperatures. However, the micro-pillars compressed in excess of 550 MPa stress have also shown the

collapse behaviour caused by unstable shearing out of some chunks from the middle of the micro-pillars; the instability in the micro-pillars is likely caused by bending/buckling due to simultaneous activation of <c+a> slip on 6 equivalent pyramidal II planes. The CRSS was measured for the activation of pyramidal <c+a> slip at all the three temperatures and shows an anomalous temperature dependence in the range between 23°C to -90°C involving a decrease in CRSS with the decrease in temperature. The range of temperatures for this unusual temperature dependence of CRSS for pyramidal <c+a> slip observed in this study confirmed the findings of Kitahara et al. [62]. The competition between thermally activated dissociation of sessile <c+a> edge dislocations and the cross-slip of glissile <c+a> screw dislocations between different pyramidal planes is suggested to be responsible for such anomalous temperature dependence of the activation of pyramidal <c+a> slip in magnesium single crystals.

7 Conclusions and future work

7.1 Conclusions

This work investigated the influence of sub ambient temperatures on the activation of basal <a> slip, pyramidal <c+a> slip and tension twinning in micron-sized micro-pillars of magnesium single crystal using in-situ SEM compression. This is the first time that the orientation dependent temperature sensitivity of magnesium has been reported for micron-sized specimens within the sub-ambient temperature range. In this work, a novel cryo-stage has been developed to enable the Hysitron PI85 system to perform in-situ SEM micro-pillar compression experiments below room temperature. The effect of thermal drift due to pillar/punch contact temperature mismatch has been minimized by placing the tip in contact with the cooled specimen and restricting the test duration to a few seconds. The temperature of the cryo-stage is controlled/regulated by the flow of cooling liquid nitrogen gas. This system has been used here to perform variable temperature micro-mechanical testing at sub-ambient temperatures up to -95°C.

The square shaped micro-pillars were made using FIB on three different grains with $[11\bar{2}1]$, [0001] and $[1\bar{3}20]$ orientations to activate basal <a> slip, pyramidal <c+a> slip and tension twinning respectively at 23°C, ~ -25°C and ~ -95°C with similar specimen sizes and strain rates. The CRSS values for these deformation modes were measured / calculated at each test temperature from the stress vs strain curves. The specific conclusions about the temperature dependence of magnesium are:

1. The comparison of variation trends in CRSS values with change in test temperature revealed that each of these deformation modes behaved differently at the micron length scale. Basal <a>

slip showed an increase in CRSS value with a decrease in temperature whereas pyramidal <c+a> slip showed a decrease in CRSS and tension twinning showed no significant change in CRSS with decrease in temperature.

2. For the micro-pillars compressed parallel to the loading direction near $[11\bar{2}1]$, $1/3[11\bar{2}0](0001)$ basal slip remains the main deformation mode for plasticity between 23°C and -94°C. The testing temperature does not significantly affect the dislocation structure over the entire test temperature range. The CRSS for basal <a> slip increases with decrease in temperature, which suggests that it is related to an increase in Peierls lattice friction.

3. For micro-pillars compressed parallel to the c-axis [0001], pyramidal <c+a> slip is the main deformation mode at 23°C, -20°C and -90°C. The CRSS for the activation of pyramidal <c+a> slip decreases with a reduction in temperature, thus showing an anomalous temperature dependence. The findings of this study validate the observations of Kitahara et al. [62] for the sub-ambient test temperature range for which the activation of pyramidal <c+a> slip shows the anomalous temperature dependence.

4. For the micro-pillars compressed along the basal plane, $\{10\bar{1}2\}$ tension twinning followed by basal <a> slip inside the twinned region are the main deformation modes between 23°C and -94°C. The CRSSs for twin nucleation / activation and for twin growth have been successfully measured at all test temperatures by performing pillar compression in load-controlled mode. The CRSSs for twinning show temperature insensitivity over this temperature range. The dominant role of stress concentrators in twin nucleation during micro-pillar compression and the mechanism of twin growth are proposed as the main reason for this. Furthermore, it is concluded that both these key factors for twinning do not change for the temperatures investigated. Lastly, the present work showed clearly that the rate of twin growth is slowed

down with a reduction in testing temperature. This results in smaller twinning associated strain bursts in the stress-strain curves due presumably to the reduced mobility of glissile twinning dislocations.

5. The trends in CRSS values with change in test temperature at the micron scale for basal <a> slip, tension twinning and pyramidal <c+a> slip are similar to those reported previously for the millimetre sized scale, indicating that sample size does not have any impact on the general behaviour / trends of these deformation modes in terms of the temperature dependence. However, the magnified values of CRSS of micron-sized specimens indicate that a significant size-effect does exist. The room temperature CRSS values of micron scale pillars for the three deformation modes are similar to those of other micro-pillar studies, with similar sizes, on magnesium single crystals.

6. This work is the first to report the temperature sensitivity of tension twinning activated by performing uniaxial compression along the basal plane below room temperature at any length scale.

7. The experimental results obtained during this research work provide a useful dataset of CRSS values for basal <a> slip, pyramidal <c+a> slip and tension twinning in pure magnesium at the micron length scale within the practical range of sub-ambient service temperatures (23°C to -95°C) measured systematically under similar test conditions of sample size, uniaxial compression and strain rate.

7.2 Suggestions for future work

To develop the present work, suggestions for future work are:

1. In order to obtain a broader picture of the temperature sensitivity of plastic deformation in magnesium at small length scale over a wider range of service temperatures, it would be of interest to perform micro-pillar compression for the common deformation modes in magnesium above room temperature.

2. It will be of interest to study the micro-pillar behaviour of recently developed magnesium alloys by coupling the effect of test temperature with the alloying elements to optimise the commonly observed plastic anisotropy in magnesium alloys. In this context, the Mg-Y system would provide potential alloys to investigate.

3. Though micro-pillar compression is capable of measuring the critical stresses associated with the activation of particular deformation modes on varying the test temperature, it is not possible to find a direct correlation between the nucleation mechanisms of dislocations and twinning and the test temperature. In this regard, it will be of interest to study the effect of temperature on nucleation mechanisms by crystal plasticity modelling.

References

[1] M. K. Kulekci, “Magnesium and its alloys applications in automotive industry,” *Int. J. Adv. Manuf. Technol.*, vol. 39, no. 9–10, pp. 851–865, 2008.

[2] T. M. Pollock, “Weight loss with magnesium alloys,” *Science.*, vol. 328, no. 5981, pp. 986–987, May 2010.

[3] P. G. Partridge, “The crystallography and deformation modes of hexagonal close-packed metals,” *Rev. Lit. Arts Am.*, vol. 12, pp. 169–194, 1967.

[4] M. D. Uchic, P. A. Shade, and D. M. Dimiduk, “Plasticity of Micrometer-Scale Single Crystals in Compression,” *Annu. Rev. Mater. Res.*, vol. 39, no. 1, pp. 361–386, Aug. 2009.

[5] M. D. Uchic and D. M. Dimiduk, “A Methodology to Investigate Size Scale Effects in Crystalline Plasticity Using Uniaxial Compression Testing,” *Mater. Sci. Eng. A*, vol. 400–401, no. 1-2 SUPPL., pp. 268–278, Jul. 2005.

[6] A. Barnoush, P. Hosemann, J. Molina-Aldareguia, and J. M. Wheeler, “In situ small-scale mechanical testing under extreme environments,” *MRS Bull.*, vol. 44, no. 6, pp. 471–477, Jun. 2019.

[7] C. S. Barrett and T. B. Massalski, *Structure of metals : crystallographic methods, principles, and data*, 3rd Editio. McGraw-Hill Book Company, New York, 1966.

[8] D. Hull and D. J. Bacon, “Dislocations in Other Crystal Structures,” in *Introduction to Dislocations*, Elsevier, 2011, pp. 109–136.

[9] M. H. Yoo, “Slip, twinning, and fracture in hexagonal close-packed metals,” *Metall. Trans. A*, vol. 12, no. 3, pp. 409–418, 1981.

[10] Q. Yu, “Size-related Mechanical Properties of Pure Magnesium,” University of California, Berkeley, 2012.

[11] L. Xiaohui, “Enhanced Ductility of Mg Alloys Containing Rare Earth Elements,” RWTH Aachen University, Germany, 2013.

[12] E. Schmid and B. Walker, *Kristallplastizität: Mit Besonderer Berücksichtigung der Metalle,* 1st ed. Springer, 1935.

[13] P. B. Hirsch and J. S. Lally, “The deformation of magnesium single crystals,” *Philos. Mag.*, vol. 12, no. 117, pp. 595–648, 1965.

[14] B. Sułkowski, R. Chulist, B. Beausir, W. Skrotzki, and B. Mikułowski, “Stage B work-hardening of magnesium single crystals,” *Cryst. Res. Technol.*, vol. 46, no. 5, pp. 439–442, 2011.

[15] G. S. Kim, “Small Volume Investigation of Slip and Twinning in Magnesium Single Crystals,” Universite´ de Grenoble, Grenoble, France, 2011.

[16] K. E. Prasad, K. Rajesh, and U. Ramamurty, “Micropillar and macropillar compression responses of magnesium single crystals oriented for single slip or extension twinning,” *Acta Mater.*, vol. 65, pp. 316–325, Feb. 2014.

[17] J. Ye, R. K. Mishra, A. K. Sachdev, and A. M. Minor, “In situ TEM compression testing of Mg and Mg-0.2 wt.% Ce single crystals,” *Scr. Mater.*, vol. 64, no. 3, pp. 292–295, Feb. 2011.

[18] C. M. Byer and K. T. Ramesh, “Effects of the initial dislocation density on size effects in single-crystal magnesium,” *Acta Mater.*, vol. 61, no. 10, pp. 3808–3818, 2013.

[19] Y. Liu *et al.*, “Experimentally quantifying critical stresses associated with basal slip and twinning in magnesium using micropillars,” *Acta Mater.*, vol. 135, pp. 411–421, Aug. 2017.

[20] E. C. Burke and W. R. Hibbard, “Plastic Deformation of Magnesium Single Crystals,” *J. Miner. Met. Mater. Soc.*, vol. 4, no. 3, pp. 295–303, 1952.

[21] P. M. Burke and O. D. Sherby, “Mechanical Behavior of Crystalline Solids at Elevated Temperature.,” no. April, 1962.

[22] Z. S. Basinski, “The influence of temperature and strain rate on flow stress of magnesium single crystal,” *NASA*, vol. 1, 1959.

[23] H. Conrad and W. D. Robertson, “Effect of temperature on the flow stress and strain-hardening coefficient of magnesium single crystals,” *J. Miner. Met. Mater. Soc.*, vol. 9, no. 4, pp. 503–512, 1957.

[24] J. V. Sharp and J. W. Christian, “Work Hardening and Thermally Activated Flow in Magnesium Single Crystals,” *Phys. Status Solidi*, vol. 11, no. 2, pp. 831–843, 1965.

[25] R. T. C. Tsui, “Internal friction and transmission electron microscopy studies of magnesium-II. Electron microscopy,” *Acta Metall.*, vol. 15, no. 11, pp. 1723–1730, 1967.

[26] B. Bhattacharya and M. Niewczas, “Work-hardening behaviour of Mg single crystals oriented for basal slip,” *Philos. Mag.*, vol. 91, no. 17, pp. 2227–2247, 2011.

[27] F. F. Lavrent'ev, Y. A. Pokhil, and V. I. Startsev, "Critical shear stress temperature and rate dependence in magnesium single crystals," *Strength Mater.*, vol. 4, no. 10, pp. 1216–1220, 1972.

[28] B. Bhattacharya, "Plastic Deformation Behavior of Pure Magnesium in the Temperature Range 4.2K--300K," McMaster University, 2006.

[29] X. L. Nan, H. Y. Wang, L. Zhang, J. B. Li, and Q. C. Jiang, "Calculation of Schmid factors in magnesium: Analysis of deformation behaviors," *Scr. Mater.*, vol. 67, no. 5, pp. 443–446, 2012.

[30] M. D. Uchic, D. M. Dimiduk, J. N. Florando, and W. D. Nix, "Sample dimensions influence strength and crystal plasticity," *Science.*, vol. 305, no. 5686, pp. 986–989, Aug. 2004.

[31] D. M. Dimiduk, M. D. Uchic, and T. A. Parthasarathy, "Size-affected single-slip behavior of pure nickel microcrystals," *Acta Mater.*, vol. 53, no. 15, pp. 4065–4077, Sep. 2005.

[32] R. E. Reed-Hill and W. D. Robertson, "Deformation of magnesium single crystals by nonbasal slip," *J. Miner. Met. Mater. Soc.*, vol. 9, no. 4, pp. 496–502, 1957.

[33] W. B. Hutchinson and M. R. Barnett, "Effective values of critical resolved shear stress for slip in polycrystalline magnesium and other hcp metals," *Scr. Mater.*, vol. 63, no. 7, pp. 737–740, 2010.

[34] S. Ando and H. Tonda, "Non-basal slips in magnesium and magnesium-lithium alloy single crystals," *Mater. Sci. Forum*, vol. 350, pp. 43–48, 2000.

[35] S. Ando, K. Nakamura, K. Takashima, and H. Tonda, “Special issue ‘Magnesium and magnesium alloys’. {1122}<1123> slip in magnesium single crystal.,” *J. Japan Inst. Light Met.*, vol. 42, no. 12, pp. 765–771, 1992.

[36] S. Ando, A. Kodera, K. Fukushima, M. Tsushida, and H. Kitahara, “Tensile Deformation of Magnesium and Magnesium Alloy Single Crystals,” *Mater. Sci. Forum*, vol. 783–786, pp. 341–345, 2014.

[37] S. Ando, M. Tsushida, and H. Kitahara, “Deformation Behavior of Magnesium Single Crystal in c-Axis Compression and a-Axis Tension,” *Mater. Sci. Forum*, vol. 654–656, pp. 699–702, 2010.

[38] J. Jeong, M. Alfreider, R. Konetschnik, D. Kiener, and S. H. Oh, “In-situ TEM observation of {$10\bar{1}2$} twin-dominated deformation of Mg pillars: Twinning mechanism, size effects and rate dependency,” *Acta Mater.*, vol. 158, pp. 407–421, Oct. 2018.

[39] G. D. Sim, K. Y. Xie, K. J. Hemker, and J. A. El-Awady, “Effect of temperature on the transition in deformation modes in Mg single crystals,” *Acta Mater.*, vol. 178, pp. 241–248, Oct. 2019.

[40] G. D. Sim, G. Kim, S. Lavenstein, M. H. Hamza, H. Fan, and J. A. El-Awady, “Anomalous hardening in magnesium driven by a size-dependent transition in deformation modes,” *Acta Mater.*, vol. 144, pp. 11–20, Feb. 2018.

[41] S. Plimpton, “Fast parallel algorithms for short-range molecular dynamics,” *J. Comput. Phys.*, vol. 117, no. 1, pp. 1–19, Mar. 1995.

[42] X. Y. Liu, J. B. Adams, F. Ercolessi, and J. A. Moriarty, “EAM potential for magnesium from quantum mechanical forces,” *Model. Simul. Mater. Sci. Eng.*, vol. 4, no. 3, pp. 293–303, 1996.

[43] J. A. Yasi, T. Nogaret, D. R. Trinkle, Y. Qi, L. G. Hector, and W. A. Curtin, “Basal and prism dislocation cores in magnesium: Comparison of first-principles and embedded-atom-potential methods predictions,” *Model. Simul. Mater. Sci. Eng.*, vol. 17, no. 5, 2009.

[44] T. Obara, H. Yoshinga, and S. Morozumi, “{11$\bar{2}$2}〈1123〉 Slip system in magnesium,” *Acta Metall.*, vol. 21, no. 7, pp. 845–853, 1973.

[45] S. Ando, N. Harada, M. Tsushida, H. Kitahara, and H. Tonda, “Temperature Dependence of Deformation Behavior in Magnesium and Magnesium Alloy Single Crystals,” *Key Eng. Mater.*, vol. 345–346, pp. 101–104, 2007.

[46] S. Ando, M. Tanaka, and H. Tonda, “Pyramidal slip in magnesium alloy single crystals,” in *Materials Science Forum*, 2003, vol. 419–422, no. I, pp. 87–92.

[47] H. Tonda and S. Ando, “Effect of temperature and shear direction on yield stress by {11$\bar{2}$2}〈1123〉 slip in HCP metals,” in *Metallurgical and Materials Transactions A: Physical Metallurgy and Materials Science*, 2002, vol. 33, no. 3, pp. 831–836.

[48] D. Zhang *et al.*, “ In situ transmission electron microscopy investigation on 〈 c + a 〉 slip in Mg ,” *J. Mater. Res.*, vol. 34, no. 9, pp. 1–10, May 2019.

[49] J. Jain, P. Cizek, and K. Hariharan, “Transmission electron microscopy investigation on dislocation bands in pure Mg,” *Scr. Mater.*, vol. 130, pp. 133–137, Mar. 2017.

[50] J. Geng, M. F. Chisholm, R. K. Mishra, and K. S. Kumar, “An electron microscopy study of dislocation structures in Mg single crystals compressed along [0 0 0 1] at room temperature,” *Philos. Mag.*, vol. 95, no. 35, pp. 3910–3932, Dec. 2015.

[51] S. R. Agnew, J. a. Horton, and M. H. Yoo, “Transmission electron microscopy investigation of <c+a> dislocations in Mg and α-solid solution Mg-Li alloys,” *Metall. Mater. Trans. A*, vol. 33, no. 13, pp. 851–858, 2002.

[52] J. F. Stohr, J. P. Poirier, P. J. F. Stohr, and J. P. Poirier, “Etude en microscopie electronique du glissement pyramidal {1122} 〈1123〉 dans le magnesium,” *Philos. Mag.*, vol. 25, no. 6, pp. 1313–1329, 1972.

[53] K. Y. Xie, Z. Alam, A. Caffee, and K. J. Hemker, “Pyramidal i slip in c-axis compressed Mg single crystals,” *Scr. Mater.*, vol. 112, pp. 75–78, 2016.

[54] K. Y. Xie, Z. Alam, A. Caffee, and K. J. Hemker, “Deformation behavior of Mg single crystals compressed along c-axis,” in *Magnesium Technology*, 2016, vol. 2016-January, pp. 209–211.

[55] B. Y. Liu *et al.*, “Large plasticity in magnesium mediated by pyramidal dislocations,” *Science.*, vol. 364, no. 6448, pp. 73–75, 2019.

[56] C. M. Byer, B. Li, B. Cao, and K. T. Ramesh, “Microcompression of single-crystal magnesium,” *Scr. Mater.*, vol. 62, no. 8, pp. 536–539, 2010.

[57] P. J. F. Stohr and J. P. Poirier, “Etude en microscopie electronique du glissement pyramidal {1122} 〈1123〉 dans le magnesium,” *Philos. Mag.*, vol. 25, no. 6, pp. 1313–1329, 1972.

[58] E. Lilleodden, “Microcompression study of Mg (0 0 0 1) single crystal,” *Scr. Mater.*, vol. 62, no. 8, pp. 532–535, 2010.

[59] B. C. Wonsiewicz, “PLASTICITY OF MAGNESIUM CRYSTALS,” Massachusetts Institute of Technology, USA, 1966.

[60] E. W. Kelley and W. F. Hosford, “The plastic deformation of magnesium : technical report,” 1967.

[61] H. Yoshinaga and R. Horiuchi, “Deformation mechanisms in magnesium single crystals compressed in the direction parallel to hexagonal axis,” *Trans. JIM*, vol. 4, no. 1, pp. 1–8, 1963.

[62] T. Kitahara, S. Ando, M. Tsushida, H. Kitahara, and H. Tonda, “Deformation Behavior of Magnesium Single Crystals in C-Axis Compression,” *Key Eng. Mater.*, vol. 345–346, pp. 129–132, 2007.

[63] M. H. Yoo, S. R. Agnew, J. R. Morris, and K. M. Ho, “Non-basal slip systems in HCP metals and alloys: Source mechanisms,” *Mater. Sci. Eng. A*, vol. 319–321, pp. 87–92, 2001.

[64] S. Sandlöbes *et al.*, “The relation between ductility and stacking fault energies in Mg and Mg-Y alloys,” *Acta Mater.*, vol. 60, no. 6–7, pp. 3011–3021, Apr. 2012.

[65] S. R. Agnew, L. Capolungo, and C. A. Calhoun, “Connections between the basal I1 ‘growth’ fault and 〈c + a〉 dislocations,” *Acta Mater.*, vol. 82, pp. 255–265, Jan. 2015.

[66] S. Sandlöbes, M. Friák, J. Neugebauer, and D. Raabe, “Basal and non-basal dislocation slip in Mg–Y,” *Mater. Sci. Eng. A*, vol. 576, pp. 61–68, Aug. 2013.

[67] D. Buey and M. Ghazisaeidi, “Atomistic simulation of <c + a> screw dislocation cross-slip in Mg,” *Scr. Mater.*, vol. 117, pp. 51–54, May 2016.

[68] M. Itakura, H. Kaburaki, M. Yamaguchi, and T. Tsuru, “Novel Cross-Slip Mechanism of Pyramidal Screw Dislocations in Magnesium,” *Phys. Rev. Lett.*, vol. 116, no. 22, Jun. 2016.

[69] Z. Wu and W. A. Curtin, “Mechanism and energetics of ‘c + a’ dislocation cross-slip in hcp metals,” *Proc. Natl. Acad. Sci. U. S. A.*, vol. 113, no. 40, pp. 11137–11142, Oct. 2016.

[70] Y. Tang and J. A. El-Awady, “Formation and slip of pyramidal dislocations in hexagonal close-packed magnesium single crystals,” *Acta Mater.*, vol. 71, pp. 319–332, 2014.

[71] D. Y. Sun *et al.*, “Crystal-melt interfacial free energies in hcp metals: A molecular dynamics study of Mg,” *Phys. Rev. B - Condens. Matter Mater. Phys.*, vol. 73, no. 2, 2006.

[72] H. Fan and J. A. El-Awady, “Towards resolving the anonymity of pyramidal slip in magnesium,” *Mater. Sci. Eng. A*, vol. 644, pp. 318–324, 2015.

[73] H. Fan, Q. Wang, X. Tian, and J. A. El-Awady, “Temperature effects on the mobility of pyramidal < c + a > dislocations in magnesium,” *Scr. Mater.*, vol. 127, pp. 68–71, 2017.

[74] Z. Wu and W. A. Curtin, “Intrinsic structural transitions of the pyramidal i <c + a> dislocation in magnesium,” *Scr. Mater.*, vol. 116, pp. 104–107, 2016.

[75] F. C. Frank and J. F. Nicholas, “CXXVIII. Stable dislocations in the common crystal lattices,” *London, Edinburgh, Dublin Philos. Mag. J. Sci.*, vol. 44, no. 358, pp. 1213–

1235, Nov. 1953.

[76] "The theory of the crystallography of deformation twinning," in *Proceedings of the Royal Society of London. Series A. Mathematical and Physical Sciences*, 1965, vol. 288, no. 1413, pp. 240–255.

[77] S. Mahajan and D. F. Williams, "Deformation Twinning in Metals and Alloys," *Int. Metall. Rev.*, vol. 18, no. 2, pp. 43–61, 1973.

[78] W. F. Hosford, *The Mechanics of Crystals and Textured Polycrystals (Oxford Engineering Science Series)*. Oxford University Press, USA, 1993.

[79] R. E. Reed-Hill and W. D. Robertson, "The crystallographic characteristics of fracture in magnesium single crystals," *Acta Metall.*, vol. 5, no. 12, pp. 728–737, 1957.

[80] M. R. Barnett, "Twinning and the ductility of magnesium alloys. Part I: 'Tension' twins," *Mater. Sci. Eng. A*, vol. 464, no. 1–2, pp. 1–7, 2007.

[81] M. R. Barnett, "Twinning and the ductility of magnesium alloys. Part II. 'Contraction' twins," *Mater. Sci. Eng. A*, vol. 464, no. 1–2, pp. 8–16, 2007.

[82] P. Lukáč and Z. Trojanová, "Hardening and softening in selected magnesium alloys," *Mater. Sci. Eng. A*, vol. 462, no. 1–2, pp. 23–28, Jul. 2007.

[83] M. R. Barnett, Z. Keshavarz, A. G. Beer, and D. Atwell, "Influence of grain size on the compressive deformation of wrought Mg-3Al-1Zn," *Acta Mater.*, vol. 52, no. 17, pp. 5093–5103, 2004.

[84] M. R. Barnett, M. D. Nave, and C. J. Bettles, "Deformation microstructures and textures

of some cold rolled Mg alloys," *Mater. Sci. Eng. A*, vol. 386, no. 1–2, pp. 205–211, 2004.

[85] P. Yang, Y. Yu, L. Chen, and W. Mao, "Experimental determination and theoretical prediction of twin orientations in magnesium alloy AZ31," *Scr. Mater.*, vol. 50, no. 8, pp. 1163–1168, 2004.

[86] F. Hiura, "LATENT HARDENING IN PURE MAGNESIUM SINGLE CRYSTALS," McMaster University, Canada, 2010.

[87] J. Wang, I. J. Beyerlein, and C. N. Tomé, "An atomic and probabilistic perspective on twin nucleation in Mg," *Scr. Mater.*, vol. 63, no. 7, pp. 741–746, 2010.

[88] X. Liao, J. Wang, J. Nie, Y. Jiang, and P. Wu, "Deformation twinning in hexagonal materials," *MRS Bull.*, vol. 41, no. 4, pp. 314–319, Apr. 2016.

[89] G. S. Kim, S. Yi, Y. Huang, and E. Lilleodden, "Twining and slip activity in magnesium <ll-20> single crystal," in *Materials Research Society Symposium Proceedings*, 2010, vol. 1224, pp. 181–186.

[90] Q. Yu, L. Qi, K. Chen, R. K. Mishra, J. Li, and A. M. Minor, "The nanostructured origin of deformation twinning," *Nano Lett.*, vol. 12, no. 2, pp. 887–892, Feb. 2012.

[91] A. Luque, M. Ghazisaeidi, and W. A. Curtin, "Deformation modes in magnesium (0 0 0 1) and (011-1) single crystals: Simulations versus experiments," *Model. Simul. Mater. Sci. Eng.*, vol. 21, no. 4, Jun. 2013.

[92] A. Chapuis, "Low temperature plane strain compression of a magnesium single crystal with c-axis constrained," *Mater. Sci. Eng. A*, vol. 590, pp. 401–405, 2014.

[93] A. Chapuis and Ju. Driver, “a Fundamental Study of the High Temperature Deformation Mechanism of Magnesium,” *J. Phys. Conf. Ser.*, vol. 240, p. 012092, 2010.

[94] A. Chapuis and J. H. Driver, “Temperature dependency of slip and twinning in plane strain compressed magnesium single crystals,” *Acta Mater.*, vol. 59, no. 5, pp. 1986–1994, 2011.

[95] H. Yoshinaga and R. Horiuchi, “On the Nonbasal Slip in Magnesium Crystals,” *Trans. Japan Inst. Met.*, vol. 5, no. 1, pp. 14–21, 1964.

[96] B. Syed, J. Geng, R. K. Mishra, and K. S. Kumar, “[0 0 0 1] Compression response at room temperature of single-crystal magnesium,” *Scr. Mater.*, vol. 67, no. 7–8, pp. 700–703, 2012.

[97] A. Kunz, S. Pathak, and J. R. Greer, “Size effects in Al nanopillars: Single crystalline vs. bicrystalline,” *Acta Mater.*, vol. 59, no. 11, pp. 4416–4424, Jun. 2011.

[98] O. Kraft *et al.*, “Size effects on deformation and fatigue of thin films and small structures: experiments and dislocation dynamics simulation,” 2006.

[99] R. Gu and A. H. W. Ngan, “Dislocation arrangement in small crystal volumes determines power-law size dependence of yield strength,” *J. Mech. Phys. Solids*, vol. 61, no. 6, pp. 1531–1542, Jun. 2013.

[100] C. P. Frick, B. G. Clark, S. Orso, A. S. Schneider, and E. Arzt, “Size effect on strength and strain hardening of small-scale [1 1 1] nickel compression pillars,” *Mater. Sci. Eng. A*, vol. 489, no. 1–2, pp. 319–329, Aug. 2008.

[101] J. R. Greer and W. D. Nix, “Nanoscale gold pillars strengthened through dislocation

starvation," *Phys. Rev. B - Condens. Matter Mater. Phys.*, vol. 73, no. 24, p. 245410, Jun. 2006.

[102] S. W. Lee, S. M. Han, and W. D. Nix, "Uniaxial compression of fcc Au nanopillars on an MgO substrate: The effects of prestraining and annealing," *Acta Mater.*, vol. 57, no. 15, pp. 4404–4415, Sep. 2009.

[103] K. O and C. A. Volkert, "Size Effects on Deformation and Fatigue of Thin Films and Small Structures," *CAMTEC, Cambridge Univ. UK, Cambridge*, 2006.

[104] A. T. Jennings, J. Li, and J. R. Greer, "Emergence of strain-rate sensitivity in Cu nanopillars: Transition from dislocation multiplication to dislocation nucleation," *Acta Mater.*, vol. 59, no. 14, pp. 5627–5637, Aug. 2011.

[105] K. S. Ng and A. H. W. Ngan, "Stochastic nature of plasticity of aluminum micro-pillars," *Acta Mater.*, vol. 56, no. 8, pp. 1712–1720, May 2008.

[106] B. R. S. Rogne and C. Thaulow, "Strengthening mechanisms of iron micropillars," *Philos. Mag.*, vol. 95, no. 16–18, pp. 1814–1828, Jun. 2015.

[107] R. Huang *et al.*, "Flow stress in submicron BCC iron single crystals: Sample-size-dependent strain-rate sensitivity and rate-dependent size strengthening," *Mater. Res. Lett.*, vol. 3, no. 3, pp. 121–127, Jan. 2015.

[108] H. Yilmaz, "Mechanical Properties of Body-Centred Cubic Nanopillars," *[Thesis]. Manchester, UK Univ. Manchester; 2018.*, May 2018.

[109] A. S. Schneider *et al.*, "Correlation between critical temperature and strength of small-scale bcc pillars," *Phys. Rev. Lett.*, vol. 103, no. 10, Aug. 2009.

[110] J. Y. Kim, D. Jang, and J. R. Greer, “Tensile and compressive behavior of tungsten, molybdenum, tantalum and niobium at the nanoscale,” *Acta Mater.*, vol. 58, no. 7, pp. 2355–2363, Apr. 2010.

[111] S. M. Han, T. Bozorg-Grayeli, J. R. Groves, and W. D. Nix, “Size effects on strength and plasticity of vanadium nanopillars,” *Scr. Mater.*, vol. 63, no. 12, pp. 1153–1156, Dec. 2010.

[112] Q. Yu *et al.*, “Strong crystal size effect on deformation twinning,” *Nature*, vol. 463, no. 7279, pp. 335–338, Jan. 2010.

[113] Q. Sun, Q. Guo, X. Yao, L. Xiao, J. R. Greer, and J. Sun, “Size effects in strength and plasticity of single-crystalline titanium micropillars with prismatic slip orientation,” *Scr. Mater.*, vol. 65, no. 6, pp. 473–476, 2011.

[114] J. R. Greer, W. C. Oliver, and W. D. Nix, “Size dependence of mechanical properties of gold at the micron scale in the absence of strain gradients,” *Acta Mater.*, vol. 53, no. 6, pp. 1821–1830, Apr. 2005.

[115] C. A. Volkert and E. T. Lilleodden, “Size effects in the deformation of sub-micron Au columns,” *Philos. Mag.*, vol. 86, no. 33-35 SPEC. ISSUE, pp. 5567–5579, 2006.

[116] D. Kiener, C. Motz, T. Schobert, M. Jenko, and G. Dehm, “Determination of mechanical properties of copper at the micron scale,” *Adv. Eng. Mater.*, vol. 8, no. 11, pp. 1119–1125, 2006.

[117] D. Kiener and A. M. Minor, “Source-controlled yield and hardening of Cu(1 0 0) studied by in situ transmission electron microscopy,” *Acta Mater.*, vol. 59, no. 4, pp. 1328–1337,

Feb. 2011.

[118] Shahbeyk, Voyiadjis, Habibi, Astaneh, and Yaghoobi, “Review of Size Effects during Micropillar Compression Test: Experiments and Atomistic Simulations,” *Crystals*, vol. 9, no. 11, p. 591, Nov. 2019.

[119] T. A. Parthasarathy, S. I. Rao, D. M. Dimiduk, M. D. Uchic, and D. R. Trinkle, “Contribution to size effect of yield strength from the stochastics of dislocation source lengths in finite samples,” *Scr. Mater.*, vol. 56, no. 4, pp. 313–316, Feb. 2007.

[120] T. S. Jun, Z. Zhang, G. Sernicola, F. P. E. Dunne, and T. B. Britton, “Local strain rate sensitivity of single α phase within a dual-phase Ti alloy,” *Acta Mater.*, vol. 107, pp. 298–309, Apr. 2016.

[121] Z. Zhang, T. S. Jun, T. B. Britton, and F. P. E. Dunne, “Intrinsic anisotropy of strain rate sensitivity in single crystal alpha titanium,” *Acta Mater.*, vol. 118, pp. 317–330, Oct. 2016.

[122] T. S. Jun, G. Sernicola, F. P. E. Dunne, and T. B. Britton, “Local deformation mechanisms of two-phase Ti alloy,” *Mater. Sci. Eng. A*, vol. 649, pp. 39–47, 2016.

[123] T. S. Jun *et al.*, “The role of β-titanium ligaments in the deformation of dual phase titanium alloys,” *Mater. Sci. Eng. A*, vol. 746, pp. 394–405, Feb. 2019.

[124] Z. Zheng, S. Waheed, D. S. Balint, and F. P. E. Dunne, “Slip transfer across phase boundaries in dual phase titanium alloys and the effect on strain rate sensitivity,” *Int. J. Plast.*, vol. 104, pp. 23–38, May 2018.

[125] K. Kishida, J. G. Kim, T. Nagae, and H. Inui, “Experimental evaluation of critical

resolved shear stress for the first-order pyramidal c + a slip in commercially pure Ti by micropillar compression method," *Acta Mater.*, vol. 196, pp. 168–174, Sep. 2020.

[126] K. Onose *et al.*, "Analysis of deformation behavior in beta titanium alloys using TEM in-situ observation," *Keikinzoku/Journal Japan Inst. Light Met.*, vol. 69, no. 5, pp. 273–280, 2019.

[127] T. E. J. Edwards, F. Di Gioacchino, G. Mohanty, J. Wehrs, J. Michler, and W. J. Clegg, "Longitudinal twinning in a TiAl alloy at high temperature by in situ microcompression," *Acta Mater.*, vol. 148, pp. 202–215, Apr. 2018.

[128] J. Y. Wang *et al.*, "Effect of solute content and temperature on the deformation mechanisms and critical resolved shear stress in Mg-Al and Mg-Zn alloys," *Acta Mater.*, vol. 170, pp. 155–165, May 2019.

[129] Q. Sun, Q. Guo, X. Yao, L. Xiao, J. R. Greer, and J. Sun, "Size effects in strength and plasticity of single-crystalline titanium micropillars with prismatic slip orientation," *Scr. Mater.*, vol. 65, no. 6, pp. 473–476, Sep. 2011.

[130] W. Chen *et al.*, "Strain rate-induced plasticity in bcc β-Ti alloy single crystal micropillars containing brittle ω-precipitates," *Mater. Des.*, vol. 137, pp. 404–413, Jan. 2018.

[131] A. J. Palomares-García, I. Sabirov, M. T. Pérez-Prado, and J. M. Molina-Aldareguia, "Effect of nanoscale thick lamellae on the micromechanical response of a TiAl alloy," *Scr. Mater.*, vol. 139, pp. 17–21, Oct. 2017.

[132] P. J. Ashton *et al.*, "The effect of the beta phase on the micromechanical response of dual-phase titanium alloys," *Int. J. Fatigue*, vol. 100, pp. 377–387, Jul. 2017.

[133] A. J. Palomares-García, M. T. Pérez-Prado, and J. M. Molina-Aldareguia, “Effect of lamellar orientation on the strength and operating deformation mechanisms of fully lamellar TiAl alloys determined by micropillar compression,” *Acta Mater.*, vol. 123, pp. 102–114, Jan. 2017.

[134] T. E. J. Edwards *et al.*, “Transverse deformation of a lamellar TiAl alloy at high temperature by in situ microcompression,” *Acta Mater.*, vol. 166, pp. 85–99, Mar. 2019.

[135] X. Ma, Q. Jiao, L. J. Kecskes, J. A. El-Awady, and T. P. Weihs, “Effect of basal precipitates on extension twinning and pyramidal slip: A micro-mechanical and electron microscopy study of a Mg–Al binary alloy,” *Acta Mater.*, vol. 189, pp. 35–46, May 2020.

[136] J. Y. Wang *et al.*, “Effect of solute content and temperature on the deformation mechanisms and critical resolved shear stress in Mg-Al and Mg-Zn alloys,” *Acta Mater.*, vol. 170, no. March 2019, pp. 155–165, 2019.

[137] G. Mohanty *et al.*, “Elevated temperature, strain rate jump microcompression of nanocrystalline nickel,” *Philos. Mag.*, vol. 95, no. 16–18, pp. 1878–1895, 2015.

[138] J. M. Wheeler, C. Kirchlechner, J. S. Micha, J. Michler, and D. Kiener, “The effect of size on the strength of FCC metals at elevated temperatures: annealed copper,” *Philos. Mag.*, vol. 96, no. 32–34, pp. 3379–3395, 2016.

[139] J. Ast *et al.*, “The brittle-ductile transition of tungsten single crystals at the micro-scale,” *Mater. Des.*, vol. 152, pp. 168–180, 2018.

[140] O. Torrents Abad, J. M. Wheeler, J. Michler, A. S. Schneider, and E. Arzt, “Temperature-dependent size effects on the strength of Ta and W micropillars,” *Acta Mater.*, vol. 103,

pp. 483–494, Jan. 2016.

[141] S. W. Lee, Y. Cheng, I. Ryu, and J. R. Greer, “Cold-temperature deformation of nano-sized tungsten and niobium as revealed by in-situ nano-mechanical experiments,” *Sci. China Technol. Sci.*, vol. 57, no. 4, pp. 652–662, Apr. 2014.

[142] H. Yilmaz, C. J. Williams, J. Risan, and B. Derby, “The size dependent strength of Fe, Nb and V micropillars at room and low temperature,” *Materialia*, vol. 7, no. April, 2019.

[143] A. B. Hagen, B. D. Snartland, and C. Thaulow, “Temperature and orientation effects on the deformation mechanisms of α-Fe micropillars,” *Acta Mater.*, vol. 129, pp. 398–407, May 2017.

[144] A. B. Hagen and C. Thaulow, “Low temperature in-situ micro-compression testing of iron pillars,” *Mater. Sci. Eng. A*, vol. 678, pp. 355–364, Dec. 2016.

[145] C. R. Mayer, S. Lotfian, J. Molina-Aldareguia, and N. Chawla, “High-Temperature Micropillar Compression Creep Testing of Constituent Phases in Lead-Free Solder,” *Adv. Eng. Mater.*, vol. 17, no. 8, pp. 1168–1174, 2015.

[146] A. Lupinacci, J. Kacher, A. Eilenberg, A. A. Shapiro, P. Hosemann, and A. M. Minor, “Cryogenic in situ microcompression testing of Sn,” *Acta Mater.*, vol. 78, pp. 56–64, 2014.

[147] J. Cho *et al.*, “High temperature deformability of ductile flash-sintered ceramics via in-situ compression,” *Nat. Commun.*, vol. 9, no. 1, pp. 1–9, 2018.

[148] S. Korte and W. J. Clegg, “Micropillar compression of ceramics at elevated temperatures,” *Scr. Mater.*, vol. 60, no. 9, pp. 807–810, 2009.

[149] J. M. Wheeler, R. Raghavan, V. Chawla, J. Zechner, I. Utke, and J. Michler, “Failure mechanisms in metal-metal nanolaminates at elevated temperatures: Microcompression of Cu-W multilayers,” *Scr. Mater.*, vol. 98, pp. 28–31, 2015.

[150] S. Lotfian, M. Rodríguez, K. E. Yazzie, N. Chawla, J. Llorca, and J. M. Molina-Aldareguía, “High temperature micropillar compression of Al/SiC nanolaminates,” *Acta Mater.*, vol. 61, no. 12, pp. 4439–4451, 2013.

[151] K. Thomas *et al.*, “Elevated and cryogenic temperature micropillar compression of magnesium–niobium multilayer films,” *J. Mater. Sci.*, 2019.

[152] J. M. Wheeler, D. E. J. Armstrong, W. Heinz, and R. Schwaiger, “High temperature nanoindentation: The state of the art and future challenges,” *Curr. Opin. Solid State Mater. Sci.*, vol. 19, no. 6, pp. 354–366, 2015.

[153] J. Chen, G. A. Bell, H. Dong, J. F. Smith, and B. D. Beake, “A study of low temperature mechanical properties and creep behaviour of polypropylene using a new sub-ambient temperature nanoindentation test platform,” *J. Phys. D. Appl. Phys.*, vol. 43, no. 42, 2010.

[154] J. M. Wheeler and J. Michler, “Elevated temperature, nano-mechanical testing in situ in the scanning electron microscope,” *Rev. Sci. Instrum.*, vol. 84, no. 4, p. 045103, Apr. 2013.

[155] M. A. Monclús and J. M. Molina-Aldareguia, “High Temperature Nanomechanical Testing,” in *Handbook of Mechanics of Materials*, Springer Singapore, 2018, pp. 1–29.

[156] S. Wang and H. Zhao, “Low temperature nanoindentation: Development and

applications," *Micromachines*, vol. 11, no. 4, 2020.

[157] A. J. Harris, B. D. Beake, & D. E. J. Armstrong, and M. I. Davies, "Development of High Temperature Nanoindentation Methodology and its Application in the Nanoindentation of Polycrystalline Tungsten in Vacuum to 950 °C."

[158] E. W. Kelley and W. F. Hosford, "Plane-Strain Compression of Magnesium and Magnesium Alloy Crystals," *Trans. Metall. Soc. AIME*, vol. 242, no. 1, pp. 5–13, 1968.

[159] A. S. Schneider, B. G. Clark, C. P. Frick, P. A. Gruber, and E. Arzt, "Effect of orientation and loading rate on compression behavior of small-scale Mo pillars," *Mater. Sci. Eng. A*, vol. 508, no. 1–2, pp. 241–246, 2009.

[160] M. Zaiser *et al.*, "Strain bursts in plastically deforming molybdenum micro- and nanopillars," *Philos. Mag.*, vol. 88, no. 30–32, pp. 3861–3874, 2008.

[161] H. Tang, K. W. Schwarz, and H. D. Espinosa, "Dislocation-source shutdown and the plastic behavior of single-crystal micropillars," *Phys. Rev. Lett.*, vol. 100, no. 18, p. 185503, May 2008.

[162] M. Uranagase and R. Matsumoto, "Thermal activation analysis of enthalpic and entropic contributions to the activation free energy of basal and prismatic slips in Mg," *Phys. Rev. B - Condens. Matter Mater. Phys.*, vol. 89, no. 22, pp. 1–7, 2014.

[163] M. Uranagase, S. Kamigaki, R. Matsumoto, and N. Miyazaki, "Activation free energy of nucleation of a dislocation pair in magnesium," *Mater. Trans.*, vol. 54, no. 5, pp. 680–685, 2013.

[164] S. Groh, E. B. Marin, M. F. Horstemeyer, and D. J. Bammann, "Dislocation motion in

magnesium: A study by molecular statics and molecular dynamics," *Model. Simul. Mater. Sci. Eng.*, vol. 17, no. 7, 2009.

[165] A. S. Schneider, C. P. Frick, E. Arzt, W. J. Clegg, and S. Korte, "Influence of test temperature on the size effect in molybdenum small-scale compression pillars," *Philos. Mag. Lett.*, vol. 93, no. 6, pp. 331–338, Jun. 2013.

[166] S. R. Niezgoda, A. K. Kanjarla, I. J. Beyerlein, and C. N. Tomé, "Stochastic modeling of twin nucleation in polycrystals: An application in hexagonal close-packed metals," *Int. J. Plast.*, vol. 56, pp. 119–138, May 2014.

[167] I. J. Beyerlein, L. Capolungo, P. E. Marshall, R. J. McCabe, and C. N. Tome, "Statistical analyses of deformation twinning in magnesium," *Philos. Mag.*, vol. 90, no. 16, pp. 2161–2190, May 2010.

[168] J. Wang, S. K. Yadav, J. P. Hirth, C. N. Tomé, and I. J. Beyerlein, "Pure-Shuffle Nucleation of Deformation Twins in Hexagonal-Close-Packed Metals," *Mater. Res. Lett.*, vol. 1, no. 3, pp. 126–132, Sep. 2013.

[169] J. S. Weaver *et al.*, "Slip transmission of high angle grain boundaries in body-centered cubic metals: Micropillar compression of pure Ta single and bi-crystals," *Acta Mater.*, vol. 156, pp. 356–368, 2018.

[170] C. D. Barrett, M. A. Tschopp, H. El Kadiri, and B. Li, "Influence of crystallographic orientation on twin nucleation in single crystal magnesium," in *Magnesium Technology*, 2011, pp. 295–299.

[171] J. Wang, M. Ramajayam, E. Charrault, and N. Stanford, "Quantification of precipitate

hardening of twin nucleation and growth in Mg and Mg-5Zn using micro-pillar compression," *Acta Mater.*, vol. 163, pp. 68–77, Jan. 2019.

[172] J. Wang, J. M. Molina-Aldareguía, and J. LLorca, "Effect of Al content on the critical resolved shear stress for twin nucleation and growth in Mg alloys," *Acta Mater.*, vol. 188, pp. 215–227, Apr. 2020.

[173] D. I. Tomsett and M. Bevis, "The incorporation of basal slip dislocations in (1012) twins in zinc crystals," *Philos. Mag.*, vol. 19, no. 157, pp. 129–140, 1969.

[174] H. Fan, S. Aubry, A. Arsenlis, and J. A. El-Awady, "The role of twinning deformation on the hardening response of polycrystalline magnesium from discrete dislocation dynamics simulations," *Acta Mater.*, vol. 92, pp. 126–139, Jun. 2015.

[175] H. Fan, S. Aubry, A. Arsenlis, and J. A. El-Awady, "Grain size effects on dislocation and twinning mediated plasticity in magnesium," *Scr. Mater.*, vol. 112, pp. 50–53, Feb. 2016.

[176] H. Tonda, S. Ando, K. Takashima, and T. Vreeland, "Anomalous temperature dependence of the yield stress by {1122}〈1123〉 secondary pyramidal slip in cadmium crystals-II. Mechanism," *Acta Metall. Mater.*, vol. 42, no. 8, pp. 2853–2858, Aug. 1994.

[177] Y. Tang and J. A. El-Awady, "Formation and slip of pyramidal dislocations in hexagonal close-packed magnesium single crystals," *Acta Mater.*, vol. 71, pp. 319–332, 2014.

[178] J. Zhang, Y. Zhang, J. A. El-Awady, and Y. Tang, "The plausibility of <c + a> dislocation slip on {-12-11} planes in Mg," *Scr. Mater.*, vol. 156, pp. 19–22, 2018.